POLISH ACADEMY OF SCIENCES

THERMODYNAMICS AND COMBUSTION COMMITTEE

archives of thermodynamics

QUARTERLY
Vol. 38
2017
No. 3

WYDAWNICTWO IMP PAN

Wydawnictwo IMP
Gdańsk

Editorial Office

Archives of Thermodynamics
The Szewalski Institute of Fluid Flow Machinery, Fiszera 14, 80-231 Gdańsk, Poland,
Tel.: (+48) 58-341-12-71 int. 141, E-mail: redakcja@imp.gda.pl
http://www.imp.gda.pl/archives-of-thermodynamics/
http://at.czasopisma.pan.pl/

Publication funding of this journal is provided by resources of the Polish Academy of Sciences and the Szewalski Institute of Fluid-Flow Machinery PASci

Terms of subscription outside Poland
Annual subscription rate outside Poland (2017) is 120 EUR. Price of single issue is 30 EUR. Back of previously published volumes are available on request. Subscription orders should be sent directly to **IMP PAN Publishers, The Szewalski Institute of Fluid-Flow Machinery PASci, ul. Fiszera 14, 80-231 Gdansk, Poland**; fax: (+48) 58-341-61-44; e-mail: now@imp.gda.pl. Payments should be transferred to the bank account of IMP PAN: IBAN 28 1130 1121 0006 5498 9520 0011 at Bank Gospodarstwa Krajowego; Code SWIFT: GOSKPLPW

Warunki prenumeraty w Polsce
Roczna prenumerata (2017 r.) wynosi 168 PLN. Cena pojedynczego numeru wynosi 42 PLN. Osiągalne są również wydania archiwalne. Zamówienia z określeniem okresu prenumeraty, nazwiskiem i adresem odbiorcy należy kierować bezpośrednio do Wydawcy (Instytut Maszyn Przepływowych im. R. Szewalskiego PAN, ul. Fiszera 14, 80-231 Gdańsk, Aleksandra Nowaczewska, e-mail: now@imp.gda.pl). Wpłaty prosimy kierować na konto Instytutu Maszyn Przepływowych PAN nr 28 1130 1121 0006 5498 9520 0011 w Banku Gospodarstwa Krajowego

Articles in *Archives of Thermodynamics* are abstracted and indexed within:

Applied Mechanics Reviews • BazTech • Arianta • Baidu Scholar • Cabell's Directory • Celdes • Chemical Abstracts Service (CAS) - CAplus • CNKI Scholar (China National Knowledge Infrastucture) • CNPIEC • DOAJ • EBSCO (relevant databases) • EBSCO Discovery Service • Elsevier - SCOPUS • Genamics JournalSeek • Google Scholar • Inspec • Index Copernicus • J-Gate • Journal TOCs • Naviga (Softweco) • Paperbase • Pirabase • POL-index • Polymer Library • Primo Central (ExLibris) • ProQuest (relevant databases) • ReadCube • Referativnyi Zhurnal (VINITI) • SCImago (SJR) • Summon (Serials Solutions/ProQuest) • TDOne (TDNet) • TEMA Technik und Management • Ulrich's Periodicals Directory/ulrichsweb • WorldCat (OCLC)

Online ISSN 2083-6023
DE GRUYTER – http://www.degruyter.com/view/j/aoter

Typeset in LaTeX
Printed and bound by
Centrum Poligrafii Sp. z o.o., Łopuszańska 53, 02-232 Warszawa

archives
of thermodynamics
Vol. **38**(2017), No. 3, 3–21
DOI: 10.1515/aoter-2017-0013

The performance of H_2O, R134a, SES36, ethanol, and HFE7100 two-phase closed thermosyphons for varying operating parameters and geometry

RAFAŁ ANDRZEJCZYK[*]
TOMASZ MUSZYŃSKI

Gdańsk University of Technology, Narutowicza 11/12, 80-233 Gdańsk, Poland

Abstract In this study, the influences of different parameters at performance two-phase closed thermosiphon (TPCT) was presented. It has been confirmed that the working fluid, as well as operating parameters and fill ratio, are very important factors in the performance of TPCT. The article shows characteristics of gravitational tube geometries, as well as the technical characteristic of the most important system components, i.e., the evaporator/condenser. The experiment's plan and the results of it for the two-phase thermosiphon for both evaluated geometries with varying thermal and fluid flow parameters are presented. Experiments were performed for the most perspective working fluids, namely: water, R134a, SES36, ethanol and HFE7100. Obtained research proves the possibility to use TPCT for heat recovery from the industrial waste water.

Keywords: Two-phase closed thermosiphon; Heat pipe; Energy efficiency; NTU (number of heat transfer units); Heat recovery

Nomenclature

A – surface area, m^2
c_p – specific heat, J/kgK
D – diameter, m

---

[*] Corresponding Author. Email rafanrz@pg.gda.pl

f – friction factor
$\dot{G}$ – mass flux, kg/m^{2}s
LMTD – logarithmic mean temperature difference
L – length, m
$\dot{m}$ – mass flow , kg/s
NTU – number of transfer units
Nu – Nusselt number
p – pressure, Pa
ΔP – pressure drop, Pa
Q – heat, J
$\dot{Q}$ – rate of heat, W
r – radius, m
Re – Reynolds number
T – temperature, °C
ΔT – temperature difference, °C
U – overall heat transfer coefficient, W/m^{2}K
w – velocity, m/s
W – fluid heat capacity rate, W/K
$\dot{V}$ – volumetric flow, m^3/s
V – volume, m^3
X – radial direction

Greek symbols

ε – heat exchanger effectiveness
φ – fill ratio
ρ – density of water, kg/m^3
μ – dynamic viscosity, Pa s

Superscripts

a – adiabatic
abs – absolute
c – cold
con – condensation
e – evaporator
exp – experimental
h – hot
min – minimum
max – maximum
o – outer
out – output
p – poll boiling
s – surface
sh – shell
sat – saturation
w – water

1 Introduction

Thermosiphons are enclosed passive two-phase heat transfer devices. Heat applied to the evaporator section vaporizes the filling liquid which then rises to the condenser section. In the condenser section, vapor condenses and discharges its heat of vaporization. The condensate then flows back to the evaporator section due to gravitational force. The cycle of consecutive evaporation and condensation continues as long as heat is provided at the evaporator and removed at the condenser. The highly efficient thermal transport process of evaporation and condensation maximizes the thermal conductance between the heat source and the heat sink [1]. The amount of heat that can be transported by these devices is normally several orders of magnitude greater than pure conduction through a solid metal [2,3]. They are proven to be very effective, low cost and reliable heat transfer devices for applications in many thermal management and heat recovery systems [4]. They are used in many applications including but not limited to passive ground/road antifreezing [5], baking ovens, heat exchangers in waste heat recovery applications [6], water heaters and solar energy systems and are showing some promise in high-performance electronics thermal management for situations which are orientation specific [7,8]. The heat transfer performance of a two-phase closed thermosiphon (TPCT) is significantly affected by geometry, inclination angle, vapor temperature and pressure, aspect ratio, filling ratio and thermophysical properties of the working fluid. Among those, filling ratio is one of the most important factors [9].

Khazaee [10] investigated TPCT with ethanol as a working fluid. In the experiments, two copper tubes of 1000 mm length and with 15 mm, 25 mm diameters were used. The thermosiphon consisted of three sections, i.e., adiabatic ($L = 160$ mm), evaporating ($L = 430$ mm) and condensing ones ($L = 430$ mm). The heat was supplied by an electric heater. The study showed a good agreement between experimental data and literature correlations for heat transfer coefficient for boiling and condensation into TPCT conditions. The author also proposed own empirical correlation for boiling heat transfer coefficient. Elmosbahi *et al.* [11] investigated the influence of working fluid filling ratio on heat pipe performance, for solar thermal collector applications. Measurements of absorbed heat flux and the temperature in different positions over the heat pipe were done. The heat pipe was made of an 8 mm copper tube (inner diameter was 6 mm). The tube was 715 mm long. The paper proved that the better performance was observed for methanol filling ratio close to 2/3. Fadhl *et al.* [12]

used numerical methods to predict temperature distributions of TPCT. In their work, the volume of the fluid model (VOF) in Ansys Fluent software with user-defined functions was used in calculations. Also, the experimental data from own experimental test section were collected to compare it with numerical simulations. The 0.5 m – a long smooth copper tube with a 22 mm outer diameter was used as a TPCT. The tube wall thickness was 0.9 mm. It consisted of 0.2 m long evaporation section, 0.1 m long adiabatic section, and 0.2 m long condensation section. Into experiments as well as in numerical simulation water was used as a working fluid. The good agreement between experimental data and numerical simulations were obtained. Kannan *et al.* [13] observed the influence of various operational parameters of two-phase closed thermosiphon on its heat transport capability. The three different diameters of thermosiphon tubes were used: 6.7, 9.5 and 12 mm. In all three cases, wall thickness was equal to 0.65 mm. The tubes were 1000 mm long and consisted of 300 mm long evaporation section, 200 mm long adiabatic section, and 500 mm long condensation section. The heat was supplied by means of an electric heater. Condensation section was cooled by water in the simple tube in tube heat exchanger. As working fluids water, ethanol, methanol, and acetone, with filling ratio between 30% to 90% were used. Authors observed marginal influences of filling ratio for heat transfer capabilities. They also observed the best water capabilities to heat transfer for operating temperature between 30 and 70 °C. It has been also emphasized that acetone had the lowest heat transfer capabilities. Jouhara *et al.* [14] carried experimental investigation of small diameter TPCT charged with water and dielectric working fluids: FC-84, FC-77, and FC-3283. The thermosiphon was made out of 200 mm long copper tube with 6 mm inner diameter. The evaporation section was 40 mm long and condensation was 60 mm long. Authors emphasize that the geometrical parameters of TPCT were assumed based on what might be expected in compact heat exchangers. Experiments confirmed the best capabilities to heat transfer for water. Despite the benefits of using dielectric fluid, water outperforms them. Ong *et al.* [15] worked at the power input, filling ratio and angle inclination influence on the thermal performance of two-phase closed thermosiphon. In their study, they used R-410A refrigerant as a working fluid. The tests were performed at a low evaporator temperature. The tested element was fabricated as 930 mm long copper pipe with 12.7 mm outer diameter and 9.5 mm inner diameter. The evaporation, condensation, and adiabatic sections were equally long. As in the previous studies, the heat was supplied by an electric heater. Condensation section was cooled by tube in tube heat exchanger with water as a coolant. Presented study did not confirm the influence of filling ratio and inclination angle on the TPCT performance. MacGregor *et al.* [16] studied the performance of two-phase thermosiphon with low global warming potential fluids. Authors searched replacements for R134a one of the most common working fluids in such applications. Based on authors selection methodology three potential replacement fluids were chosen, namely water, methanol, and 5% ethylene glycol-water mixture. The mixture of water and glycol was chosen to avoid problems associated with freezing. As a test element, 2200 mm long copper tube with 15.9 mm outer diameter was used. The tube had enhanced internal surface in the form of grooves. The domestic hot and cold water was used as a heat source and heat sink. The experiments showed that water-ethylene glycol mixture could be a good replacement of R134a in TPCT. It should be also noted that for certain conditions its performance was lower than filled with R134a.

The main problem of process industry is to supply efficient heat exchangers for given operating conditions [17–20]. This problem is even more noticeable in waste heat recovery systems [21,22]. The difficulty which occurs during the heat recovery from waste water or industrial water is the contamination, and thereby the risk of infiltration of harmful substances into the heat transfer medium. Another concern is the increase of flow and heat transfer resistance in the context of impurities deposition of on the exchanger surface [23]. In the case of using TPCT, these risks of infiltration of harmful substances into the heat transfer medium are low, also it is quite easy to clean heat transfer surface.

There are not many studies during the two-phase flow of new perspectives dielectric fluids such as HFE-7100, SES36 [24,25]. Those fluids are more environmentally friendly compared to R134a or R404a. In this paper, the thermal performance of copper thermosiphons charged with water as well as ethanol, R134a, HFE-7100, and SES36 is reported for two TPCT geometries. HFE-7100, SES36 liquids were chosen for testing since they are dielectric and cover a range of thermophysical properties, in particular, boiling points in the range of 30–100 °C. Most of the studies emphasize geometries parameters of evaporator and condenser as one of the important factors which influence on TPCT performance. In this studies, the efficiency of condenser heat exchanger was also considered.

2 Experimental apparatus

The measuring system was presented as Fig. 1. The rig consists of two closed loops of test fluid. The facility was intended to work with any non-chemically aggressive working fluids. In both of loops, circulation is forced by electrically powered pumps with a magnetic coupling, capable of providing the mass flow rate from 1×10^{-3} to 5×10^{-3} kg/s and the overpressure up to 800 kPa. This type of pump has been chosen to provide the circulation of fluid in the test sections and to avoid flow pulsations. On the other hand, using distilled water to supply both, the condenser and the evaporator, allowed to eliminate an additional heat conduction resistance associated with sedimentation of the so-called limescale. Adjustment of the mass flow rate is realized by two independent inverters. The inlet and outlet temperatures of hot and cold water were recorded using 4 T-type thermocouples inserted at the inlet and outlet collectors. After obtaining constant parameters, temperatures were measured three times with an accuracy of 0.5 °C in the time steps of 20 min, and the average values were used for further analysis. Appropriate arrangements were provided to measure the pressure loss of both pipes in pipe heat exchangers at shell side. Table 1 presented the experimental uncertainty.

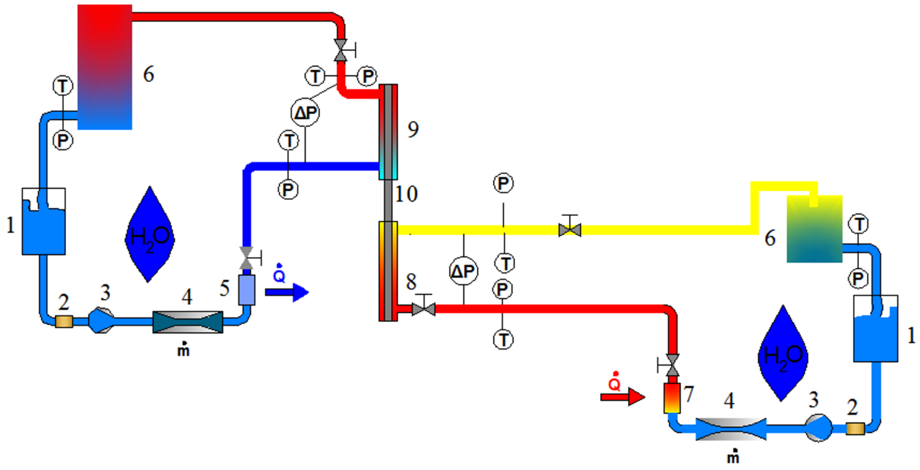

Figure 1: The test rig : 1 – fluid tank, 2 – filter, 3 – pump, 4 – Corioliss flow meter, 5 – chiller, 6 – heat exchanger, 7 – electrical heater, 8 – evaporator, 9 – condenser, 10 – two-phase thermosiphon [26].

Table 1: Partial experimental uncertainties.

Parameter	Unit	Measurement range	Uncertainty
T	°C	10–60	±1.5
$\dot{m}_c$	kg/s	0.01–0.025	±0,005
ΔP	kPa	0–200	±0.5
P_{abs}	kPa	0–3	±0.108

Experimental uncertainty was determined using the sequential perturbation method of error analysis. This method allows determination of the total experimental error by including errors originating from individual sources into a general database and averaging it using the root mean square method. The error analysis was executed automatically for each data series. It was implemented in the spreadsheets used for data reduction.

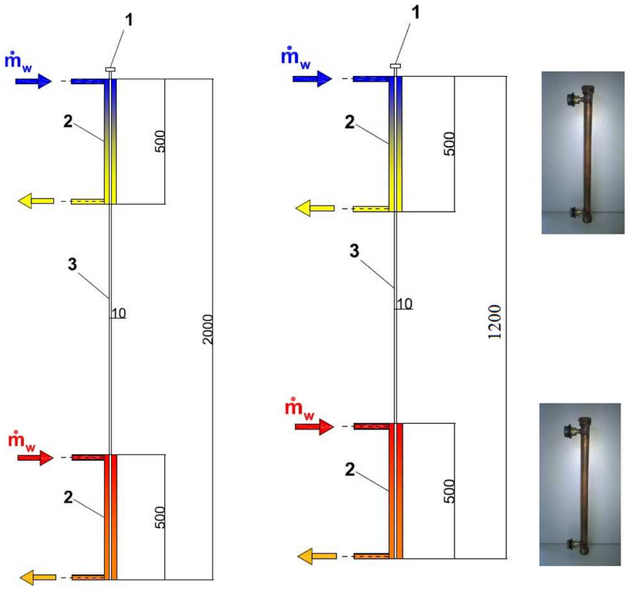

Figure 2: Illustration of two-phase thermosiphons with different length: 1 – Schroder valve, 2 – typical tube in tube heat exchanger (evaporator/condenser) [26].

The experiments were conducted for two thermosiphon geometries (see Fig. 2). Both investigated elements were made of copper pipes with an inner diameter of 10 mm and outer of 12 mm. In both cases, the length of the section of heat delivery and reception (and therefore also the heat transfer surface) was the same. Due to differences in overall length of the tubes, the length of the adiabatic section varied. Before filling, each thermosiphon was first discharged by the vacuum pump Vi-220SV, whereas before changing the medium, in each case the system was subjected to rinsing, drying and purging with nitrogen, and then emptied in vacuum in order to eliminate the influence of moisture and inert gasses.

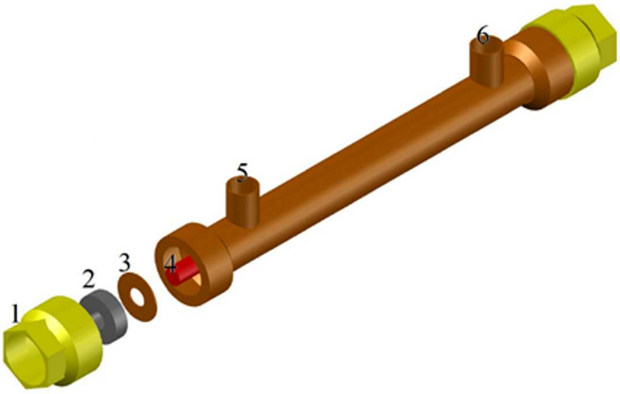

Figure 3: Construction of a typical pipe in pipe heat exchanger working as evaporator/ condenser in test elements: 1 – nut, 2 – gasket, 3 – pad, 4 – heat pipe, 5 – inlet, 6 – outlet [26].

The evaporator and condenser were made as a conventional tube in tube heat exchanger (Fig. 3). The shell of the heat exchanger was also made of copper, and the additional Teflon sealing was applied.

3 Experimental research

3.1 Preliminary heat flow tests for tube in tube heat exchangers

Prior to the appropriate experimental measurements of two-phase thermosiphon, preliminary heat-flow tests of tube in tube heat exchanger were carried out. These devices were used to provide/receive heat in the circuit of the gravitational heat pipe. For this purpose, in the preliminary study, the electric heater was used as a heat source. For the heating element, we have here a case of heat conduction from the internal heat source in the form of a resistance wire powered by electric current.

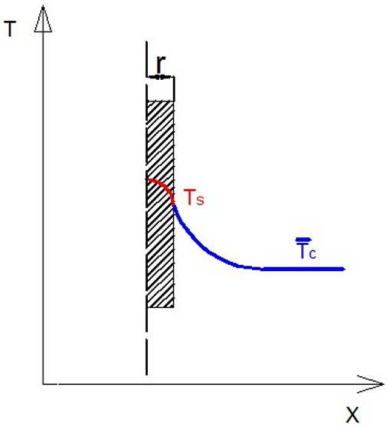

Figure 4: Temperature distribution in double pipe heat exchanger with electrical heat source: $\overline{T}_c$ – mean cold fluid temperature, T_s – wall temperature, r - radius of a heater [26].

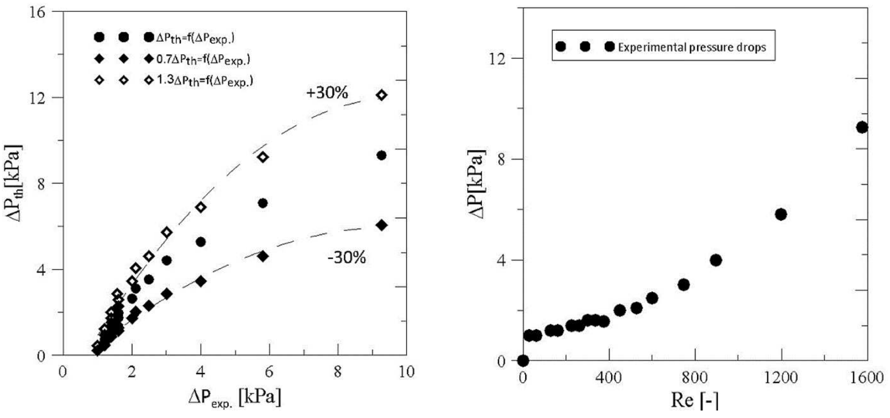

a) b)

Figure 5: Hydraulic characteristic of water flow in double pipe heat exchanger: a) comparison between experimental and theoretical values of pressure drops, b) pressure drop as a function of Reynolds number.

Figure 5 presents the hydraulic resistance of heat exchangers as a function of Reynolds number. Pressure drop measurement is carried out using the piezoelectric smart differential pressure transducer. The measuring range of the pressure transducer is 0–200 kPa, and the measuring accuracy is ±0.5% of the full scale (FS). The pressure at the inlet and outlet of the heat exchanger is also measured using conventional pressure transducers (measurement is thus duplicated, it is important to verify operation of the system and capture any hardware failure). At the inlet, an absolute pressure transducer with a measuring range of 0–400 kPa and a precision of 0.25% FS is mounted. At the outlet gauge pressure transducer with the range 0–600 kPa and accuracy of 0.5% FS is installed. The experimental results were compared to the theoretical calculations (friction factor was assumed so as for the annular flow $f = 96/\mathrm{Re}$).

$$\triangle P_{th} = 4f \frac{\dot{G}^2}{2\rho} \,, \tag{1}$$

$$\dot{G} = \frac{\dot{m}_c}{A_p} \,, \tag{2}$$

$$A_p = \frac{\pi D_e}{4} \,, \tag{3}$$

$$D_e = \frac{(4V_{sh})}{\pi\, D_0\, L} \,, \tag{4}$$

$$\mathrm{Re} = \frac{\dot{G}\, D_e}{\mu} \,. \tag{5}$$

The outcomes are within the limits of the correlation accuracy and the raised spread of small Reynolds numbers is undoubtedly caused by a measurement equipment errors (±0.5 kPa).

The efficiency of the heat exchanger was evaluated by using the well-known ε-NTU method. The formulas below presents a calculation methodology:

$$\mathrm{NTU} = \frac{U\, A}{W_{min}} \,, \tag{6}$$

$$W_{min} = c_p\, \dot{m}_c \,, \tag{7}$$

$$\varepsilon_{exp} = \frac{\dot{Q}}{\dot{Q}_{max}} \,, \tag{8}$$

$$\dot{Q} = W_c \, \left(T_{c,out} - T_{c,in}\right) \,, \tag{9}$$

$$\triangle T_{max} = T_s - T_{c,in} \ , \tag{10}$$

$$\dot{Q}_{max} = W_{min} \, \triangle T_{max} \ . \tag{11}$$

The predicted value of efficiency was calculated from [27]

$$\varepsilon = \frac{1 - \exp\left[\,-\,\mathrm{NTU}\ (1 - W_{min})\,\right]}{1 + W_{min}\ \exp\left[\,-\,\mathrm{NTU}\ (1 - W_{min})\,\right]} \quad \text{for} \quad W_{min} < 1 \ , \tag{12}$$

and

$$\varepsilon = \frac{\mathrm{NTU}}{1 + \mathrm{NTU}} \quad \text{for} \quad W_{min} = 1 \ .$$

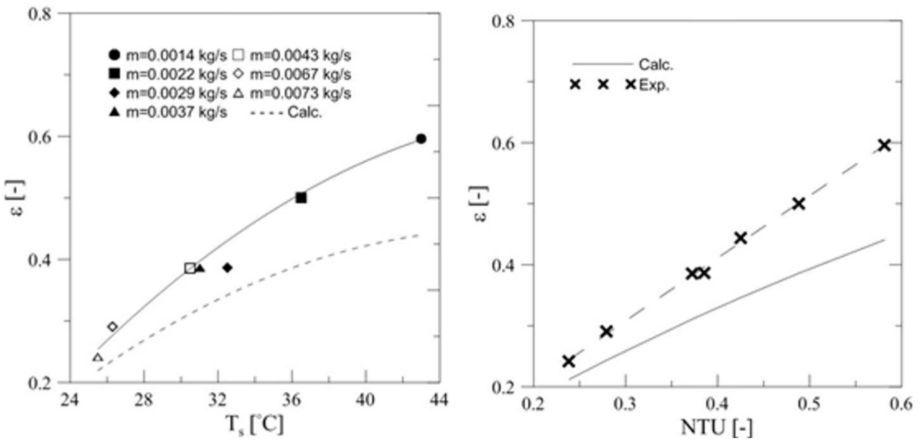

a) b)

Figure 6: Efficiency of pipe in pipe heat exchanger with variable flow parameters, constant cold inlet water temperature and heat flux of 100 W: a) comparison of experimental and calculated efficiency as a function of surface temperature, b) comparison of experimental and calculated efficiency as a function of NTU [26].

As can be seen from Fig. 6 the heat exchanger efficiency is larger than those predicted by theoretical correlation. It should be also noted that efficiency is increasing proportional to the surface temperature and inversely proportionally to mass flow rate of cooling water. The characteristic lines were formed using regression analysis.

Figure 7 presented results for higher heat flux. There is no significant difference in small water flow rate. However, it has to be emphasized that for larger heat flux efficiency are also increasing for larger water flow rate.

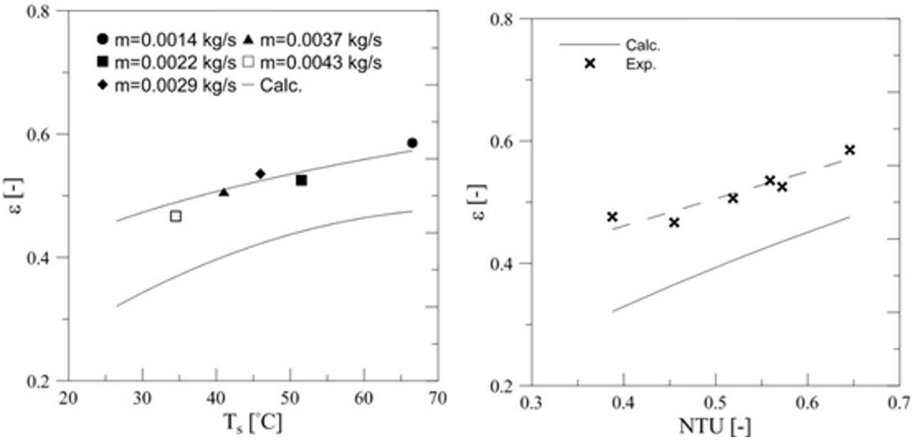

a) b)

Figure 7: Efficiency of pipe in pipe heat exchanger with variable flow parameters, constant cold water inlet temperature and heat flux of 190 W: a) comparison of experimental and calculated efficiency as a function of surface temperature, b) comparison of experimental and calculated efficiency as a function of NTU [26].

In this case as before the experimental results are greater than calculated. The characteristic curve is much flatter also that curves were formed using regression analysis. The results presented for the steady heat flux prove, that the efficiency of exchanger rise with the wall temperature increase, but only slightly depends on the mass flow rate for greater heat flux. In contrast, for the increasing heat flux, as for constant mass flow rate and the inlet temperature of the cooling water, in the tested heat exchanger efficiency is almost constant (see Fig. 8). In authors opinion, it is an effect of almost constant heat transfer coefficient for the same water mass flow rate.

3.2 Influences of working fluids thermophysical parameters

Obtained results enabled to prepare appropriate 'strategy' of experimental studies and proper estimation of set parameters for the target device. The main part this study was is concerned with the selection of appropriate working medium for the application in two-phase thermosiphon, which is an element of the waste heat recovery system. In the study, the following working fluids were used: distilled water, SES36, HFE-07100, R134a, and

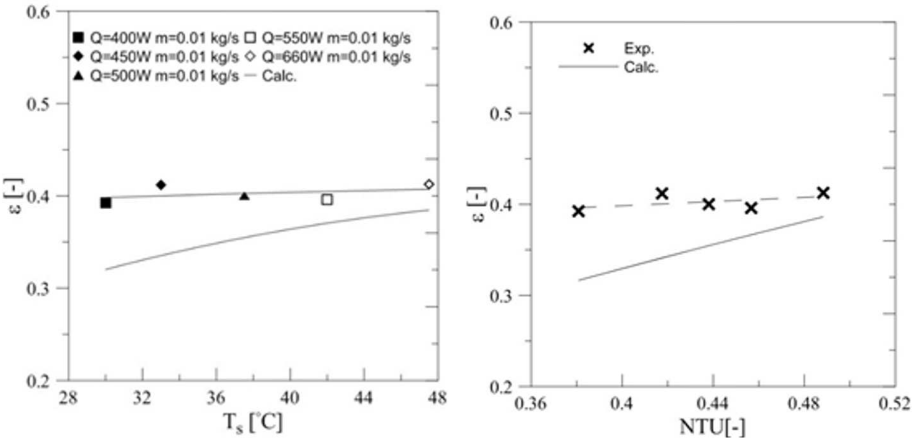

a) b)

Figure 8: Efficiency of pipe in pipe heat exchanger with constant flow parameters, cold inlet temperature, and variable heat flux: a) comparison of experimental and calculated efficiency as a function of surface temperature, b) comparison of experimental and calculated efficiency as a function of NTU [26].

99,8% ethanol. In Fig. 9 the outcomes are presented (all characteristic curves were formed using regression analysis) .

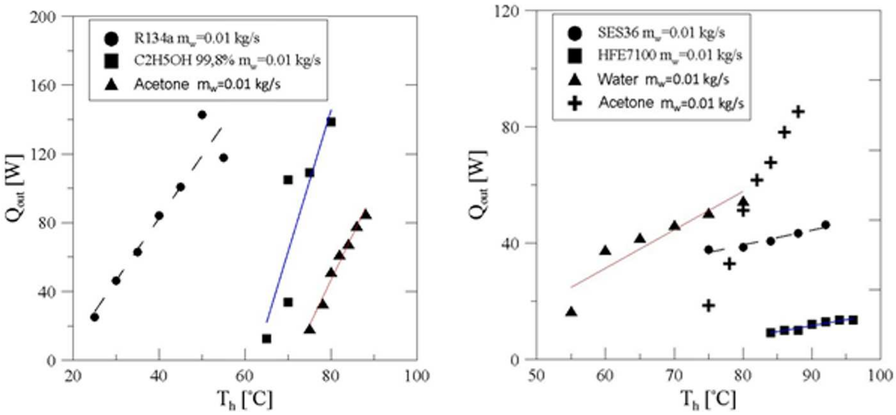

a) b)

Figure 9: Working characteristic of TPCT for filling ratio of 100% – type 'a' for different fluids but constant flow mass of fluid and pressure: a) most efficient fluids, b) low efficiency fluids.

For the first geometry (type 'a') presented results clearly imply that the highest efficiency is for the R134a and ethanol. Wherein the 'activation temperature' for R134a is significantly lower than for ethanol. Therefore, this factor should be intended for systems powered by low-temperature heat. The arrangement with ethanol as the working medium is more suitable for recovery heat of temperature above 75 °C. For the second geometry (type 'b') following liquids were examined: SES36, water, and ethanol 99.8%. Once again it appeared that a system working with water has a good performance (Fig. 10), but much better results have been obtained with ethanol. On this basis, decision was made to provide a more precise examination of that case. Especially in the context of the results obtained for the previous geometry, above case marked by significantly higher efficiency and lower 'activation' temperature.

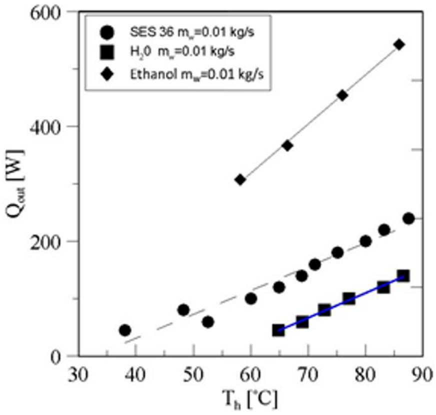

Figure 10: Characteristic of two-phase thermosiphon – type 'b' for fill ratio of: 100% – for different fluids but constant cold water mass flow rate and the same operating pressure.

3.3 Influence of filling ratio

The present experimental investigations were extended by varying the filling level in installation (the mass of working fluid), which is defined as a ratio of the volume occupied by the medium, V_p, to the volume of the evaporator, V_e,

$$\varphi = \frac{V_p}{V_e} \, . \tag{13}$$

The results were divided into two parts: for filling ratio lower than 80% and above 100% (see Fig. 11).

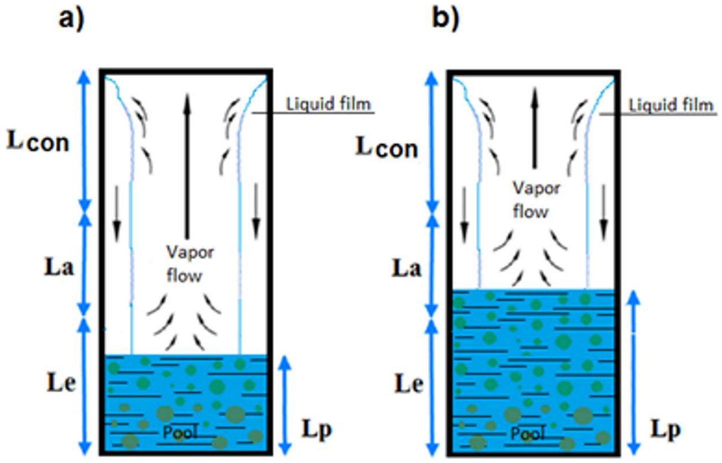

Figure 11: Visualization of flow patterns in TPCT for different fill ratio: a) $\varphi < 80\%$, b) $\varphi > 100\%$ [9].

It can be observed, that for the filling ratio of evaporator below 80%, efficiency reaches its maximum at a rate of heat of approximately 550 W and a flow temperature of the evaporator approx. 80 °C. Another important conclusion is the fact, that the system with the filling of 25% has a considerably better performance at lower temperatures. A smaller amount of fluid in the device leads to its faster evaporation (reduced heat capacity) and thus the soft start of thermosiphon. For the filling ratio of the evaporator above 80% performance of thermosiphon is a linear function of the evaporation temperature. The unit achieves the highest efficiency for the filling in the range of 100–130%. For higher values, an explicit decrease in the performance of the system is noticed.

3.4 Influence of operating parameters at condenser section

Because of the low activation temperature and the largest performance for R134a in the case of type ‘a’ geometry, this fluid was used in the last tests.

The first important proposal is that the saturation temperature of the system rises after reaching the inlet temperature of the hot fluid of approximately 45 °C, then it begins to rapidly decline (see Fig. 13a). The

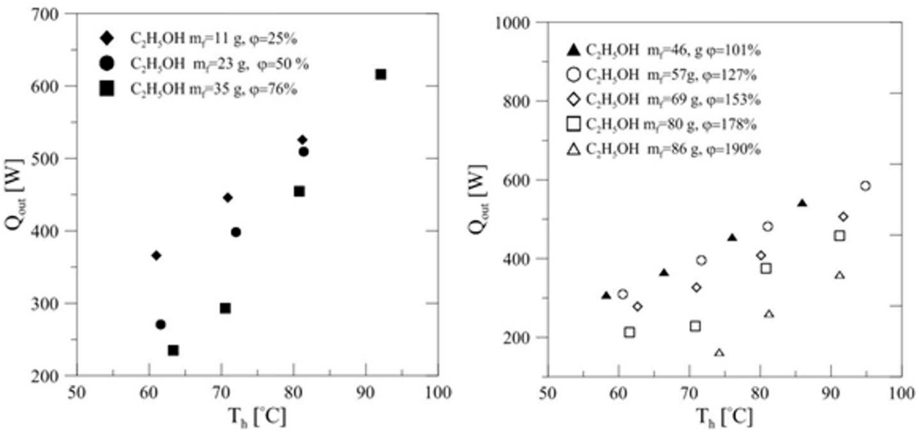

a) b)

Figure 12: Characteristic of two-phase thermosiphon type ‘b’ for different filling ratio and constant pressure: a) operation parameter for filling ratio below 70%, b) operation parameters for filling ratio above 70% [26].

decrease is, however, proportional to the mass flow of cooling water. This is in accordance with the characteristics of the condenser. The quantity of receiving heat does not depend on the mass flow of cooling water, but merely on the temperature of the heat source.

4 Summary

The article is a continuation of a previous material devoted to the issue of efficiency of the two-phase thermosiphon in the context of its application in heat recovery systems [6,26]. The work significantly expands prior matter. The paper reviews the basic knowledge about the influence different parameters at TPCT performance. The design of experiment and research methodology is discussed in detail, especially in an effort to stable operation of the system.

The essential case seems to be here the correct approach to adjustment of the efficiency of the condenser. For this reason, the authors conducted autonomous tests on performance and hydraulic characteristics of the double pipe heat exchanger working as an evaporator/condenser. The analysis allowed for appropriate planning of further research.

Relevant studies based on two types of two-phase thermosiphon geometries of different length of the adiabatic section. In both cases, several types

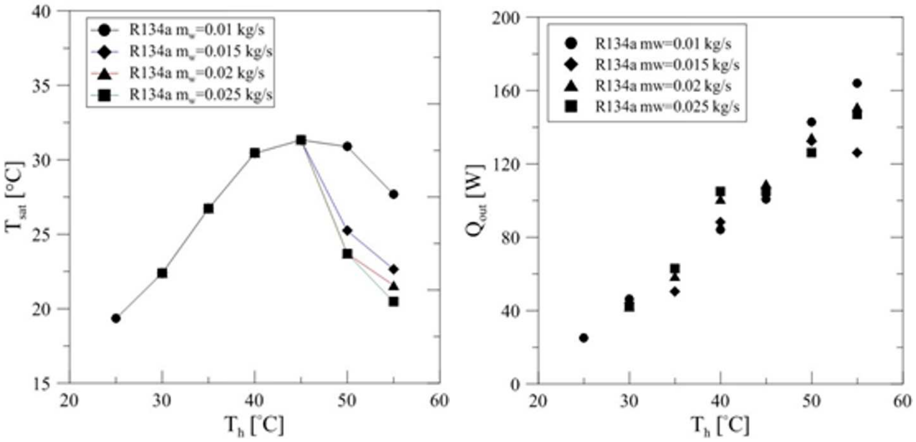

a) b)

Figure 13: Characteristic of two-phase thermosiphon – type ‘a’ for R134a 100% for fill ratio of: a) influences of hot flow stream (condenser efficiency) for saturation temperature, b) influence of heat source temperature on transferred heat [26]

of working fluid were utilized, including those of inorganic origin – water, organic – ethanol, as well as synthetic R134a and SES36, HFE-7100 belonging to a new ‘family’ of energy fluids.

The best results were obtained for a system working with R134a and ethanol, wherein R134a, due to its properties, operated better in lower evaporation temperatures. The authors also discussed the impact of fill ratio, condenser efficiency on the work of the thermosiphon system.

Received 24 February 2017

References

[1] Bieliński H., Mikielewicz J.: *Application of a two-phase thermosyphon loop with minichannels and a minipump in computer cooling.* Arch. Thermodyn. **37**(2016), 1, 3–16, DOI:10.1515/aoter-2016-0001.

[2] Noie S.H.: *Heat transfer characteristics of a two-phase closed thermosyphon.* Appl. Therm. Eng. **25**(2005), 495–506.

[3] Reay D., McGlen R., Kew P.: *Heat pipes: Theory, design and applications.* Butterworth-Heinemann, 2013.

[4] Cieśliński J.T.: *Effect of nanofluid concentration on two-phase thermosyphon heat exchanger performance.* Arch. Thermodyn. **37**(2016), 2, 23–40, DOI:10.1515/aoter-2016-0011.

[5] Andrzejczyk R., Muszyński T., Kozak P.: *Modern method of snow and ice removal from operational surfaces.* Mater. Bud. **12**(2014), 18–20 (in Polish).

[6] Andrzejczyk R., Muszyński T., Kozak P.: *Analysis of the effectiveness of waste heat recovery with application of heat pipe. Part I. Structure and operation of the measurement system, design of heat pipe.* Gaz, Woda i Tech. Sanit. (2015) 171–174 (in Polish).

[7] Muszynski T., Andrzejczyk R.: *Heat transfer characteristics of hybrid microjet – Microchannel cooling module.* Appl. Therm. Eng. **93**(2016), 1360–1366, DOI:10.1016/j.applthermaleng.2015.08.085.

[8] Muszynski T., Andrzejczyk R.: *Applicability of arrays of microjet heat transfer correlations to design compact heat exchangers.* Appl. Therm. Eng. **100**(2016), 105–113, DOI:10.1016/j.applthermaleng.2016.01.120.

[9] Jiao B., Qiu L.M., Zhang X.B., Zhang Y.: *Investigation on the effect of filling ratio on the steady-state heat transfer performance of a vertical two-phase closed thermosyphon.* Appl. Therm. Eng. **28**(2008), 1417–1426.

[10] Khazaee I.: *Experimental investigation and comparison of heat transfer coefficient of a two phase closed thermosyphon.* Int. J. Energy Environ. **5**(2014), 495–505.

[11] Elmosbahi M.S., Dahmouni A.W., Kerkeni C., Guizani A.A., Ben Nasrallah S.: *An experimental investigation on the gravity assisted solar heat pipe under the climatic conditions of Tunisia.* Energy Convers. Manag. **64**(2012), 594–605.

[12] Fadhl B., Wrobel L.C., Jouhara H.: *Numerical modelling of the temperature distribution in a two-phase closed thermosyphon.* Appl. Therm. Eng. **60**(2013), 122–131.

[13] Kannan M., Senthil R., Baskaran R., Deepanraj B.: *An experimental study on heat transport capability of a two phase thermosyphon charged with different working fluids.* Am. J. Appl. Sci. **11**(2014), 584.

[14] Jouhara H., Robinson A.J.: *Experimental investigation of small diameter two-phase closed thermosyphons charged with water FC-84, FC-77 and FC-3283.* Appl. Therm. Eng. **30**(2010), 201–211.

[15] Ong K.S., Goh G., Tshai K.H., Chin W.M.: *Thermal resistance of a thermosyphon filled with R410A operating at low evaporator temperature.* Appl. Therm. Eng. **106**(2016), 1345–1351, DOI:10.1016/j.applthermaleng.2016.06.080.

[16] MacGregor R.W., Kew P.A., Reay D.A.: *Investigation of low Global Warming Potential working fluids for a closed two-phase thermosyphon.* Appl. Therm. Eng. **51**(2013), 917–925.

[17] Andrzejczyk R., Muszynski T.: *Performance analyses of helical coil heat exchangers. The effect of external coil surface modification on heat exchanger effectiveness.* Arch. Thermodyn. **37**(2016), 4, 137–159. DOI:AOT-00010-2016-0032.

[18] Andrzejczyk R., Muszynski T.: *Thermodynamic and geometrical characteristics of mixed convection heat transfer in the shell and coil tube heat exchanger with baffles.* Appl. Therm. Eng. (2017), DOI:10.1016/j.applthermaleng.2017.04.053.

[19] Andrzejczyk R., Muszynski T., Dorao C.A.: *Experimental investigations on adiabatic frictional pressure drops of R134a during flow in 5mm diameter channel.* Exp. Therm. Fluid Sci. **83**(2017), 78–87, DOI:10.1016/j.expthermflusci.2016.12.016.

[20] Muszynski T., Andrzejczyk R., Dorao C.A.: *Investigations on mixture preparation on two phase adiabatic pressure drop of R134a during flow in 5mm diameter channel.* Arch. Thermodyn. **38**(2017), 3, 99-116, DOI:10.1515/aoter-2017-0018.

[21] Muszynski T., Koziel S.M.: *Parametric study of fluid flow and heat transfer over louvered fins of air heat pump evaporator.* Arch. Thermodyn. **37**(2016), 3, 45–62, DOI:10.1515/aoter-2016-0019.

[22] Muszynski T.: *Design and experimental investigations of a cylindrical micro-jet heat exchanger for waste heat recovery systems.* Appl. Therm. Eng. (2017), DOI:10.1016/j.applthermaleng.2017.01.021.

[23] Ma H., Yin L., Shen X., Lu W., Sun Y., Zhang Y., Deng N.: *Experimental study on heat pipe assisted heat exchanger used for industrial waste heat recovery.* Appl. Energy. **169**(2016), 177–186.

[24] Mikielewicz D., Andrzejczyk R., Mikielewicz J.: *Pressure Drop of HFE7000 and HFE7100 in Flow Condensation in Minichannels with Account of Non-Adiabatic Effects.* In: MATEC Web Conf., EDP Sciences, 2014, 1007.

[25] Mikielewicz D., Andrzejczyk R., Jakubowska B., Mikielewicz J.: *Analytical model with nonadiabatic effects for pressure drop and heat transfer during boiling and condensation flows in conventional channels and minichannels.* Heat Transf. Eng. **37**(2016), 1158–1171.

[26] Andrzejczyk R., Muszyński T.: *Analysis of the efectiveness of waste heat recovery. Part 2. Experimental investigations.* Gaz, Woda I Tech. Sanit. (2016) (in Polish).

[27] Teke I., Ağra Ö., Atayilmaz T.Ö., Demir H.: *Determining the best type of heat exchangers for heat recovery.* Appl. Therm. Eng. **30**(2010), 577–583.

archives
of thermodynamics
Vol. **38**(2017), No. 3, 23–48
DOI: 10.1515/aoter-2017-0014

Entropy generation and thermodynamic analysis of solar air heaters with artificial roughness on absorber plate

RADHA K. PRASAD[*]
MUKESH K. SAHU

Department of Mechanical Engineering, National Institute of Technology,
Jamshedpur, Jharkhand, India, Pin - 831014

Abstract This paper presents mathematical modelling and numerical analysis to evaluate entropy generation analysis (EGA) by considering pressure drop and second law efficiency based on thermodynamics for forced convection heat transfer in rectangular duct of a solar air heater with wire as artificial roughness in the form of arc shape geometry on the absorber plate. The investigation includes evaluations of entropy generation, entropy generation number, Bejan number and irreversibilities of roughened as well as smooth absorber plate solar air heaters to compare the relative performances. Furthermore, effects of various roughness parameters and operating parameters on entropy generation have also been investigated. Entropy generation and irreversibilities (exergy destroyed) has its minimum value at relative roughness height of 0.0422 and relative angle of attack of 0.33, which leads to the maximum exergetic efficiency. Entropy generation and exergy based analyses can be adopted for the evaluation of the overall performance of solar air heaters.

Keywords: Entropy generation analysis; Entropy generation number; Irreversibility; Bejan number

Nomenclature

A_C – collector surface area, m^2
Be – Bejan number

---

[*] Corresponding Author. Email rkpappnit@gmail.com

C_p – specific heat of air, J/(kgK)
D – equivalent or hydraulic diameter of duct, m
e – rib roughness height, m
Ex_{dest} – exergy destruction
Ex_{in} – exergy inlet
Ex_{out} – exergy outlet
F' – collector efficiency factor
F_R – collector heat removal factor
G – mass flow rate of air per unit collector area, kg/s m^2
H – height of duct, m
h – heat transfer coefficient, W/m^{2}K
h_w – convective heat transfer coefficient due to wind, W/m^{2}K
h_{c-ab-f} – convective heat transfer coefficient between absorber plate and fluid, W/m^{2}K
I – solar irradiation intensity, W/m^2
K_i – thermal conductivity of insulation, W/(m K)
L – length of duct, m
L_g – cover glass thickness, m
L_1 – gap between covers, m
M – number of glass covers
m – mass flow rate of air, kg/s
Ns – entropy generation number
Nu_s – Nusselt number for smooth duct
Nu – Nusselt number between flowing fluid and absorber plate
Nu_{ab-f} – Nusselt number for roughened duct
Q_s – energy received by the collector absorber plate from the sun
Q_u – useful heat gain, W
P – pitch of roughness element, m
P_m – mechanical power, W
ΔP – pressure drop across the duct, Pa
Pr – Prandtl number
Re – Reynolds number
St – Stanton number
S_{gen} – entropy generation, W/K
T – temperature, K
ΔT – air temperature rise across the duct, K
T_a – atmospheric air temperature, K
T_{bp} – mean bottom plate temperature, K
T_f – mean temperature of fluid, K
T_g – temperature of glass cover, K
T_i – inlet air temperature, K
T_o – outlet air temperature, K
Tp – mean absorber plate temperature, K
T_{sun} – temperature of sun, K
U_L – overall heat loss coefficient, W/m^{2}K
U_t – top loss coefficient, W/m^{2}K
U_b – bottom loss coefficient, W/m^{2}K
U_s – side loss coefficient, W/m^{2}K
V – velocity of air in the duct, m/s
V_w – wind velocity, m/s
W – width of duct, m

Greek symbols

α – angle of attack, degree
β – tilt angle of collector surface, degree
δ_i – insulation thickness , m
ε_p – emissivity of absorber plate
ε_g – emissivity of glass cover
η_{EN} – energy efficiency
η_{eff} – effective efficiency
η_{EX} – exergy efficiency
η_{II} – second law efficiency
μ – dynamic viscosity of air, N s/m^2
μ_{th} – thermal efficiency
$(\tau\alpha)_e$ – effective transmittance-absorptance product
ρ_a – density of air, kg/m^3
σ – Stefan Boltzman's constant , Wm^{-2} K^{-4}

Dimensionless

$\alpha/90$ – relative angle of attack
e/D – relative roughness height
f_r – friction factor for roughened duct
f_s – friction factor for smooth surface
P/e – relative roughness pitch
SAH – solar air heater
W/H – duct aspect ratio

1 Introduction

The increasing use of energy day-by-day and faster depletion of available conventional and non-recycle fossil fuels has compelled to opt for alternative source of energy and hence there is a need of harnessing energy from various non-conventional energy resources like solar, wind, geothermal, tidal etc. Among all the available non-conventional energy resources, the solar energy is the most promising source because of its free availability, non-polluting and non-depleting nature. However, the major disadvantage of this energy is its irregular availability round the year and spasmodic nature day-wise [1]. Solar air heater has wide applications for heating air at low to moderate temperatures. Due to simple, compact and low cost structure, it is employed for space heating, drying of fruits, seeds and grains, timber seasoning, etc. The main draw back with solar air heater is that heat transfer rate from absorber plate to fluid (air) is poor as the specific heat of air is low thus, heat loss to the surroundings is high [1,2].

Several methods to improve the heat transfer rate from the absorber plate of a solar air heater have been reported [2,3]. To provide artificial roughness on absorber plate at its air flow side is one of such methods. Several roughness elements with different geometries have been employed by the investigators in order to enhance the heat transfer rate and thereby to have improved overall thermal performance of such solar air heaters (SAH). The evaluation of thermal efficiency is an incomplete measure of performance because it does not take into account all the factors required for evaluation of overall performance of a solar collector [4,5]. Thermal efficiency only accounts for quantity of energy transferred, and can be ambiguous where heat is recovered at low temperatures. Exergy is maximum work, which can be obtained from a system in a quantified manner [6,7]. The study of entropy generation in heat transfer by forced convection in four different flow configurations: pipe flow, flow over a flat plate, single cylinder in cross-flow, and flow in the entrance region of a flat rectangular duct has been made by Bejan [8]. The entropy generation due to heat transfer and due to viscous effect has been investigated in detail by the author.

Entropy generation in different duct geometries: circular, square, equilaterally triangular and rectangular with the aspect ratio of 1/2, and sinusoidal with the aspect ratio of $\sqrt{3}\big/2$ was studied by Sahin [9]. He determined the optimum duct geometry which minimizes losses for laminar flow at constant heat flux. Sahin [10] studied numerically the effect of variable viscosity on the entropy generation and pumping power in a laminar fluid flow in a duct subjected to constant heat flux and found an optimum duct length which minimizes total energy losses due to both entropy generation and pumping power. Oztop *et al.* [11] studied entropy generation through hexagonal cross-sectional duct for constant wall temperature in laminar flow. Geometrical effect of hexagonal duct was considered. The variation of total entropy generation along the duct length was studied. Dagtekin *et al.* [12] studied the entropy generation analysis in a circular duct with internal longitudinal fins of different shapes for laminar flow. Three different fin shapes, namely thin, triangular and V-shaped ones were chosen for the analysis. Calculations were performed for various lengths and number of fins, temperature difference and fin angle for triangular and V-shaped fins. Ko and Ting [13] analyzed entropy generation induced by forced convection in a curved rectangular duct with external heating by numerical methods for 3D, steady, and laminar flow conditions. The effects of Dean number, external wall heat flux and cross-sectional aspect ratio, on entropy generated from frictional irreversibility and heat transfer irreversibility were investigated. They reported that the optimal aspect ratio is dependent on heat flux and Dean number.

Numerical investigation on entropy generation in concentric curved annular square ducts under constant wall temperature condition was carried out by Haydar Kucuk [14]. The problem was solved by assuming steady, incompressible and fully developed laminar flow with constant properties of the fluid. It was reported that, the distribution of volumetric entropy generation coming out from the heat transfer irreversibility, is depending on the curvature of the duct. Shahi *et al.* [15] studied, entropy generation due to natural convection of a nanofluid consisting of water and Cu in a cavity with a protruded heat source. It was observed that the maximum value of Nusselt number and minimum entropy generation are obtained when heat source mountains in the bottom horizontal wall. Mahian *et al.* [16] numerically studied the entropy generation and heat transfer rate due to nanofluid flow in a flat plate solar collector. Al_2O_3/water nanofluid with four different particle sizes 25–100 nm and volume concentrations up to 4% have been taken. Effects of tube roughness, nanoparticle size, and different thermophysical models have been investigated on the Nu, h, T_o, entropy generation, and Bejan number. A critical mass flow rate was determined under two different values of solar irradiation and ambient temperature.

Velmurugana and Kalaivanana [17] carried out energy and exergy analyses of multipass flat plate solar air heater. They found higher energy and exergy performances of triple pass solar air heater over the single and double pass solar air heaters. Layek *et al.* [18] carried out their numerical investigation based on the second law of thermodynamics. They evaluated entropy generation number and irreversibility distribution ratio of chamfered rib-groove absorber plate solar air heater. Performance evaluation and entropy generation in the double pass solar air heater with longitudinal fins was investigated by Naphon [19]. Behura *et al.* [20] carried out an outdoor experimental investigation by using 3 sided transverse wire rib roughness with only the bottom side insulated remaining sides made with glass. The overall thermal performance was found to be enhanced as compared to one sided transverse ribs. Kumar *et al.* [21] carried out their experimental investigation by employing multiple V-shape wire ribs with gap on the absorber plate and found better performance as compared to the continuous V-shape ribs. Rybiński and Mikielewicz [28] presented two analytical solutions for friction factor and Nusselt number of fully developed laminar fluid flow in straight mini channels having rectangular cross-section. Zima and

Dziewa [29] developed one-dimensional mathematical model for simulation of transient processes in liquid flat plate solar collector tubes.

The literature reveals that although extensive researches have been performed on the use of artificial roughness on absorber plate but the entropy generation analysis based on the second law of thermodynamics for a solar air heater having its absorber plate roughened with arc shaped wire ribs, has not been worked out in detail. In view of this, a mathematical model has been developed to evaluate entropy generation, entropy generation number, Bejan number and irreversibility of a solar air heater having arc shaped wire ribs as roughness element on underside of the absorber plate of the air heater duct. A comparison has been made with a simple solar air heater working under similar conditions in order to have most appropriate and meaningful values of the design parameters for enhanced overall performance.

2 Mathematical modeling

Figure 1 shows schematic diagram of a solar air heater having arc shaped wire ribs as roughness element at the underside of the absorber plate. The geometry of the roughness on absorber plate has been shown in Fig. 2.

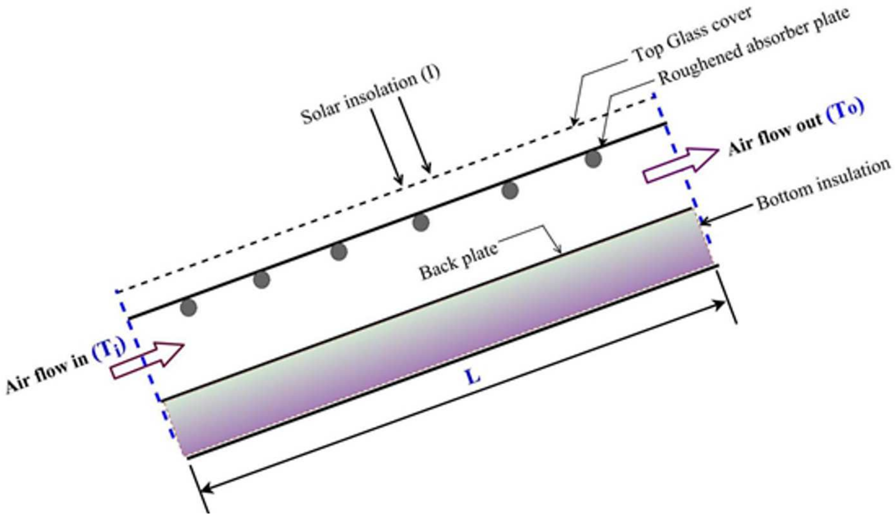

Figure 1: Solar air heater with roughened absorber plate.

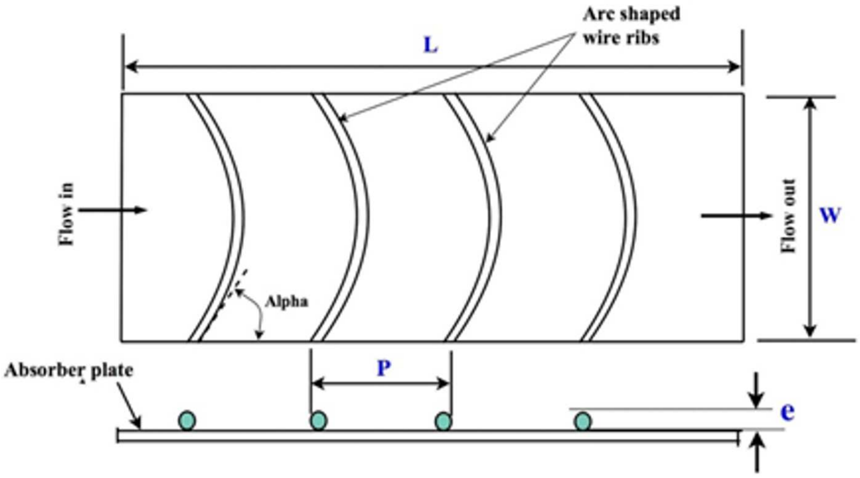

Figure 2: Roughness geometry on absorber plate.

2.1 Evaluation of thermal efficiency

The thermal efficiency of a solar collector is concerned with quantity of useful thermal energy gain and is evaluated, based on the first law of thermodynamics, as [1,2]

$$\eta_{th} = \frac{Qu}{IA_c} = F_R\left[(\tau\alpha)_e - U_L\left(\frac{T_i - T_a}{I}\right)\right] , \tag{1}$$

where F_R is the heat removal factor and it is expressed as

$$F_R = \frac{mC_p}{U_L A_c}\left[1 - \exp\left(\frac{-A_c F' U_L}{mC_p}\right)\right] . \tag{2}$$

The thermal efficiency of a collector using air as the working fluid, can also be given in terms of mass flow rate, specific heat of air and temperature difference of air at outlet and inlet as [1,2]

$$\eta_{th} = \frac{Qu}{IA_c} = \frac{mC_p(T_o - T_i)}{IA_c} . \tag{3}$$

The overall heat loss coefficient (U_L) used in Eq. (1) is calculated by [5,27]

$$U_L = U_b + U_s + U_t . \tag{4}$$

To evaluate the top loss coefficient, U_t, an approximate initial mean plate temperature is assumed and proceeded to find approximate values of U_L, F_R and Q_u [5].

New mean plate temperature is to be calculated as

$$T_P = T_a + \left[\frac{Q_u(1 - F_R)}{A_c U_L F_R}\right] . \tag{5}$$

Outlet temperature of air, T_o, can be calculated as

$$T_o = T_i + \frac{Q_u}{m\, C_p} . \tag{6}$$

The collector efficiency factor F' which is the ratio of actual heat collection rate to the useful heat collection rate when the collector plate is at the local fluid temperature, can be calculated as

$$F' = \frac{h}{h + U_L} , \tag{7}$$

where h is the effective heat transfer coefficient.

2.2 Performance analysis of solar collector based on second law of thermodynamics

Exergy efficiency evaluation, based primarily on the second law of thermodynamics, is a better approach than that of energy efficiency evaluation Eq. (1) for performance analysis of a solar collector as the former takes both into account the quality and quantity of the energy transferred.

Under steady flow condition and treating air as an ideal gas having constant specific heat with negligible humidity, exergy balance equation can be expressed as:

$$\sum Ex_{in} - \sum Ex_{out} = Ex_{dest} . \tag{8}$$

The inlet exergy, Ex_{in}, of absorbed heat from solar radiation is given by

$$Ex_{in} = \left(1 - \frac{T_a}{T_{sun}}\right) Q_s , \tag{9}$$

where Q_s is the energy received by the collector absorber plate from the sun and is given by

$$Q_s = I A_c (\tau\alpha)_e . \tag{10}$$

The outlet exergy, Ex_{out}, includes exergy of outlet fluid

$$Ex_{out} = mC_p(T_o - T_i) + mC_p T_a \ln\left(\frac{T_o}{T_i}\right) + mRT_a \ln\left(\frac{P_{out}}{P_{in}}\right) . \tag{11}$$

In the right side of Eq. (11) the first term represents the variation in enthalpy of air flowing through the collector duct while the mid-term represents the entropy created due to change in temperature of air $(S_{gen})_H$ and the last term represents the entropy created due to pressure drop $(S_{gen})_P$ in the duct.

By combining Eqs. (9), (10) and (11) and substituting into Eq. (8), the resulting relation is obtained as

$$Ex_{dest} = \left(1 - \frac{T_a}{T_{sun}}\right) I A_c (\tau\alpha)_e - \\ mC_p\,(T_o - T_i) - mC_p\,T_a \ln\left(\frac{T_o}{T_i}\right) - m\,RT_a \ln\left(\frac{P_{out}}{P_{in}}\right) . \tag{12}$$

The irreversibility, I_{rev}, expressed in the following form [17,18]

$$I_{rev} = T_a\,S_{gen} . \tag{13}$$

Entropy generation number, Ns, is given by

$$Ns = \frac{I_{rev}}{Q_s} , \tag{14}$$

and Bejan generation number, Be, is given by [22]

$$\mathrm{Be} = \frac{(Ns)_H}{(Ns)_H + (Ns)_P} , \tag{15}$$

where $(Ns)_H$ is entropy generation number due to heat transfer and $(Ns)_P$ is entropy generation number due to pressure drop (friction) in the duct.

The second law efficiency (exergetic efficiency) of solar air heater is given as [17]

$$\eta_{II} = \frac{Ex_{out}}{Ex_{in}} . \tag{16}$$

2.3 Entropy generation analysis of solar collector

There are two sources of entropy generation in a solar collector for heating air [6–8,22–25]. The first entropy generation is due to loss of energy owing to the friction between the collector surface and the air flowing through it, and the second one is due to the heat transfer or temperature change in the heat carrier fluid (air).

Entropy generation, S_{gen}, by considering pressure drop in the collector duct, is given by

$$S_{gen} = \frac{1}{T_a} I_{rev} \,. \tag{17}$$

Dittus –Boelter equation has been used to calculate convective heat transfer coefficient between flowing fluid and conventional smooth plate solar air heater

$$h_{c-ab-f} = \mathrm{Nu}_{ab-f} \frac{K}{D} \,, \tag{18}$$

where Nu_{ab-f} is the Nusselt number for smooth plate solar air heater duct for Re $\geq$ 2300 given by [5]

$$\mathrm{Nu}_{ab-f} = 0.024(\mathrm{Re})^{0.8}(\mathrm{Pr})^{0.4} \,. \tag{19}$$

In the case of laminar flow (Re $<$ 2300) the following correlation for the case of smooth plate solar air heater duct is used [17]:

$$\mathrm{Nu}_{ab-f} = 4.9 + \frac{0.0606\left(\mathrm{RePr}\frac{D}{L}\right)^{0.5}}{1 + 0.0909\left(\mathrm{RePr}\frac{D}{L}\right)^{0.7}(\mathrm{Pr})^{0.17}} \,. \tag{20}$$

For a solar air heater duct having wires as roughness elements in arc shape on the absorber plate, the convective heat transfer coefficient between flowing fluid and absorber plate is calculated by using the correlation [26]

$$\mathrm{Nu}_{ab-f} = 0.001047(\mathrm{Re})^{1.3186}\left(\frac{e}{D}\right)^{0.3772}\left(\frac{\alpha}{90}\right)^{-0.1198} \,. \tag{21}$$

The equivalent or hydraulic diameter D of the duct is given by

$$D = \frac{2(W \times H)}{(W + H)} \,. \tag{22}$$

The Reynolds number of the flow in the duct is given by

$$\mathrm{Re} = \frac{GD}{\mu} \,, \tag{23}$$

where the mass velocity, G, is given by

$$G = \frac{m}{WH} \,. \tag{24}$$

2.4 Pressure drop and mechanical power

In the present analysis the correlation, proposed by Saini and Saini [26] to calculate the friction factor for roughened air heater duct has been used:

$$f_r = 0.14408\mathrm{Re}^{-0.17103}\left(\frac{e}{D}\right)^{0.1765}\left(\frac{\alpha}{90}\right)^{0.1185} \tag{25}$$

and friction factor for smooth plate solar air heater duct is evaluated using the correlation given by

$$f_s = 0.085\mathrm{Re}^{-0.25}\ . \tag{26}$$

The loss of pressure, ΔP, in the air heater duct is calculated as

$$\Delta P = \frac{2\,f\,L\,V^2\,\rho_a}{D}\ . \tag{27}$$

The mechanical power, P_m, needed to overcome the energy loss associated with the pressure drop can be calculated as

$$P_m = \frac{m\Delta P}{\rho_a}\ . \tag{28}$$

2.5 Solutions of performance of solar air heater

The thermal efficiency and entropy generation of roughened solar air heater duct and also that of conventional type for various mass flow rates and solar irradiations have numerically been calculated using collector configuration (Fig.1) and system properties and operating conditions according to Tab. 1. In the present work, the ambient temperatures, T_a, and inlet air temperature, T_i, have been considered as same. In order to determine the top loss coefficients, U_t, an assumed value of mean plate temperature, T_p, is made by using Eq. (5) with approximate values of the heat removal factor, plate efficiency factor and useful heat energy gain are evaluated.

If the new calculated temperature, T_p, of the plate differs by more than 0.0001 from its initial value, then this new temperature is used as the initial temperatures in Eq. (5) for the next iteration and the process is kept continued till an optimum new temperature is obtained with maximum ±0.01% deviation of its respective input values and accordingly the relevant parameters are calculated. In order to obtain the thermal efficiency Eq. (3), second law efficiency Eq. (16), and entropy generation Eq. (17) numerically, programming codes have been developed in MATLAB software environment. The flow chart of the executed program to obtain various parameters is also shown in Fig. 3a.

Table 1: Typical values of system and operating parameters used in presented investigation.

Parameters	Range/base value(s)
Collector dimensions	
Collector length (L), m	1.5
Collector width (W), m	1.0
Duct depth (H), m	0.030
Gap between absorber plate and glass cover (L_1), m	0.05
Absorber plate	
Emissivity of absorber plate (ε_P), dimensionless	0.9
Glass cover	
Number of glass covers (M), dimensionless	1.0
Emissivity of glass cover (ε_g), dimensionless	0.88
Thickness of glass cover (L_g), m	0.004
Effective transmittance absorptance product $\tau\alpha_e$, dimensionless	0.85
Insulation	
Thermal conductivity of insulation (K_i), W/m K	0.037
Thermal conductivity of glass (K_g), W/m K	0.75
Thickness of insulation (δ_i), m	0.05
Relative roughness height (e/D), dimensionless	0.0256–0.0422
Relative roughness pitch (P/e), dimensionless	10
Relative angle of attack ($\alpha/90$), dimensionless	0.33–0.66
Operating parameters	
Atmospheric air temperature (T_a), K	300
Velocity of wind (V_w), m/s	1.5
Reynolds number (Re)	1650–21500
Solar irradiation (I), W/m^2	600–1000

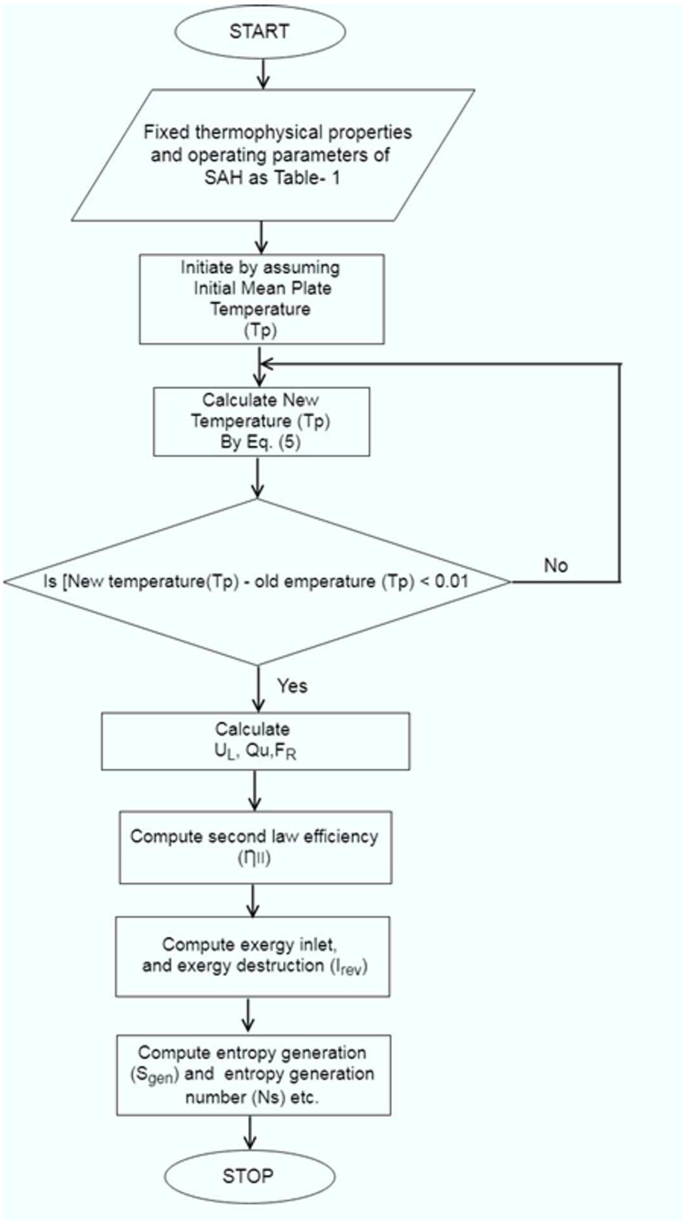

Figure 3: (a) Flow chart for theoretical solution procedure.

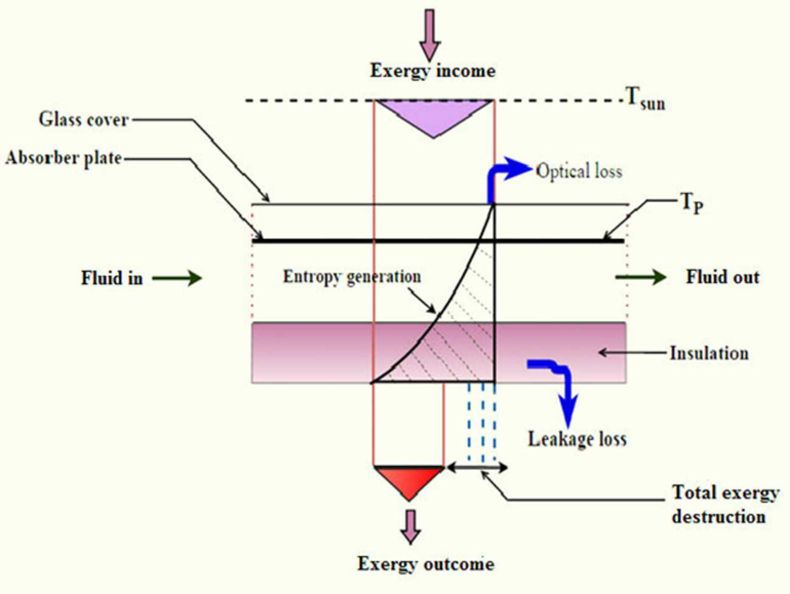

Figure 3: (b) Exergy inflow, entropy generation process and various losses in a solar air heater.

3 Results and discussion

Entropy generation, S_{gen}, entropy generation number, Ns, irreversibility, I_{rev}, or exergy destruction and Bejan number, Be, were calculated and plotted as a function of Reynolds number, Re, covering the entire range of operating and system parameters, given in Tab. 1 Exergy efficiencies account for the temperatures associated with energy transfers to and from solar air heater, and consequently provide a measure of how solar collector nearly approaches to ideal efficiency.

3.1 Effect of relative roughness height and relative angle of attack on entropy generation

Figure 4 shows the plots of entropy generation, S_{gen}, as a function of Reynolds number Re with various values of e/D for roughened solar air heater and also of conventional type. The fixed parameters were taken as $P/e = 10$, $\alpha/90 = 0.33$, and $I = 850$ W/m^2. The entropy generation has been calculated by considering the pressure drop by using Eqs. (12) and (17). It is found from Fig. 4 that, the S_{gen} continues to increase with the increase in Reynolds number for both, i.e., rough and smooth flat plate solar air heaters. Entropy generation values is the highest for the smallest value of $e/D = 0.0256$ and the lowest at highest value of $e/D = 0.0422$ (used for present analysis). The value of entropy generation for smooth plate solar air heating (SAH) duct is lower than the roughened type, for all values of Re. The trend of variation of entropy generation for both types of heaters are similar. The values of S_{gen} at Re = 22956 is 3.3 W/K and 2.68 respectively for roughened ($e/D = 0.0256$, $P/e = 10$, $\alpha/90 = 0.33$) and smooth plate SAHs, hence it can be said that, S_{gen} for roughened duct is 22.85% more as compared to smooth plate SAH. From the above results it can also be concluded that, the S$_{gen}$ decreases with increase in e/D.

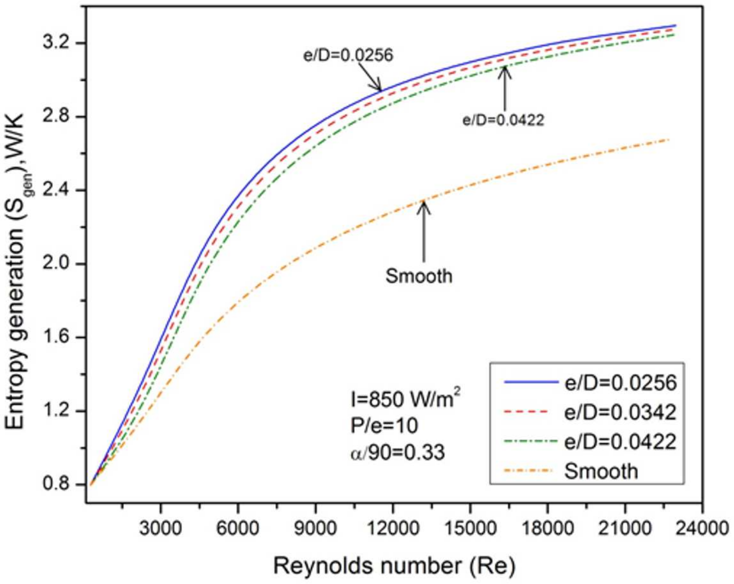

Figure 4: Variation of entropy generation with Reynolds number at different relative roughness height.

Figure 5 exhibits the variation of S_{gen} as a function of Re and different values of relative angle of attack ($\alpha/90$) for arc shape wire rib roughened and also flat plate solar air heater for $T_i = 300$ K. The fixed parameters was taken as $P/e = 10$, $e/D = 0.0422$ and $I = 850$ W/m^2. From Fig. 5 it can be observed that, S_{gen} is found to be increasing with Re for roughened and flat plate solar air heaters. Furthermore it can be seen that S_{gen} values of roughened solar air heater with $\alpha/90 = 0.66$ is higher as compared to the values obtained at $\alpha/90 = 0.33$ and conventional solar air heater for all values of Re. On the basis of above results it can be concluded that the entropy generation can be minimized by using/employing $\alpha/90 = 0.33$ for the present roughened solar air heater which leads into maximization of second law exergetic efficiency.

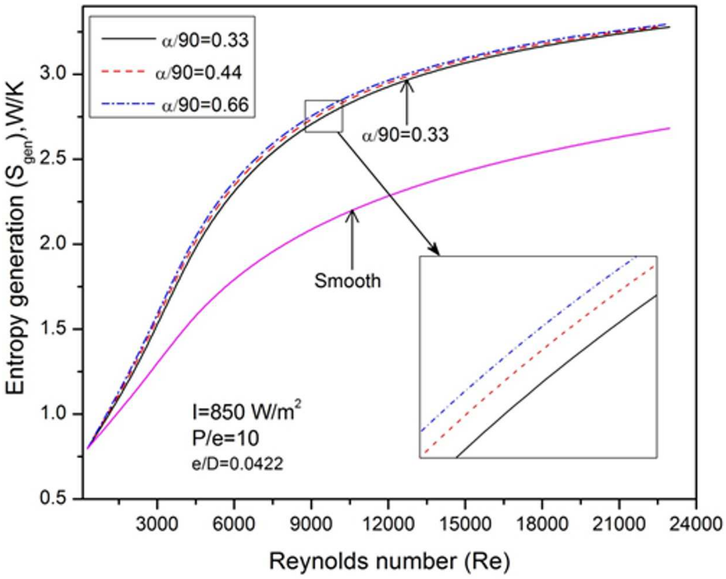

Figure 5: Variation of entropy generation with Reynolds number at different relative angle of attack.

3.2 Effect of roughness parameters on entropy generation number

Figures 6 and 7 shows the effect of three different e/D and $\alpha/90$ values on dimensionless entropy generation number of roughened and simple solar air heaters as a function of Re. The fixed parameters were taken as shown in Fig. 6. It can be observed from Fig. 6 that Ns is found to be increases as values of Re increased, this tendency is followed by both SAHs. The values of Ns is decreases as the value of e/D increases, i.e., the values of Ns for $e/D = 0.0422$ is having lower as compared to $e/D = 0.0256$. However the values of Ns for smooth SAH is lower as compared to roughened duct for all values of Re.

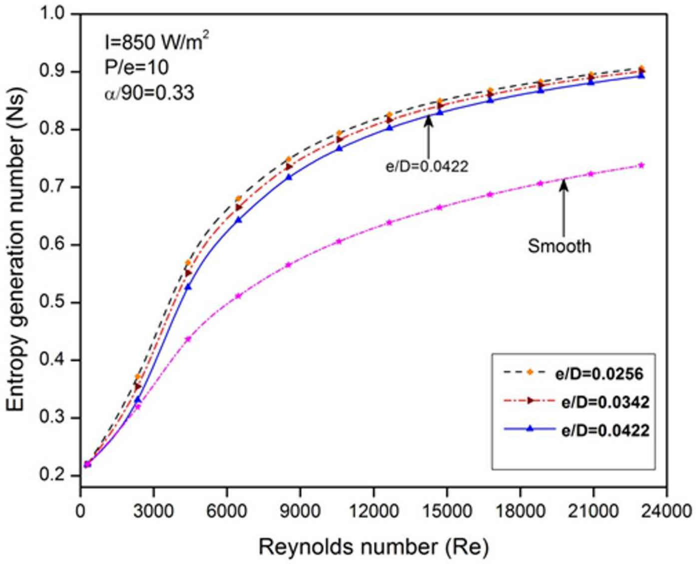

Figure 6: Variation of entropy generation number, Ns, with Re at different e/D.

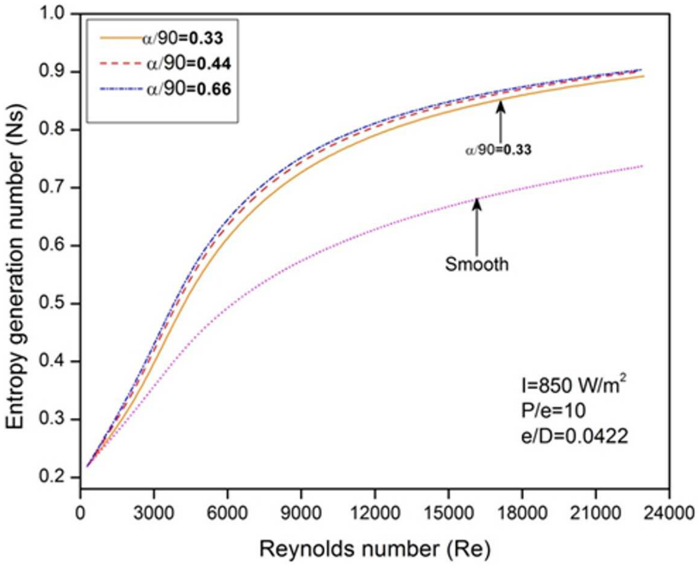

Figure 7: Variation of entropy generation number, Ns, with Re at different $\alpha/90$.

Figure 7 depicts that similar increasing trend is followed by Ns as a function of Re for all three values of $\alpha/90$ for rough and smooth SAHs. The values of Ns is smaller for $\alpha/90 = 0.33$ as compared to $\alpha/90 = 0.44$ and $\alpha/90 = 0.66$. On the other hand smooth SAH is having lower values of Ns as compared to all values of $\alpha/90$ and Re.

3.3 Effect of roughness parameters on irreversibility

Figures 8 and 9 have been drawn in order to show the influence of e/D and $\alpha/90$ values on irreversibility, I_{rev}, of roughened and simple solar air heaters as variation in the values of Re. The fixed parameters such as $P/e = 10$, and $I = 850$ W/m^2 remains unchanged.

As expected, I_{rev}, is having tendency to increase with growth in the values of Re for both SAHs. It happens due to the fact that I_{rev} is product of ambient temperature, T_a, and entropy generation, S_{gen}, (refer Eq. (13)) where S_{gen} is the function of heat transfer and pressure drop (friction) in the duct, as the Re increases these two parameters a increase.

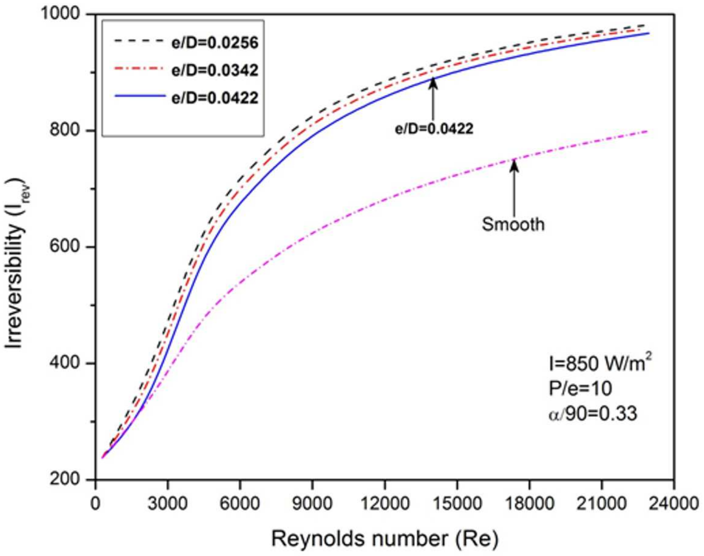

Figure 8: Irreversibility as a function of Reynolds number for different values of e/D.

It is clear from Fig. 9 that, I_{rev} (exergy destruction) increases continuously with increasing Re. The value of irreversibility at $\alpha/90 = 0.66$ is higher as compared to at $\alpha/90 = 0.33$ and 0.44 for all Re. The variation of I_{rev}

and second law efficiency with Re for arc shaped wire roughened solar air heater has been given in Tab. 2. The I_{rev} increases with Re whereas second law efficiency increases upto certain Re.

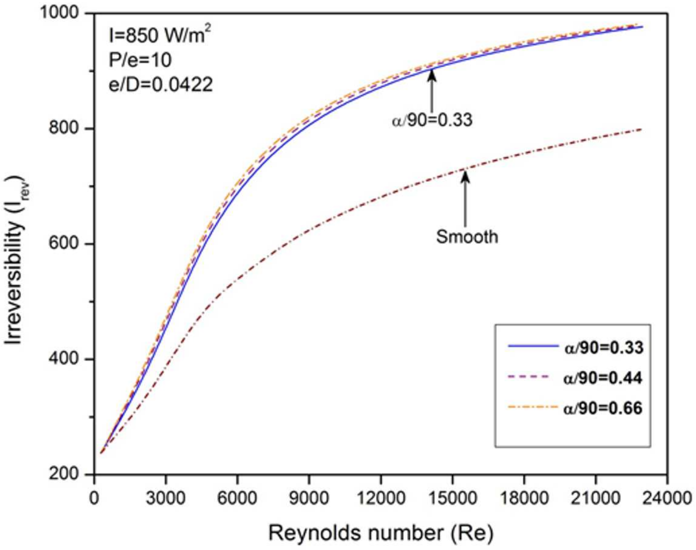

Figure 9: Irreversibility as a function of Reynolds number for different values of $\alpha/90$.

4 Entropy generation and second law efficiency comparison

Figure 10a shows the comparison of S_{gen} and second law efficiency, η_{II}, for roughened SAH with variation in the values of Re. It can be seen from Fig. 10 that second law efficiency increases with Re upto its optimal value (η_{II} = 2.52%, Re = 6460). After passing this critical value of Reynolds number it is exhibiting the decreasing trend. The η_{II} decreases after critical Re. This occurs due to the reason that with increasing Re various losses (like optical loss, leakage loss, friction etc.), as shown in Fig. 3b go on increasing and attribute to the increase in S_{gen} and lowering of second law efficiency. It is imperative to select the various parameters like the duct depth, H, and solar irradiation, I, etc., for reduced S_{gen} and to get optimum useful energy, Q_u, or quality energy efficiency, i.e., η_{II}.

Table 2: Results of irreversibility and second law efficiency of solar air heater with arc shaped wire roughness at $I = 850$ W/m^2 and Re = 270–23.000.

Parameter		Reynolds number	Irreversibility	Exergy loss (%)	Second law efficiency (%)
e/D	$\alpha/90$				
0.0422	0.33	274	237.47	98.98	1.01
		2336	358.73	98.06	1.93
		4398	570.16	97.50	2.49
		6460	696.24	97.48	2.51
		8522	776.26	97.61	2.38
		10584	830.46	97.80	2.19
		12646	869.23	98.01	1.98
		14708	898.26	98.23	1.76
		16770	920.87	98.48	1.51
		18832	939.11	98.76	1.23
		20894	954.28	99.07	0.92
		22956	967.30	99.41	0.58

Furthermore another result can be obtained from Fig. 10a that S_{gen} is having increasing trend with growth in the values of Re (as already discussed in previous section). The variation in S_{gen} and η_{II} with Re has been plotted in Fig. 10b for roughened and smooth plate solar air heaters for the fixed values of the parameter with $P/e = 10$, $e/D = 0.0422$, $\alpha/90 = 0.33$ with inlet temperature $T_i = 300$ K and $I = 850$ W/m^2.

From the plot it is found that the S_{gen} has the increasing tendency with increase of Re for both, i.e., rough and smooth absorber plate solar air heaters, but the entropy generation values for smooth and rough solar collectors having same values of S_{gen} upto Re = 2500 (approx.). In other words, it can be said that upto Re = 2500 there is no effect of the roughness rib on the absorber and it acts like solar air heater of conventional type that is the absorber plate without roughness. For Re $<$ 2500 (approx.) there is no significant difference of entropy generation between the smooth plate and roughened absorber plate solar air heaters. Another result of the graph indicates that second law efficiency values is higher for the conventional solar air heater for Re $>$ 21 000 (approx.) over the roughened solar air heater and it follows the same trend as the rough solar air heater.

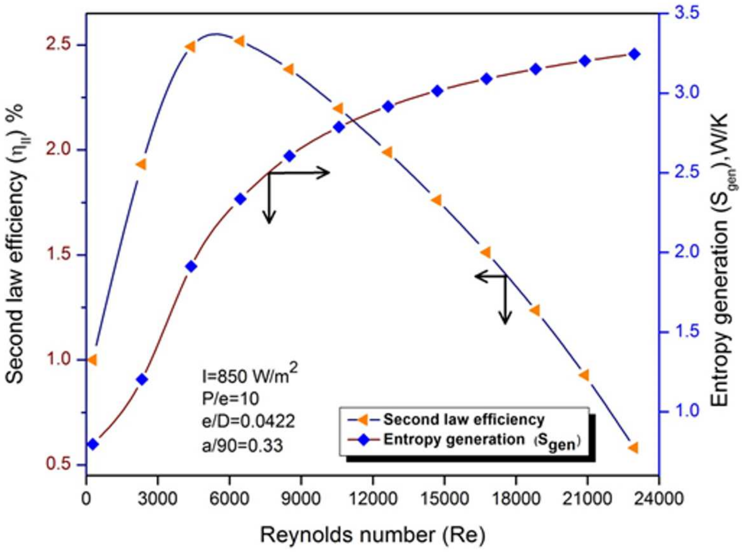

Figure 10: (a) Variation of second law efficiency and entropy generation with Re for roughened solar air heater for roughness parameters $P/e = 10$, $e/D = 0.0422$, $\alpha/90 = 0.33$, $T_i = 300$ K and Insolation $I = 850$ W/m^2.

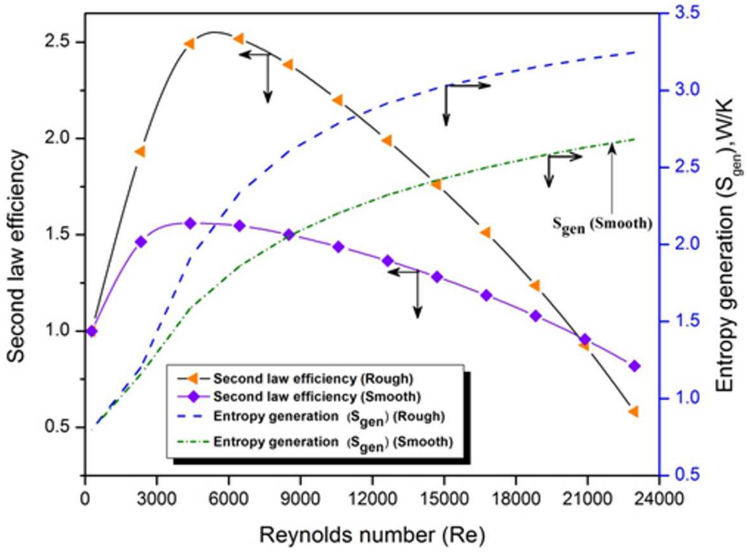

Figure 10: (b) Variation of entropy generation and second law with Re for roughened and smooth plate solar air heaters for roughness parameters $P/e = 10$, $e/D = 0.0422$, $\alpha/90 = 0.33$, and insolation $I = 850$ W/m^2.

4.1 Effect of roughness parameters on Bejan number

The effect of variations in e/D and $\alpha/90$ on Bejan number, Be, as a function of Re has been plotted in Figs. 11 and 12 respectively. From the plot (Fig. 11) it is found that Be has the decreasing tendency with increase in Re for both, i.e., roughened and smooth absorber plate solar air heaters, but Be having same values for both collectors upto Re = 6.000 (approx.). Another result can be obtain from the curves that Be values of $e/D = 0.0422$ is lower as compared to $e/D = 0.0256$ and conventional SAH for Re < 6.000 (approx.). In other words as we increase the Re the Be is decreasing sharply from one (unity) toward zero. It means the entropy generation number due to pressure drop/friction Ns_p in the duct is more dominating over the entropy generation number due to heat transfer Ns_h.

This behavior is due to the fact that the highest value of e/D (in the present investigation $e/D = 0.0422$) produces more barrier in the flow consequently delivering highest friction factor, hence values of Be are lower as compared to other e/D and smooth plate SAH.

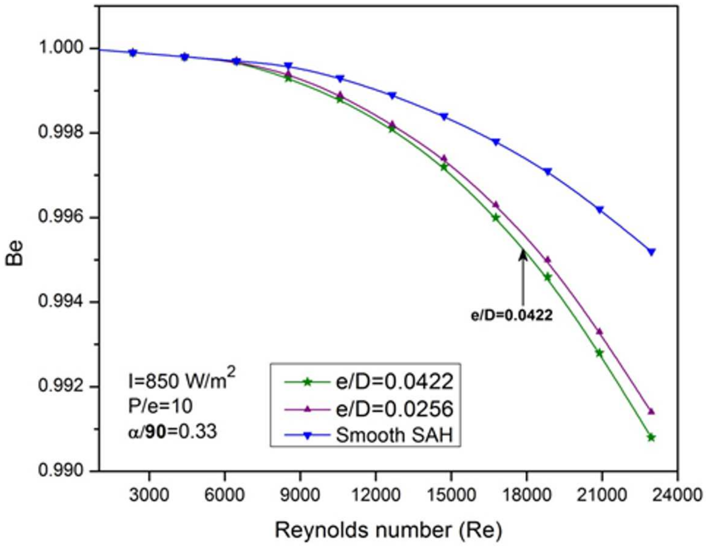

Figure 11: Effect of e/D on Bejan number and comparison of roughened with simple solar air heater as a function of Re.

Figure 12 shows the influence of roughness parameter $\alpha/90$ on Be as function of Re. Similar decreasing trend is obtained for both SAHs with increase in the values of Re. The values of Be for $\alpha/90 = 0.33$ is lower as

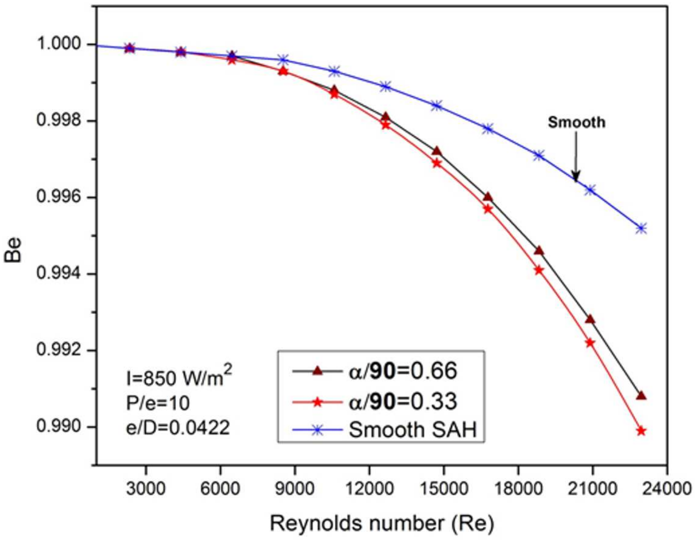

Figure 12: Effect of $\alpha/90$ on Bejan number and comparison of roughened with simple solar air heater as a function of Re.

compared to $\alpha/90 = 0.66$ and simple SAH after Re < 6.000 (approx.). The $\alpha/90 = 0.33$ is having lowest value of Be because at this value of inclination it produces highest friction in the flow.

5 Conclusions

This article presents the comprehensive entropy generation analysis and evaluation of second law efficiency using the principle of second law of thermodynamics, for a solar air heater having arc shape wire roughened absorber plate. The emphasis has been given to analyse entropy generation and to study the effects of roughness parameters viz. relative roughness height, e/D, relative roughness pitch, P/e, and relative angle of attack $\alpha/90$ and also operating parameters, e.g., Reynolds number, solar irradiation on the entropy generation. The following conclusions can be drawn:

- The second law efficiency increases with increase in Re upto its maxima, however at the higher values of Re smooth plate solar air heater is more efficient in comparison to roughened solar air heater. Highest η_{II} is obtained as 2.51 % for roughened solar air heater at Re = 6460 and $I = 850$ W/m^2 while for smooth plate SAH it is having 1.56% for Re $= 4398$ and $I = 850$ W/m^2.

- Entropy generation, entropy generation number and irreversibility increase continuously with increase in the Reynolds number. This trend is followed by both the roughened and smooth absorber plate solar air heaters. The entropy generation is minimum at relative roughness height of 0.0422 and relative angle of attack of 0.33, and relative roughness pitch of 10 which leads into the maximum second law efficiency. Bejan number is having decreasing trend with increase in the values of Reynolds. Minimum is obtained at relative roughness height of 0.0422, relative angle of attack of 0.33, and relative roughness pitch of 10 in the case of rough SAH.

Received 13 November 2016

References

[1] Duffie J.A., Beckman W.A.: *Solar Engineering of Thermal Processes*, 2nd Edn., John Wiley, New York 1991.

[2] Sukhatme S.P., Nayak J.P.: *Solar Energy.* 3rd Edn., Tata McGraw Hill, New Delhi 2011.

[3] Prasad R.K.: *Thermal Performance Characteristics of Unidirectional Flow Porous Bed Solar Energy Collectors for Heating Air.* Ph.D. thesis, Indian Institute of Technology, Roorkee 1991.

[4] Prasad R.K, Saini J.S.: *Packed-bed solar air heater with unidirectional flow arrangement.* In: Proc. Nat. Sem. on Energy Conversion in Buildings, The Institute of Engineers, I.I.T., Roorkee 1992, 29–33.

[5] Sahu M.K., Prasad R.K.: *Exergy based performance evaluation of solar air heater with arc shaped wire roughened absorber plate.* Renew. Energ. **96**(2016), 233–243.

[6] Bejan A.: *Advanced Engineering Thermodynamics.* Wiley Interscience, 1988.

[7] Bejan A.: *Entropy Generation Minimization.* CRC Press, New York 1996.

[8] Bejan A.: *A study of entropy generation in fundamental convective heat transfer.* J. Heat Transfer **101**(1979), 4, 718–725.

[9] Sahin A.Z.: *Irreversibilities in various duct geometries with constant wall heat flux and laminar flow.* Energ. **23**(1998), 6, 465–473.

[10] A.Z. Sahin: *The effect of variable viscosity on the entropy generation and pumping power in a laminar fluid flow through a duct subjected to constant heat flux.* Heat Mass Transfer **35**(1999), 6, 499–506.

[11] Oztop H.F., Sahin A.Z., Dagtekin I.: *Entropy generation through hexagonal cross-sectional duct for constant wall temperature in laminar flow.* Int. J. Energy Res. **28**(2004), 8, 725–737.

[12] Dagtekin I., Oztop H.F., Sahin A.Z.: *An analysis of entropy generation through a circular duct with different shaped longitudinal fins for laminar flow.* Int. J. Heat Mass Tran. **48**(2005), 1, 171–181.

[13] Ko T.H., Ting K.: *Entropy generation and optimal analysis for laminar forced convection in curved rectangular ducts: A numerical study.* Int. J. Therm. Sci. **45**(2006), 2, 138–150.

[14] Haydar Kucuk: *Numerical analysis of entropy generation in concentric curved annular ducts.* J. Mech. Sci. Technol. **24**(2010), 9, 1927–1937.

[15] Mina S., Mahmoudi A.H., Raouf A.H.: *Entropy generation due to natural convection cooling of a nanofluid.* Int. Commun. Heat Mass **38**(2011), 7, 972–983.

[16] Omid M., Kianifar A., Sahin A.Z.,Somchai W.: *Entropy generation during Al_2O_3/water nanofluid flow in a solar collector: Effects of tube roughness, nanoparticle size, and different thermophysical models.* Int. J. Heat Mass Tran. **78**(2014), 64–75.

[17] Velmurugana P., Kalaivanana R.: *Energy and exergy analysis of multi pass flat plate solar air heater — An analytical approach.* Int. J. Green Energy **12**(2015), 8, 810–820.

[18] Layek A., Saini J.S., Solanki S.C.: *Second law optimization of a solar air heater having chamfered rib–groove roughness on absorber plate.* Renew. Energ. **32**(2007), 12, 1967–1980.

[19] Naphon P.: *On the performance and entropy generation of the double-pass solar air heater with longitudinal fins.* Renew. Energ. **30**(2005), 9, 1345–1357.

[20] Behura A.K., Prasad B.N., Prasad L.: *Heat transfer, friction factor and thermal performance of three sides artificially roughened solar air heaters.* Solar Energy **130**(2016), 46–59.

[21] Kumar A., Saini R.P., Saini J.S.: *Development of correlations for Nusselt number and friction factor for solar air heater with roughened duct having multi v-shaped with gap rib as artificial roughness.* Renew. Energ. **58**(2013), 151–163.

[22] Sciacovelli A., Verda V., Sciubba E.: *Entropy generation analysis as a design tool — a review.* Renew. Sustain. Energy Rev. **43**(2015), 1167–1181.

[23] Rosen M.A.: *Second law analysis, approaches and implications.* Int. J. Energy Res. **23**(1991), 5, 415–429.

[24] Bejan A., Kearney D.W., Kreith F.: *Second law analysis and synthesis of solar collector systems.* J. Sol. Energ-T ASME **103**(1981), 1, 23–28.

[25] Incropera F.P., DeWitt D.P.: *Fundamentals of heat and mass transfer.* 5th Edn., John Wiley & Sons, New York 2006.

[26] Saini S., Saini R.P.: *Development of correlations for Nusselt number and friction factor for solar air heater with roughened duct having arc-shaped wire as artificial roughness.* Sol. Energy **82**(2008), 12, 1118–1130.

[27] Malhotra A., Garg H.P., Palit A.: *Heat loss calculation of flat plate solar collectors.* J. Therm. Energ. **2**(1981), 2, 59–62.

[28] Rybiński W., Mikielewicz J.: *Analytical solutions of heat transfer for laminar flow in rectangular channels.* Arch. Thermodyn. **35**(2014), 4, 29–42.

[29] Zima W., Dziewa P.: *Mathematical modelling of heat transfer in liquid flat-plate solar collector tubes.* Arch. Thermodyn. **31**(2010), 2, 45–62.

archives
of thermodynamics
Vol. **38**(2017), No. 3, 49–62
DOI: 10.1515/aoter-2017-0015

The effect of different organic fluids on performances of binary slag washing water power plants

ZI-AO LI^{a,b}, YANNA LIU^{a,b,c}, PENG DONG^{b}, YINGJIE ZHANG^{b}, and SONG XIAO^{a,b*}

[a] School of Mechanical & Vehicle Engineering, Linyi University, Linyi, 276000, China

[b] Faculty of Metallurgical and Energy Engineering, Kunming University of Science and Technology, Kunming, 650093, China

[c] Faculty of Chemical Engineering, Kunming University of Science and Technology, Kunming, 650500, China

Abstract In this paper, 3 typical organic fluids were selected as working fluids for a sample slag washing water binary power plants. In this system, the working fluids obtain the thermal energy from slag washing water sources. Thus, it plays a significant role on the cycle performance to select the suitable working fluid. Energy and exergy efficiencies of 3 typical organic fluids were calculated. Dry type fluids (i.e., R227ea) showed higher energy and exergy efficiencies. Conversely, wet fluids (i.e., R143a and R290) indicated lower energy and exergy efficiencies, respectively.

Keywords: Slag washing water; Efficiency; Organic fluids; Binary power cycle

Nomenclature

E – energy rate, kW
Ex – exergy rate, kW
h – specific enthalpy, kJ/kg
m – mass flow rate, kg/s

---

*Corresponding Author. Email xskmust@163.com

p – pressure, MPa
s – specific entropy, kJ/(kg K)
Q – heat transfer rate, kW
T – temperature, K
W – work rate, power, kW

Greek symbols

η – energy or first law efficiency, %
ψ – flow evergy, kJ/kg
ε – evergy or second law efficiency, %

Subscripts

cw – cooling water
$dest$ – destroyed, destruction
in – inlet
out – outlet
sww – slag washing water
wf – working fluid

1 Introduction

Organic Rankine cycle (ORC) is an important technology for conversion of energy which belongs to the low-grade heat resource into electricity. Both ORC and conventional steam Rankine cycle have the same operational principle. The only difference is that ORC uses organic working fluid with lower boiling temperature instead of water of conventional steam Rankine cycle. In utilization of the low temperature heat source, ORC shows great flexibility [1]. There are some low temperature heat sources which can be used for ORC such as solar radiation [2–4], geothermal energy [5–7], biomass combustion [8–10] and industrial waste heat [1,11–13], etc. Recently, some researches about ORC system have been explored [14–16].

In industry the source of waste heat occurs in very large volumes with a wide temperature distribution. For example, water is usually used to cool the slag and the temperature of the cooling-water washing the slag is generally between 80 and 90 °C in steel industry. It can be employed to heat buildings or preheat any other process. Furthermore, it can be used to produce electricity by organic Rankine cycle (ORC).

Slag washing water generally comprises numerous corrosive chemicals, because the binary power cycle is used to recover the waste heat from slag washing water. In this cycle, slag washing water never contacts with the system components except for the heat exchanger and the damaging effects of these chemicals can be prevented by binary power cycle. In a binary cycle power plant, the heat of slag washing water is transferred to a low boiling point and high vapor pressure organic fluid when compared to water at a given temperature [12,13].

The choice of working fluid affects considerably the system performance, therefore, the organic fluids play a key role in the cycle. The density of the organic fluid must be high either in the liquid or vapour phase. High liquid or vapor density lead to increase of mass flow rate and reduction of the size of equipment [17,18]. If the temperature and other parameters are defined, organic fluids with high latent heat and high density give high unit work output [19]. Low heat capacity of the organic fluid enables a near vertical saturated liquid line which has affected same high latent heat [18]. Briefly, organic fluids with high density, low liquid specific heat, and high latent heat are expected to give a high turbine work output [19].

In this paper, three typical organic fluids were selected as working fluid for a sample slag washing water binary power plants. In this system, the second working fluid obtains the thermal energy from slag washing water sources. Energy and exergy efficiencies of these typical organic fluids were calculated.

2 System description

The schematic representation of the ORC power plant supplied with energy of slag washing water (SWW) of blast furnace is shown in Fig. 1. The binary slag washing water power plant system consists of pump, evaporator, turbine and condenser. In this plant, the following working conditions are assumed for the aim of selecting and screening of optimum organic working fluids based on characteristic operation conditions of binary power cycle. These working conditions are specified considering reality plant operation conditions, since there is now an actual Kalina cycle in operation, it ought to be possible to make a comparison between it and ORC plants that have been in operation for some time and they show parallelism with the reality binary power plants examined by, e.g., [20,21] with respect to being same thermodynamic phase at the same status in the cycle.

For a general steady-state, steady-flow process, the three balance equations, namely mass, energy, and exergy balance equations, are employed to find the heat input, rate of exergy decrease, rate of irreversibility, and energy and exergy efficiencies [22,23]. In general, the mass balance equation

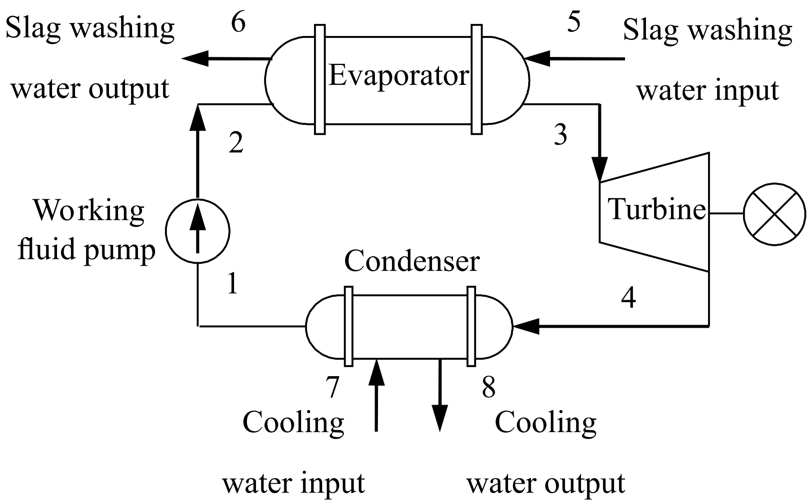

Figure 1: Schematic of analyzed slag washing water binary power cycle.

can be expressed as

$$\sum m_{in} = \sum m_{out} \ , \tag{1}$$

where m is the mass flow rate and the subscripts *in* and *out* stand for inlet and outlet. The general energy balance with negligible kinetic and potential energy changes can be expressed by

$$Q - W = \sum m_{in} h_{in} - \sum m_{out} h_{out} \ , \tag{2}$$

where Q and W are the heat transfer rate and work rate and h is the specific enthalpy.

The energy efficiency of the system η_{sys} can be defined as the ratio of total net heat input to total work output

$$\eta_{sys} = \frac{W}{Q} \ . \tag{3}$$

In this context, the specific exergy can be defined as follows:

$$\psi = (h - h_0) - T_0 (s - s_0) \ , \tag{4}$$

where subscript 0 stands for the restricted reference state, T_0 is the reference state temperature, and h_0 and s_0 are enthalpy and entropy at the restricted reference state of p_0 and T_0.

Multiplying specific exergy by the mass flow rate of the fluids gives the rate of total exergy:

$$Ex = m\psi \; . \tag{5}$$

The general exergy rate balance may be expressed as follows:

$$Ex_{dest} = Ex_{heat} - Ex_{work} + Ex_{mass,in} - Ex_{mass,out} \; . \tag{6}$$

Exergy destruction (or irreversibility) of the system can be defined as follows:

$$Ex_{dest} = \sum Ex_{in} - \sum Ex_{out} \; . \tag{7}$$

Generally, the exergy efficiency (also called second law and exergetic efficiency) may be presented as the ratio of total exergy output to total energy input.

$$\varepsilon = \frac{Ex_{output}}{E_{input}} \; . \tag{8}$$

In the considered plant, there is no environmental discharge. Slag washing water is completely returned to slag washing water pool. The power plant operates on a liquid-dominated and low-temperature resource and slag washing water remains as a liquid throughout the plant. The temperature of slag washing water entering the plant is 90 °C (i.e., $t_5 = 90\,^{\circ}\mathrm{C}$) with a mass flow rate $m_5 = 100$ kg/s, and pressure of slag washing water is 500 kPa (i.e., $p_5 = 500$ kPa) at the entrance of evaporator. Slag washing water leaves the evaporator at 60 °C (i.e., $t_6 = 60\,^{\circ}\mathrm{C}$).

Based on the Rankine cycle, the organic working fluid circulates in a closed loop. Working fluid enters the pump as saturated liquid at 10 °C ($t_1 = 10\,^{\circ}\mathrm{C}$) and is pumped to 1 MPa ($p_2 = 1$ MPa), which is the evaporator pressure. The isentropic efficiency of the pump is assumed to be 75%. The organic working fluid enters the evaporator with 1 MPa ($p_2 = 1$ MPa) and leaves after it is evaporated and superheated to 90 °C ($t_3 = 90\,^{\circ}\mathrm{C}$). The superheated organic working fluid passes through the turbine. The isentropic efficiency of the turbine is assumed to be 85%. After the organic working fluid expands in the turbine, it passes through the water-cooled condenser. It leaves the water-cooled condenser as saturated liquid at 10 °C ($t_1 = 10\,^{\circ}\mathrm{C}$). The cooling water enters the water-cooled condenser at 7 °C ($t_7 = 7\,^{\circ}\mathrm{C}$) and leaves at 15 °C ($t_8 = 15\,^{\circ}\mathrm{C}$).

The binary slag washing water power plant system has been divided into four subsystems. Mass, energy, and exergy equations and efficiencies have been defined for the evaporator as:

$$\begin{aligned}
&m_2 = m_3 = m_{wf}\ ,\\
&m_5 = m_6 = m_{sww}\ ,\\
&m_{sww}\,(h_5 - h_6) = m_{wf}\,(h_3 - h_2)\ ,\\
&Ex_{dest} = (Ex_2 + Ex_5) - (Ex_3 + Ex_6)\ ,\\
&\varepsilon = \frac{Ex_3 - Ex_2}{Ex_5 - Ex_6}\ ,
\end{aligned} \tag{9}$$

where m is the mass flow rate and the subscripts wf and sww stand for the working fluid and slag washing water, respectively.

Then, mass, energy, and exergy equations and efficiencies of the turbine can be expressed by

$$\begin{aligned}
&m_3 = m_4 = m_{wf}\ ,\\
&W_{turbine} = m_{wf}\,(h_3 - h_4)\ ,\\
&Ex_{dest} = (Ex_3 - Ex_4) - W_{turbine}\ ,\\
&\varepsilon = \frac{W_{turbine}}{Ex_3 - Ex_4}\ .
\end{aligned} \tag{10}$$

Mass, energy, and exergy equations and efficiencies of the pump are defined similarly

$$\begin{aligned}
&m_1 = m_2 = m_{wf}\,,\\
&W_{pump} = m_{wf}\,(h_2 - h_1)\,,\\
&Ex_{dest} = W_{pump} - (Ex_2 - Ex_1)\,,\\
&\varepsilon = \frac{Ex_2 - Ex_1}{W_{pump}}\ .
\end{aligned} \tag{11}$$

For the condenser, the mass, energy, and exergy equations and efficiencies are as follows

$$\begin{aligned}
&m_4 = m_1 = m_{wf}\,,\\
&m_7 = m_8 = m_{cw}\,,\\
&m_w(h_8 - h_7) = m_{wf}(h_4 - h_1)\,,\\
&Ex_{dest} = (Ex_4 + Ex_7) - (Ex_1 + Ex_8)\,,\\
&\varepsilon = \frac{Ex_8 - Ex_7}{Ex_4 - Ex_1}\,,
\end{aligned} \tag{12}$$

where m is the mass flow rate and the subscripts w stands for the cool water. Here, the overall exergy efficiency of the entire cycle may be written as

$$\varepsilon_{cyc} = \frac{W_{turbine} - W_{pump}}{m_{wf}\Big[h_1 - h_2 - T_0\left(s_1 - s_2\right)\Big]} \; . \tag{13}$$

3 Results and discussion

In this section, we studied the effect of different organic working fluids on the performance of binary slag washing water power plants. Under the same input conditions, mass, energy, and exergy balance equations were solved to validate the computations.

Selection of the organic working fluid affects the performance of the binary slag washing water power plant to a great extent. For the purpose of this investigation, three typical organic fluids were selected and analyzed as working fluid in the binary slag washing water power plant given in Fig. 1. These organic fluids were selected and analyzed because they are fluids which enable to satisfy operating conditions of studied power plant. Critical pressure for all selected working fluids is higher than 1 MPa and only R143a has critical temperature lower than 90 °C for the safety of the system. As a result of above reasons, the environmental, thermophysical, and safety properties of selected organic fluids are given in Tab. 1.

Table 1: Physical, safety, and environmental data of investigated 3 typical organic fluids.

Name	Safety	Ozone depletion potential	Freezing point, K	Boiling point, K	Critical temperature, K	Critical pressure, kPa	Fluid type
R227ea	–	0	146.35	256.81	374.90	2925.0	dry
R143a	A2	0	161.34	225.91	345.86	3761.0	wet
R290	A3	0	85.53	231.04	369.89	4251.1	wet

In Tabs. 2–4, the exergy rates of all organic fluids were calculated for each state. Note that state numbers refer to Fig. 1 and state 0, $0'$ and $0''$ indicate the restricted reference state for the slag washing water, the cooling water, and the organic working fluid, respectively. In this investigation, the temperature and pressure of restricted dead state were taken to be $t_0 = 5\,^\circ\mathrm{C}$ and $p_0 = 0.1$ MPa (101.25 kPa). Engineering Equation Solver (EES) commercial software package was used to calculate the properties of organic working fluids, slag washing water, and cooling water.

Using the values given in Tabs. 2–4, the exergy destruction for all organic fluids used in binary slag washing water power plant was determined. The exergy destructions for the various components of the plant were shown in Fig. 2. The results showed that higher exergy destruction occurs in the evaporator. Other subsystems of the plant show lower exergy destruction than the evaporator. Therefore, the evaporator plays a key role on the performance of the plant.

Table 2: Calculated exergy rates and thermodynamics properties for R227ea. State numbers refer to Fig. 1.

State no.	Working fluid	Phase	T, K	p, MPa	h, kJ/kg	s, kJ/kg K	m, kg/s	Specific exergy, kJ/kg	Exergy rate, kW
0	Slag washing water	Reference state	278	0.101	20.49	0.07398	–	–	–
$0'$	Cooling water	Reference state	278	0.101	20.49	0.07398	–	–	–
$0''$	R227ea	Reference state	278	0.101	330.2	1.507	–	–	–
1	R227ea	Saturated liquid	283	0.279	211.1	1.04	71.11	10.73	762.7
2	R227ea	Liquid	283.3	1.0	211.7	1.04	71.11	11.34	805.4
3	R227ea	Superheated vapor	358	1.0	388.6	1.589	71.11	35.6	2531.8
4	R227ea	Superheated vapor	332.9	0.279	373.6	1.589	71.11	20.6	1465.2
5	Slag washing water	Liquid	363	0.5	377.4	1.193	100	45.82	4582
6	Slag washing water	Liquid	333	0.5	251.6	0.831	100	20.66	2066
7	Cooling water	Liquid	280	0.5	29.9	0.106	343.9	0.51	174.9
8	Cooling water	Liquid	288	0.5	63.5	0.224	343.9	1.304	448.6

The exergy destruction in evaporator is a large portion of overall exergy

Table 3: Calculated exergy rates and thermodynamics properties for R143a. State numbers refer to Fig. 1.

State no.	Working fluid	Phase	T, K	p, MPa	h, kJ/kg	s, kJ/kg K	m, kg/s	Specific exergy, kJ/kg	Exergy rate, kW
0	Slag washing water	Reference state	278	0.101	20.49	0.07398	–	–	–
0′	Cooling water	Reference state	278	0.101	20.49	0.07398	–	–	–
0″	R143a	Reference state	278	0.101	405.89	1.921	–	–	–
1	R143a	Saturated liquid	283	0.837	215.2	1.054	47.56	50.34	2394
2	R143a	Liquid	283.1	1.0	215.4	1.054	47.56	50.55	2403.5
3	R143a	Superheated vapor	358	1.0	479.9	1.936	47.56	69.84	3321.6
4	R143a	Superheated vapor	356.1	0.837	474	1.936	47.56	63.94	3041
5	Slag washing water	Liquid	363	0.5	377.4	1.193	100	45.82	4582
6	Slag washing water	Liquid	333	0.5	251.6	0.831	100	20.66	2066
7	Cooling water	Liquid	280	0.5	29.9	0.106	366.3	0.51	186.2
8	Cooling water	Liquid	288	0.5	63.5	0.224	366.3	1.304	477.8

destruction of the cycle (Fig. 2). Revealing minimum exergy destruction in evaporator for the fluid such as R227ea results in minimum exergy destruction percentage for the overall overall system. It can be also shown in Fig. 3 that R227ea gives rise to low exergy losses relatively. It is expected that R227ea has the best performance, due to its minimum exergy destruction.

It is important to note that net work affects directly performance of the binary cycle. Net work is defined as the difference between work input and work output. The net work between work produced in the turbine and work consumed in the pump is different in this cycle. The net work rate

Table 4: Calculated exergy rates and thermodynamics properties for R290. State numbers refer to Fig. 1.

State no.	Working fluid	Phase	T, K	p, MPa	h, kJ/kg	s, kJ/kg K	m, kg/s	Specific exergy, kJ/kg	Exergy rate, kW
0	Slag washing water	Reference state	278	0.101	20.49	0.07398	–	–	–
$0'$	Cooling water	Reference state	278	0.101	20.49	0.07398	–	–	–
$0''$	R290	Reference state	278	0.101	597.23	2.73	–	–	–
1	R290	Saturated liquid	283	0.637	225.6	1.091	24.89	84.01	2091.1
2	R290	Liquid	283.2	1.0	226.3	1.091	24.89	84.71	2108.5
3	R290	Superheated vapor	358	1.0	731.8	2.74	24.89	131.79	3280.3
4	R290	Superheated vapor	345.4	0.637	704	2.74	24.89	103.99	2588.3
5	Slag washing water	Liquid	363	0.5	377.4	1.193	100	45.82	4582
6	Slag washing water	Liquid	333	0.5	251.6	0.831	100	20.66	2066
7	Cooling water	Liquid	280	0.5	29.9	0.106	354.4	0.51	180.2
8	Cooling water	Liquid	288	0.5	63.5	0.224	354.4	1.304	462.3

of investigated organic fluids is shown in Fig. 4. As a result of analysis, R227ea features the maximum net work rate and R143a has the minimum net work rate.

First and second law efficiencies of the overall cycle were calculated as shown in Fig. 5. We can find that R227ea exhibits the best first and second law efficiencies. It has 8.14% first law efficiency and 40.69% second law efficiency. On the other hand, R143a shows the worst first law efficiency 2.16% and second law efficiency 10.77%.

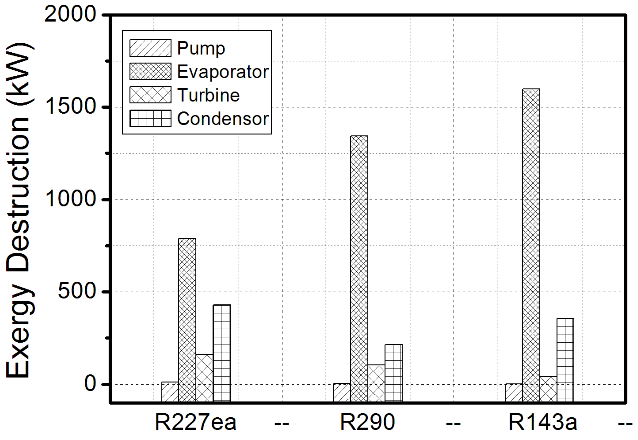

Figure 2: Exergy destruction of screened organic fluids at various components of the plants.

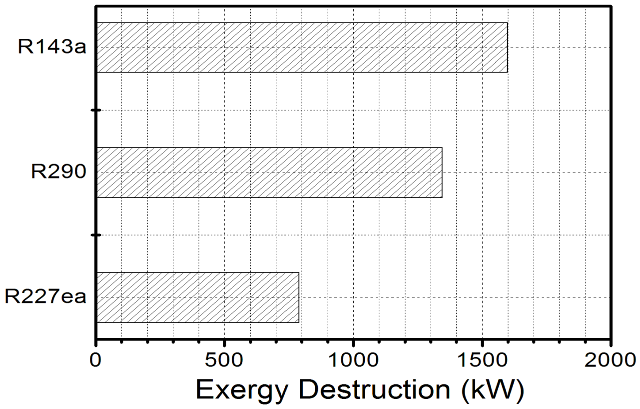

Figure 3: Exergy destruction of the system with different organic fluids.

4 Conclusions

1. In the considered slag washing water binary power plant, energy (first law) efficiencies are obtained in the range of 2–8%, and exergy (second law) efficiencies are gained in the range of 10–40%. The considered

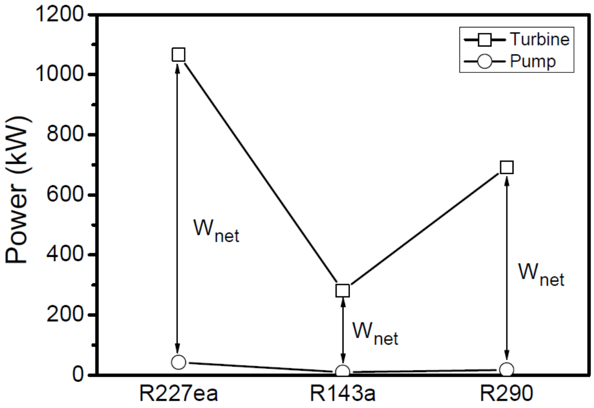

Figure 4: Net work rates of investigated organic fluids.

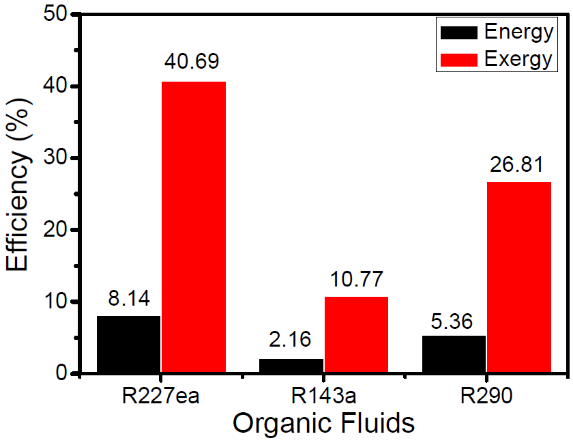

Figure 5: Energy and exergy efficiency of the investigated organic fluids.

slag washing water binary power plant which uses low-temperature slag washing water resource as a heat source exhibits higher exergy efficiency than energy efficiency.

2. According to the analysis, it is observed that selection of the organic fluids influence the system performance. Dry type organic fluid R227ea among the screened organic fluids demonstrates higher first and second law efficiencies than wet type organic fluids R290 and R143a. As a result, dry type organic fluids should be preferred as

working fluid in the binary power cycle, which produces electricity from low-temperature slag washing water resource.

3. It has been determined that the evaporator is of great importance in terms of system performance. As the exergy destruction that has been caused by the refrigerants in the evaporator increase, energy and exergy efficiencies decrease. Organic fluid R227ea which caused the minimum exergy destruction in the evaporator has exhibited the highest energy and exergy efficiencies.

4. In contrast, R143a which caused the maximum exergy destruction in the evaporator has shown the lowest energy and exergy efficiencies. Therefore, exergy destruction in the evaporator should be taken into consideration during the selection of the working fluid.

Acknowledgements Authors acknowledge the support of Item sponsored by National Natural Science Foundation (Grant No. 51568032, 51376040 and 51676031).

Received 1 December 2016

References

[1] Wang D, Ling X, Peng H.: *Performance analysis of double organic Rankine cycle for discontinuous low temperature waste heat recovery.* Appl. Therm. Eng. **48**(2012), 63–71.

[2] Ksayer E.: *Design of an ORC system operating with solar heat and producing sanitary hot water.* Energy Proc. **6**(2011), 389–395.

[3] Agustín MD, Lourdes G.: *Analysis and optimization of the low-temperature solar organic Rankine cycle (ORC).* Energy Convers. Manage. **51**(2010), 12, 2846–2856.

[4] Astolfi M, Xodo L, Romano MC, Macchi E.: *Technical and economical analysis of a solar–geothermal hybrid plant based on an organic Rankine cycle.* Geothermics **40**(2011), 2, 58–68.

[5] Kanoglu M, Bolattürk A.: *Performance and parametric investigation of a binary geothermal power plant by exergy.* Renew Energy **33**(2008), 11, 2366–2374.

[6] Kanoglu M.: *Exergy analysis of a dual-level binary geothermal power plant.* Geothermics **31**(2002), 6, 709–724.

[7] Gabbrielli R.: *A novel design approach for small scale low enthalpy binary geothermal power plants.* Energy Convers. Manage. **64**(2012), 263–272.

[8] Qiu G., Shao Y., Li J., Liu H., Saffa B.R.: *Experimental investigation of a biomassfired ORC-based micro-CHP.* Fuel **96**(2012), 374–382.

[9] Drescher U., Bruggemann D.: *Fluid selection for the organic Rankine cycle in biomass power and heat plants.* Appl Therm. Eng. **27**(2007), 1, 223–228.

[10] Al-Sulaimana F.A., Dinçer I., Hamdullahpur F.: *Energy and exergy analysis of a biomass trigeneration system using an organic Rankine cycle.* Energy **45**(2012), 1, 975–985.

[11] Wei D., Lu X., Lu Z., Gu J.: *Performance analysis and optimization of organic Rankine cycle (ORC) for waste heat recovery.* Energy Convers. Manage. **48**(2007), 4, 1113–1119.

[12] Yari M.: *Exergetic analysis of various types of geothermal power plants.* Renew. Energ. **35**(2010), 1, 112–121.

[13] Gu Z., Sato S.: *Performance of supercritical cycles for geothermal binary design.* Energy Convers. Manage. **43**(2002), 7, 961–971.

[14] Mikielewicz D., Mikielewicz J., Wajs J.: *Experiences from operation of different expansion devices for application in domestic micro CHP.* Arch. Thermodyn. **31**(2010), 4, 3–13.

[15] Wajs J., Mikielewicz D., Bajor M., Kneba Z.: *Experimental investigation of domestic micro-CHP based on the gas boiler fitted with ORC module.* Arch. Thermodyn. **37**(2016), 3, 79-93.

[16] Mocarski S., Borsukiewicz-Gozdur A.: *Selected aspects of operation of supercritical (transcritical) organic Rankine cycle.* Arch. Thermodyn. **36**(2015), 2, 85–103.

[17] Yamamoto T., Furuhata T., Arai N.: *Design and testing of the organic Rankine cycle.* Energy **26**(2001), 3, 239–251.

[18] Papadopoulos A.I, Stijepovic M., Linke P.: *On the systematic design and selection of optimal working fluids for organic Rankine cycles.* Appl. Therm. Eng. **30**(2010), 6–7, 760–769.

[19] Chen H., Goswami D.Y., Stefanakos E.K.: *A review of thermodynamic cycles and working fluids for the conversion of low-grade heat.* Renew. Sustain. Energy Rev. **14**(2010), 9, 3059–3067.

[20] Yildirim D., Ozgener L.: *Thermodynamics and exergoeconomic analysis of geothermal power plants.* Renew. Sustain. Energy Rev. **16**(2012), 8, 6438–6454.

[21] DiPippo R.: *Second law assessment of binary plants generating power from low-temperature geothermal fluids.* Geothermics **33**(2004), 5, 565–586.

[22] Molina M.J., Rowland F.S.: *Stratospheric sink for chlorofluoromethanes: chlorine atom catalyzed destruction of ozone.* Nature **249**(1974), 810–812.

[23] *REFPROP version 8.0. NIST standard reference database 23.* America: U.S. 2007.

archives
of thermodynamics
Vol. **38**(2017), No. 3, 63–75
DOI: 10.1515/aoter-2017-0016

Impact of waste heat recovery systems on energy efficiency improvement of a heavy-duty diesel engine

ZHESHU MA[a*], **HUA CHEN**[b] **and YONG ZHANG**[a]

[a] College of Automobile and Traffic Engineering, Nanjing Forestry University, Nanjing, Jiangsu, 210037, China

[b] School of Accounting, Nanjing University of Finance and Economics, Nanjing, China

Abstract The increase of ship's energy utilization efficiency and the reduction of greenhouse gas emissions have been high lightened in recent years and have become an increasingly important subject for ship designers and owners. The International Maritime Organization (IMO) is seeking measures to reduce the CO_2 emissions from ships, and their proposed energy efficiency design index (EEDI) and energy efficiency operational indicator (EEOI) aim at ensuring that future vessels will be more efficient. Waste heat recovery can be employed not only to improve energy utilization efficiency but also to reduce greenhouse gas emissions. In this paper, a typical conceptual large container ship employing a low speed marine diesel engine as the main propulsion machinery is introduced and three possible types of waste heat recovery systems are designed. To calculate the EEDI and EEOI of the given large container ship, two software packages are developed. From the viewpoint of operation and maintenance, lowering the ship speed and improving container load rate can greatly reduce EEOI and further reduce total fuel consumption. Although the large container ship itself can reach the IMO requirements of EEDI at the first stage with a reduction factor 10% under the reference line value, the proposed waste heat recovery systems can improve the ship EEDI reduction factor to 20% under the reference line value.

---

[*] Corresponding Author. Email mazheshu@126.com

Keywords: Energy efficiency design index; Energy efficiency operational indicator; Waste heat recovery system; Performance analysis; Reduction factor

Nomenclature

ANI – value of electricity recovered by WHRS annually
ANC_I – exergy loss cost
ANC_{INV} – original equipment cost
ANC_o – annual operating cost
ANC_T – annual total cost
$Capacity$ – DWT (dead weight ton) of a ship, t
C_F – nondimensional conversion factor of fuel consumption and CO_2 emission based on fuel carbon content
D – sailed distance in nautical miles, nmi
FC – total fuel consumption in a voyage, g
f_i – factor accounting for any technical/regulatory limitation on ship capacity
f_j – correction factor relating to ship design
f_w – nondimensional coefficient
f_{eff} – availability factor of innovative energy efficiency technology
GWP_{100} – 100 years' global warming potential value
MCR – maximum continuous rating power, kW
m_{cargo} – goods a cargo transported or TEU for standard containers, t
nME – numbers of main engines equipped in a ship
ODP – ozone depletion potential value
P – 75% of the rated installed power for each main engine, kW
P_c – critical pressure, Pa
SFC – certified specific fuel consumption, g/kWh
T_a – boiling point at 101.325 kPa
T_c – critical boiling point
UCB – unit cost benefit
V – voyage speed in knots, kn (1 kn = 1.852 km/h)
W_{net} – net heat energy recovered by WHRS, kW
W_{total} – total exergy of the exhaust gas

Subscripts

ME_i – main engine numbered i

1 Introduction

Deriving from the increasing interest in emission reduction and ship operating costs reduction, International Maritime Organization (IMO) has amended two rules to ensure optimal utilization of the fuel used for main engines and auxiliary engines on board ships, i.e., energy efficiency design index (EEDI) and energy efficiency operational indicator (EEOI), which are getting even more important with EEDI in place from 2013. The lower the values of EEDI and EEOI, the higher the level of fuel utilization for a specific vessel is. To reduce the values of EEDI and EEOI, various contributing factors can be identified as follows.

To reduce the value of EEDI, several technology strategies can be taken into accounts according to different stages which are demanded by IMO. For instance, a container ship which is above 15000 DWT (dead weight tonnage) should reduce its EEDI by 10% compared to the reference line value at first stage (from Jan. 1, 2015 to Dec. 31, 2019) and reduce its EEDI by 20% compared to the reference line value at second stage (from Jan. 1, 2020 to Dec. 31, 2024)[1]. To meet these tough requests, some measures can be taken at first stage, i.e., installation of generators driven by main engine, reduction of resistance, improvement of propulsive efficiency, adoption of microbubble lubrication system and other energy saving technologies while waste heat recovery system, renewable energy (such as wind power, solar power, etc.), the reduction of speed, the use of liquefied natural gas (LNG) fuel, etc. can be taken at second stage.

To reduce the value of EEOI, however, five main operating methods will be firstly considered, i.e., increase of sailed distance and load rate, reduction of time in port and speed, and utilization of waste heat recovery system.

Considering the aspects mentioned above, installation of waste heat recovery system could both reduce the values of EEDI and EEOI for a specific ship so that the level of energy utilization onboard could be further improved while ship's emission and operating costs could be further cut down.

In this paper, a new generation of 10000 TEU (twenty feet equivalent unit) container ship being built is the main study object which has won critical acclaim for environmentally friendly and energy saving. The main engine is an intelligence diesel engine made by MAN B&W with excellent performances of high energy efficiency, low specific fuel oil consumption, low exhaust gas temperature and low emission. In order to analyze the impact of waste heat recovery system on EEDI and EEOI for this container ship, three exhaust gas waste heat recovery conceptual systems had been proposed and the influences of waste heat recovery system on EEDI and EEOI had been analyzed, meanwhile, some constructive conclusions had been drawn.

2 The proposed conceptual systems of WHRS

Main engine's low exhaust gas temperature is one of the most important factors which affect the choice of the type of waste heat recovery systems (WHRS), especially for large or ultralarge merchant ships. Due to the very low exhaust gas temperature for this container ship's main engine (i.e., 266.8 °C at normal continuous rating at ISO conditions) [2], organic Rankine cycle (ORC) installation had been considered. Three exhaust gas waste heat recovery conceptual systems had been proposed according to different methods.

2.1 The WHRS with combined turbines

Figure 1 shows the WHRS with combined turbines designed for the studied container ship. By bypassing a part of exhaust gas after turbochargers, the total amount of air and exhaust gas will be reduced, the exhaust gas temperature after turbochargers and bypass will increase. The mixed exhaust gas entering the exhaust boiler could have an increase of temperature up to 65 °C compared to the standard engine at the expense of reducing the energy efficiency of the main engine, increasing specific fuel oil consumption, increasing the efficiency of the turbo-chargers, installing power turbine [3].

2.2 The WHRS based on Rankine cycle

Figure 2 shows the WHRS based on Rankine cycle designed for the studied container ship. Exhaust gas after turbochargers enters boiler directly so that superheated steam's temperature would be relatively lower compared to combined turbines waste heat recovery conceptual system.

2.3 The WHRS based on organic Rankine cycle

Figure 3 shows the WHRS based on organic Rankine cycle designed for the studied container ship. Different from the two waste heat recovery conceptual systems mentioned above, organic Rankine cycle waste heat recovery conceptual system is not a cogeneration system, i.e., the saturated steam for heating service is produced by auxiliary boiler separately. What's more, organic working fluid could keep dry at the end of expanding process so that there is no need to superheat it.

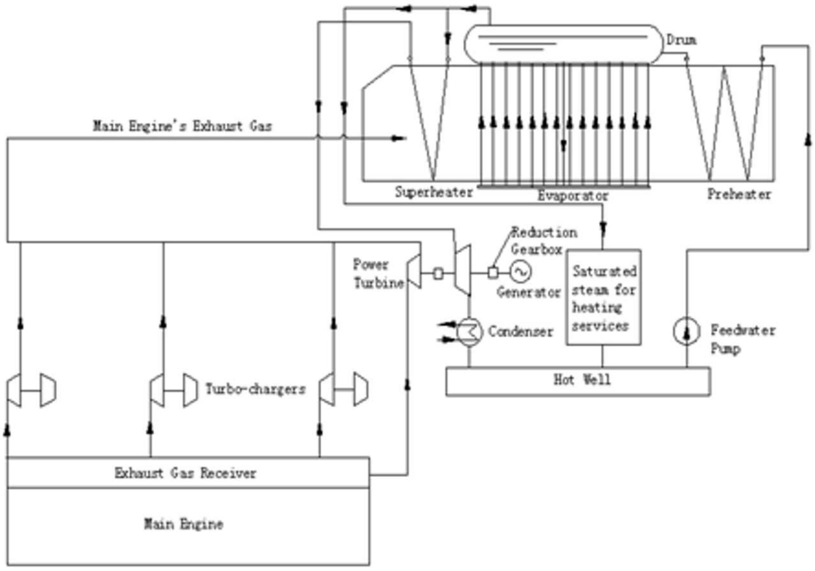

Figure 1: Diagram of combined turbines waste heat recovery conceptual system.

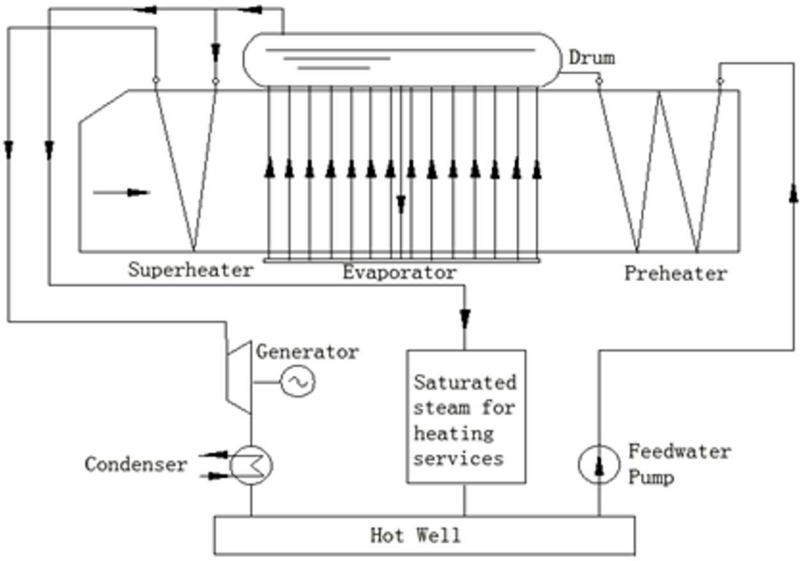

Figure 2: Diagram of Rankine cycle waste heat recovery conceptual system.

The organic compound selection has been proven to be vital to ORC plant efficiency and optimum performance [7]. Preselection of organic compound is performed under the base of same exhaust gas boiler outlet temperature according to the following criteria: (1) the organic compound should have a critical temperature near the exhaust gas temperature; (2) the standard boiling point should near the ambient air temperature; (3) it should be one of the available organic compound that has been previously studied in the scientific literature or organic compounds that are used in commercial ORC power plants, such as Solkatherm, n-pentane or R134a [8-10].

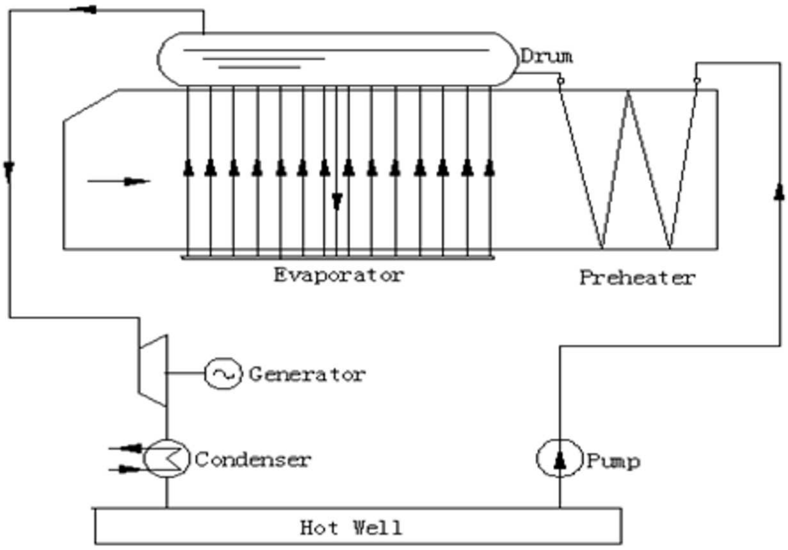

Figure 3: Diagram of organic Rankine cycle waste heat recovery conceptual system.

Table 1 shows the selected organic working fluids which may be adapted for this main engine. T_a means boiling point at 101.325 kPa, T_c means critical boiling point, P_c means critical pressure, *ODP* means ozone depletion potential value and *GWP100* means 100 years' global warming potential value.

Table 1: Thermodynamic properties of used working fluids.

Fluid	T_a, °C	T_c, °C	P_c, MPa	*ODP**	*GWP100*	Fluid type
R123	27.79	183.7	3.668	0.012	120	isentropic fluid
R141b	32.07	204.2	4.249	0.086	630	dry fluid
R245fa	14.91	154.1	3.639	0	950	isentropic fluid
n-pentane	35.87	196.5	3.364	0	11	dry fluid
isopentane	27.86	187.2	3.370	0	11	dry fluid

* ozone depletion potential

3 The research development of EEDI and EEOI

3.1 The research development of EEDI

After several amendments to MARPOL Annex VI Regulations for the prevention of air pollution from ships by IMO, *EEDI* has been a measure of ships energy efficiency (g/ton×nmi) and scheduled to enter into force on 1 Jan. 2013. The value of *EEDI* is calculated by the following formula [1]:

$$\begin{aligned} EEDI = & \Bigg\{ \Big(\prod_{j=1}^{M} f_j\Big)\Big(\sum_{i=1}^{nME} P_{ME_i}\cdot C_{FME_i}\cdot SFC_{ME_i}\Big) \\ & + \Big(P_{AE}\cdot C_{FAE}\cdot SFC_{AE}\Big) \\ & + \Bigg[\Big(\prod_{j=1}^{M} f_j \prod_{i=1}^{nPTI} P_{PTI_i} - \sum_{i=1}^{neff} f_{eff_i}\cdot P_{AEeff_i}\Big) C_{FAE}\cdot SFC_{AE}\Bigg] \\ & - \Big(\sum_{i=1}^{neff} f_{eff_i}\cdot P_{eff_i}\cdot C_{FME}\cdot SFC_{NE}\Big)\Bigg\} \\ & \times \frac{1}{f_i\cdot Capacity\cdot V_{ref}\cdot f_w}\ , \end{aligned} \tag{1}$$

where *nME* and refer to number of main engines equipped in ship. *Capacity* means DWT of a ship. It must be noted that 65% of the dead weight ton should be used as *Capacity* in the case of container ships. C_F is a nondimensional conversion factor between fuel consumption and CO_2 emission based on fuel carbon content, for heavy oil $C_F = 3.114$. The subscripts *ME* and AE refer to the main and auxiliary engine(s), respectively. P_{ME_i} is 75% of the rated installed power for each main engine (i) after having deducted any installed shaft generator(s), $P_{ME_i} = 0.75(MCR_{ME_i} - P_{PTO_i})$. MCR_{ME_i} is the maximum continuous rating (MCR) power of main engine i. P_{PTO_i} is 75% output of each shaft generator installed divided by the relevant efficiency of that shaft generator. P_{PTI_i} is 75% of the rated power consumption of each shaft motor divide by the weighted averaged efficiency of the generator(s). P_{eff_i} is the output of the innovative mechanical energy efficient technology for propulsion at 75% main engine power. P_{AEeff_i} is the auxiliary power reduction due to innovative electrical energy efficient technology measured at P_{ME_i}. P_{AE} is the required auxiliary engine power to supply normal maximum sea load including necessary power for propulsion machinery/systems and accommodation. V_{ref} is the reference speed in knots (1 knot = 1.852 km/h) in a voyage. SFC is the certified specific fuel consumption, measured in g/kWh, of the engines. f_j is a correction factor to account for ship specific design elements. According to regulations of the international marine organization (IMO), f_j can be set to be 0.77 for shuttle oil tankers with propulsion redundant system and 1.0 for other kinds of ships. A nondimensional coefficient f_w indicates the decrease of speed in representative sea conditions of wave height, wave frequency and wind speed. f_{eff_i} is the availability factor of each innovative energy efficiency technology, f_{eff_i} for waste energy recovery system should be 1.0. f_i is the capacity factor for any technical/regulatory limitation on capacity, and can be assumed 1.0 if no necessity of the factor is granted.

Equation (1) shows that the reduction of the reference speed in a voyage V_{ref}, i.e., design speed and installation of waste heat recovery system are the main measures to lower the value of EEDI with no consideration of shaft generator(s), the innovative mechanical energy efficient technology, and other correction factors. Meanwhile, several organizations have developed programs to calculate the value of EEDI for different ship designers and ship owners. For example, Baltic and International Maritime Council (BIMCO) provide one EEDI calculator for free.

To compare the *EEDI* value of real ships, the reference line value of *EEDI* recommended by international marine organization is employed in this paper.

$$EEDI_{ref} = a \cdot Capacity^{-c}\,, \tag{2}$$

where a is a coefficient related to ship type and *Capacity* means DWT of a ship. For large container ships, a is 172.21 and c is -0.2 [7].

3.2 The research development of EEOI

The EEOI (former operational CO2-Index) represents the actual transport-efficiency of a ship in service and shall be part of the ship energy efficiency management (SEEMP). The value of EEOI is calculated by the following formula [5]

$$EEOI = \frac{\sum_j FC_j \cdot C_{Fj}}{m_{cargo} \cdot D} , \tag{3}$$

where FC_j is the total fuel consumption in a voyage. C_{Fj} is a nondimensional conversion factor between fuel consumption and CO_2 emission based on fuel carbon content. m_{cargo} refers to tons of goods a cargo transported or TEU for standard containers, and D is the sailed distance in nautical miles (nmi). Equation (3) shows that five contributing aspects could be taken into account to reduce the value of EEOI. They are the increase of sailed distance and load rate, reduction of time in port and design speed, and utilization of waste heat recovery system. It must be pointed out that several organizations have developed programs to calculate the value of EEOI for different ship designers and ship owners. For example, Totem Plus Ltd provide one EEOI calculator for free [6].

4 Results and discussion

4.1 Unit cost benefit optimization of the waste heat recovery conceptual systems

Instead of the exergy efficiency optimization, this paper selects the unit cost benefit as the objective function for optimization according to the ORC WHR working conditions.

The unit cost benefit can be expressed as

$$UCB = \frac{ANB}{ANC_T} , \tag{4}$$

where ANC_T is the annual total cost of the WHRS, in USD. ANC_T consists of three parts, including the annual operating cost ANC_o, the exergy loss cost, ANC_I, and the original equipment cost ANC_{INV}. ANC_T is calculated by

$$ANC_T = ANC_o + ANC_I + ANC_{INV} . \tag{5}$$

ANB is the annual net profit and is expressed as

$$ANB = ANI - ANC_o \,, \tag{6}$$

where ANI is the value of electricity recovered by WHRS annually. ANC_o is calculated as follows

$$ANC_o = 0.1 ANC_T \,. \tag{7}$$

For the thermoeconomic optimization, assumptions are made as follows:(1) the detailed structure parameters of the ORC WHR system have been carefully determined, which means that the optimization is only related to thermodynamic paremeters; (2) the condensing temperature is 35 °C and the sea water temperature at the outlet of condenser is 30 °C.

Table 2 shows the results of optimization by net profit per cost optimization method of three exhaust gas waste heat recovery conceptual systems designed for the 10000 TEU container ship's main engine. In Tab. 2, W_{total} and W_{net} represent total exergy of the exhaust gas and net heat energy recovered by WHRS, respectively. It is obvious that organic Rankine cycle waste heat recovery conceptual system using R141b as working fluid has the best performance due to the highest value of UCB which means net profit per cost of waste heat recovery systems.

Table 2: WHRS performances optimized by net profit per cost optimization method.

WHRS type	$T_{steam.in}$, °C	UCB	ANC_T, $\times 10^6$USD	$A_{total.boiler}$, m^2	W_{net} kW	W_{total}, kW	$T_{out.boiler}$, °C
R123	176	0.347	10.84	16477	1661	2162	137.7
R141b	190.4	0.4179	10.08	17846	1842	2331	138
R245fa	146.7	0.205	8.662	13467	1317	1824	137.5
isopentane	181.6	0.3122	9.259	14987	1579	2084	136.9
n-pentane	190.2	0.3508	9.17	15659	1671	2157	137
water	220.8	0.3437	3.835	12786	1279	1408	168.4
combined turbines	270.8	0.3586	6.613	13484	3222	3389	158.5

4.2 The impact of WHRS on EEDI and EEOI

In the referred research, software packages were developed to calculate the energy efficiency design index (EEDI) and energy efficiency operational indicator (EEOI) of the given large container ship.

4.2.1 The impact of waste heat recovery conceptual systems on EEDI

According to Eq. (2), one can get the value of the reference line value of EEDI, i.e., 16.835 $gCO_2/(t\times nmi)$. Through Eq. (1), the EEDI of the 10000 TEU container ship without installing waste heat recovery conceptual systems can be calculated to be 13.60 $gCO_2/(t\times nmi)$ and, respectively. In the case of main engine installing the waste heat recovery system, taking organic Rankine cycle WHRS using R141b as working fluid (the most appropriate working fluid) for example, the EEDI value of such a container is 12.95 $gCO_2/(t\times nmi)$.

Analyzing the above three EEDI values, one can see that the 10000 TEU container ship's EEDI has decreased by 19.22% compared to the reference line value so that it has completely met IMO first stage's requirements (i.e., for a container ship which is above 15000 DWT should reduce its EEDI by 10% compared to the reference line value at first stage during Jan. 1, 2015 to Dec. 31, 2019) and very close to IMO second stage's requirements. A container ship which is above 15000 DWT should reduce its EEDI by 20% compared to the reference line value at second stage during Jan. 1, 2020 to Dec. 31, 2024).

The EEDI of the 10000 TEU container ship with R141b organic Rankine cycle WHRS can be decreased by 23.08% compared to the reference line value so that it has completely met IMO stage II's requirements by installing the waste heat recovery conceptual system.

4.2.2 The impact of waste heat recovery conceptual systems on EEOI

Suppose the normal operating state is: D_0 = 6000 nmi, R_0 =100%, ts_0 = 96 h, V_0 =23 kn (1 kn = 1.852 km/h), then the value of EEOI without waste heat recovery conceptual system can be gained, i.e., 154.8×10^{-6} ton/(TEU×nmile). After installing waste heat recovery system (e.g., organic Rankine cycle waste heat recovery conceptual system using R141b as working fluid), the value of EEOI is calculated and gained, i.e., 147.8×10^{-6}

ton/(TEU×nmi). It shows that the 10000 TEU container ship's EEOI has decreased by 4.52% after installing waste heat recovery system.

5 Conclusion

Energy efficiency design index (EEDI) and energy efficiency operational indicator (EEOI) are important measures to evaluate energy efficiency and CO_2 emissions of vessels and are advocated to make ships becoming more and more efficient.

Waste heat in emission gas of large containers is quite quantitative but with a low emission temperature. Modern WHRS is technologically possible to be equipped not only to improve total energy utilization efficiency but also to reduce greenhouse gas emissions.

In this paper, three types of WHRS are proposed to recover waste heat from a 10000 TEU conceptual large container ship driven by a modern low speed marine diesel engine. To calculate the EEDI and EEOI of the given large container ship, two software packages are developed. Results indicate that the large container ship itself can reach the IMO requirements of EEDI at the first stage with a reduction factor 10% under the reference line value, the proposed waste heat recovery systems can improve the ship EEDI reduction factor to 20% under the reference line value. WHRS could improve the overall ship efficiency and reduce emissions simultaneously.

Acknowledgments We gratefully acknowledge the financial support of the Qing-Lan Project of Jiangsu Province under contract No. 161220605, Studying Abroad Program for Excellent Young Scholars sponsored by Jiangsu Provincial Department of Education and the Nanjing Forestry University (201610298022Z).

Received 3 December 2016

References

[1] *Draft guidelines on the method of calculation of the attained energy efficiency design index for new ships [C].* Annex 1, MEPC 62/5/4, Marine Environment Protection Committee, IMO, 8 April, 2011.

[2] *MAN B&W Diesel A/S. Main Engine Room Data for 10S90ME-C9.2-TII.* Internal Data.

[3] *MAN B&W Diesel A/S. Thermo Efficiency System for Reduction of Fuel Consumption and CO2 Emission.* MAN B&W brochure, 2013.

[4] *Baltic and International Maritime Council.* EEDI Calculator, http://www.bimco.org/en/Products/EEDI.aspx.

[5] *International Maritime Organization. Guidelines for Voluntary Use of the Ship Energy Efficiency Operational Indicator (EEOI).* IMO, London 2014.

[6] *Totem Plus Ltd.* EEOI Calculator, http://www.totemplus.com.

[7] *Mepc.214(63).* Guidelines on survey and certification of the energy efficiency design index (EEDI), 2012

[8] Yang Min-Hsiung,Yeh, Rong-Hua: *Thermo-economic optimization of an organic Rankine cycle system for large marine diesel engine waste heat recovery.* Energy **82**(2015), 256–268.

[9] Zheshu Ma, Jieer Wu: *Efficiency optimization of a closed IFGT cycle working under two variable-temperature heat reservoirs.* Arch. Thermodyna. **32**(2011), 2, 3–20.

[10] Hajabdollahi Zahra, Hajabdollahi Farzaneh, Tehrani Mandi: *Thermo-economic environmental optimization of Organic Rankine Cycle for diesel waste heat recovery.* Energy **63**(2013), 142–151.

archives
of thermodynamics
Vol. **38**(2017), No. 3, 77–99
DOI: 10.1515/aoter-2017-0017

The effect of pulsed laser radiation on a thermoviscoelastic semi-infinite solid under two-temperature theory

MOHAMED I. OTHMAN[a,b],
AHMED E.E. ABOUELREGAL[c,d] *

[a] Department of Mathematics, Faculty of Science, Zagazig University, P.O. Box 44519 Zagazig, Egypt.

[b] Department of Mathematics, Faculty of Science, Taif University, 888, Taif, Saudi Arabia

[c] Department of Mathematics, Faculty of Science, Mansoura University, Mansoura 35516, Egypt

[d] Department of Mathematics, College of Science and Arts, University of Aljouf, El-Qurayat, Saudi Arabia

Abstract The purpose of this paper is to study the thermoviscoelastic interactions in a homogeneous, isotropic semi-infinite solid under two-temperature theory with heat source. The Kelvin-Voigt model of linear viscoelasticity which describes the viscoelastic nature of the material is used. The bounding plane surface of the medium is subjected to a non-Gaussian laser pulse. The generalized thermoelasticity theory with dual phase lags model is used to solve this problem. Laplace transform technique is used to obtain the general solution for a suitable set of boundary conditions. Some comparisons have been shown in figures to estimate the effects of the phase lags, viscosity, temperature discrepancy, laser-pulse and the laser intensity parameters on all the studied fields. A comparison was also made with the results obtained in the case of one temperature thermoelasticity theory.

Keywords: Generalized thermo-visco-elasticity; Two-temperature; Non-Gaussian laser pulse; Laser intensity; phase lags; Kelvin-Voigt model

---

*Corresponding Author. Email: ahabogal@mans.edu.eg

Nomenclature

b	temperature discrepancy factor
$c_1 = \sqrt{(\lambda_e + 2\mu_e)/\rho}$	longitudinal wave speed
C_E	specific heat at uniform strain
e_{ij}	linear strain tensor
$k = K/\rho C_E$	thermal diffusivity
K	thermal conductivity
L_0	laser intensity
q_i	components of heat flux vector
Q	intensity of heat source
R_a	surface reflectivity
t_p	characteristic time of the laser pulse
t_0	mechanical relaxation time due to the viscosity
T_0	environment temperature
T	absolute temperature of the medium
u, w	displacement components
(x, y, x)	Cartesian coordinates system

Greek symbols

α_1, α_2	thermoviscoelastic relaxation times
α_t	thermal expansion coefficient
δ_{ij}	Kronecker delta function
δ_1	absorption depth of heating energy
$\eta = \rho C_E/K$	thermal viscosity
$\theta = T - T_0$	temperature change
$\lambda_e,\ \mu_e$	Lameñs constant
ρ	material density
σ_{ij}	mechanical stress components
τ_q	phase lag of the heat flux
τ_θ	phase lag of gradient of temperature
φ	conductive temperature

1 Introduction

The theory of thermoelasticity deals with the effects of mechanical and thermal disturbances on elastic body. Biot has introduced a theory of coupled thermoelasticity to overcome the first shortcoming [1]. The governing equations for this theory are coupled, eliminating the first paradox of the classical theory. However, this theory shares the second shortcoming since the heat equation for the coupled theory is based on Fourier's law of heat conduction and is also parabolic. Henceforth, two styles of generalized theories of thermoelasticity presented by Lord and Shulman [2] and Green and Lindsay [3], which admit the finite speed of the thermal signal, have been the center of interest of active research during the last three decades. The third generalization to the coupled theory is known as the dual phase lag (DPL) thermoelasticity, proposed by Tzou [4], in which Fourier's law is replaced by an approximation to a modification of Fourier law with two different translations for the heat flux and the temperature gradient. These theories remove the paradox of the infinite speed of heat propagation that is inherent in the conventional coupled dynamical theory of thermoelasticity, which was introduced by Biot [1]. In the generalized theories, a modified heat conduction law, which includes both the heat flux and its time derivative, replaced the conventional Fourier law.

Chen and Gurtin [5] and Chen *et al.* [6,7] have formulated a theory of heat conduction in deformable bodies, which depends upon two distinct temperatures, the conductive and thermodynamic temperatures. For time-independent situations, the difference between these two temperatures is proportional to the heat supply, and in the absence of any heat supply, the two temperatures are identical. For time-dependent problems, however, and for wave propagation problems in particular, the two temperatures are in general different regardless of the presence of heat supply. The two temperatures and the strain are found to have representations in the form of a traveling wave plus a response, which occurs instantaneously throughout the body [8]. Warren and Chen have investigated the wave propagation in the two-temperature theory of thermoelasticity (2TT) [9]. Youssef has extended this theory in the context of the generalized theory of thermoelasticity [10].

Pulsed laser irradiation is employed over a wide spectrum of materials processing applications, including surface hardening, alloying, curing, synthesis of compound and superconductor films. An extensive review of pulsed laser processing of semiconductors is given in [11]. Very rapid thermal processes, under the action of an ultrashort laser pulse, are interesting from the standpoint of thermoelasticity, since they require an analysis of the coupled temperature and deformation fields as in [12]. This mechanism has attracted considerable attention due to extensive application of pulsed laser technologies in material processing and nondestructive detection and characterization as in [13]. The so-called ultrashort lasers are those with pulse duration ranging from nanoseconds to femtoseconds in general. The non-Fourier effect of heat conduction takes into account the effect of mean free time in the energy carrier's collision process, which can eliminate this contradiction. Wang and Xu studied the stress wave induced by nano-, pico-, and femto-second laser pulses in a semi-infinite solid [13]. The solution takes into account the non-Fourier effect in heat conduction and the coupling effect between temperature and strain rate. It is known that characteristic elastic waveforms are generated when a pulsed laser irradiates a metal surface. McDonald studied the importance of thermal diffusion to the thermoelastic wave generation [14]. Allam and Abouelregal have discussed the thermoelastic waves induced by pulsed laser and varying heat of nonhomogeneous microscale beam resonators [15]. Othman *et al.* studied the effect of rotation on a semiconducting medium with two-temperature under L-S theory. The effect of internal friction on the propagation of plane waves in an elastic medium may also be considered owing to the fact that dissipation accompanies vibrations in solid media due to the conversion of elastic energy to heat energy [16].

The effect of internal friction on the propagation of plane waves in an elastic medium may also be considered owing to the fact that dissipation accompanies vibrations in solid media due to the conversion of elastic energy to heat energy.

The viscoelastic nature of a medium has special significance in wave propagation in a solid medium. The Kelvin-Voigt model is one of the macroscopic mechanical models often used to describe the viscoelastic behavior of a material. This model represents the delayed elastic response subjected to stress when the deformation is time dependent but recoverable. The dynamical interaction of thermal and mechanical fields in solids has a number of significant practical applications in modern aeronautics, astronautics, nuclear reactors, and high energy particle accelerators, for example. Abd-alla and Abo-Dahab [17,18] investigated the reflection of the generalized magneto-thermo-viscoelastic plane waves. Mukhopadhyay studied the thermal relaxation effects and compared the various theories of generalized thermoelasticity for thermo-viscoelastic interactions in an infinite viscoelastic solid of Kelvin-Voigt type with a spherical cavity [19]. Mukhopadhyay and Bera investigated the effect of distributed instantaneous continuous heat sources in an infinite conducting magneto-thermo-viscoelastic solid with relaxation time [20]. Ezzat *et al.* introduced the state-space approach for the two-dimensional model of generalized thermo-viscoelasticity with two relaxation times [21].

Othman and Song studied the effect of rotation on plane waves of the generalized electromagneto-thermo-viscoelasticity with two relaxation times [22]. Othman and Fekry explain the effect of magnetic field on generalized thermo-viscoelastic diffusion medium with voids [23].

The objective of the present investigation is to determine the components of displacement, stress, conductive temperature, thermodynamic temperature distributions and strain in an isotropic homogeneous viscoelastic half space. The governing equations are derived in the context of two-temperature generalized thermoelasticity with phase lags. The bounding plane surface is heated by a non-Gaussian laser beam. An exact solution of the problem is first obtained in the Laplace transform space. The inversion of the Laplace transform will be computed numerically by using a method based on Fourier expansion technique. The derived expressions are computed numerically for copper and the results are presented in graphical form. The effects of the two-temperature parameter, the laser-pulse, the laser intensity and viscosity parameters are estimated.

2 Governing equation of two-temperature thermoelasticity with phase lags

The basic governing equations of motion and heat conduction, in the context of the generalized theory of thermoelasticity, in the absence of body forces are given in [19].

The equations of motion without body forces take the forms

$$\mu' u_{i,jj} + (\lambda' + \mu') u_{j,ij} - \beta' \theta_{,i} = \rho \frac{\partial^2 u_i}{\partial t^2} \,. \tag{1}$$

The constitutive equations take the forms

$$\sigma_{ij} = 2\mu' e_{ij} + \delta_{ij} \left(\lambda' e_{kk} - \beta' \theta \right) \,, \tag{2}$$

where σ_{ij} is the stress tensor and δ_{ij} is Kronecker's delta function, u_i are the components of the displacement vector, t is the time, e_{ij} is the strain, $\theta = T - T_0$, T is the absolute temperature of the medium, T_0 is the reference uniform temperature of the body chosen such $|\theta/T_0| << 1$, ρ is the density. In the above equations, a prime symbol refers to spatial derivative, a dot refers to temporal derivative and summation convention is used.

The parameters λ', μ' and β' are defined as [19]

$$\lambda' = \lambda_e \Big(1 + \alpha_1 \frac{\partial}{\partial t} \Big), \quad \mu' = \mu_e \Big(1 + \alpha_2 \frac{\partial}{\partial t} \Big), \quad \beta' = \beta_e \Big(1 + \beta \frac{\partial}{\partial t} \Big) \,,$$

$$\beta_e = (3\lambda_e + 2\mu_e)\, \alpha_t, \quad \beta = (3\lambda_e \alpha_1 + 2\mu_e \alpha_2) \frac{\alpha_t}{\beta_e}, \tag{3}$$

where λ_e, μ_e being Lamé constants, α_1, α_2 are the thermoviscoelastic relaxation times, and α_t is the coefficients of linear thermal expansion.

Fourier's law states that the heat flow is proportional to the temperature gradient. The constant of proportionality depends, among other things, on a material parameter known as the thermal conductivity of the material. For heat conduction to occur there must be temperature differences between neighboring points. The classical thermoelasticity is based on the principles of the classical theory of heat conductivity, specifically on the classical Fourier law, which relates the heat flux vector $\mathbf{q}_i$ to the temperature gradient as follows:

$$\mathbf{q}_i = -K\,\theta_{,i}\ , \tag{4}$$

where K is the thermal conductivity of a solid and $\theta = T - T_0$, T is the absolute temperature of the medium, T_0 is the reference uniform temperature of the body chosen such $|\theta\,/T_0| << 1$, which together with the energy equation yields the heat conduction equation or the parabolic heat conduction equation and is diffusive with the notion of infinite speed of propagation of thermal disturbances

$$\rho\, C_E \frac{\partial \theta}{\partial t} + \beta'\, T_0 \frac{\partial}{\partial t} u_{i,i} = -\ \mathrm{q}_{i,i} +\ Q\ , \tag{5}$$

where C_E is the specific heat and Q is the intensity of heat source.

The modified form of classical thermoelasticity model is given by Tzou theory in which the Fourier law is replaced by an approximation of the equation [22]

$$\mathbf{q}_i(x, t + \tau_q) = -K\,\theta_{,i}(x, t + \tau_\theta)\ , \tag{6}$$

where τ_θ is the phase lag of the heat flux, and τ_q is phase lag of gradient of temperature. The above equation may be approximated by [22]

$$\Big(1 + \tau_q \frac{\partial}{\partial t}\Big)\ \mathbf{q}_i = -\ K\Big(1 + \tau_\theta \frac{\partial}{\partial t}\Big)\theta_{,i}\ . \tag{7}$$

In classification of real material into simple and nonsimple materials Chen and Gurtin [5] have proposed a theory of nonsimple materials for which thermodynamics and conductive temperatures are not identical unlike simple materials for which they are identical. This theory was further extended to deformable bodies by Chen *et al.* [6,7]. They have shown that the equation of heat conduction for such materials contains an additional term involving the time derivative of the Laplacian of the conductive temperature; the equation of motion also includes terms involving the space derivatives of the Lapalcian of conductive temperature, Considering isotropy and the linearity, for such materials, they have shown that the two temperatures are related by the relation [7]

$$\varphi - \theta = b\varphi_{,ii} \ , \tag{8}$$

where φ is the conductive temperature, θ is thermodynamic temperature, and $b > 0$ is the temperature discrepancy factor.

Now, we assume a new generalized heat conduction equation of the form

$$\left(1 + \tau_q \frac{\partial}{\partial t}\right)\mathbf{q}_i = -K\left(1 + \tau_\theta \frac{\partial}{\partial t}\right) \varphi_{,i} \ , \tag{9}$$

taking the divergence of both sides of the above equation, one gets

$$\left(1 + \tau_q \frac{\partial}{\partial t}\right) q_{i,i} = -K\left(1 + \tau_\theta \frac{\partial}{\partial t}\right) \varphi_{,ii} \ . \tag{10}$$

The generalized equation of heat conduction with two temperatures in the case of nonsimple medium using Eqs. (2) and (8) takes the form [22]

$$K\left(1 + \tau_\theta \frac{\partial}{\partial t}\right)\varphi = \left(1 + \tau_q \frac{\partial}{\partial t}\right)\left[\rho C_E \frac{\partial \theta}{\partial t} + \beta' T_0 \frac{\partial}{\partial t} u_{i,i} - Q\right] . \tag{11}$$

The above equation may be considered as the generalized heat conduction equation in isotropic, thermoelastic solids with two temperatures. The key element that sets the two-temperature thermoelasticity theory apart from the classical theory is the material parameter b. Specifically, in the limit as $b \to 0$, $\varphi \to \theta$, the classical theory (one-temperature generalized thermoelasticity theory 1TT) is recovered.

3 Statement of the problem

We consider a homogenous isotropic thermoviscoelastic half space occupying a half-space $x \geq 0$ and initially undisturbed and at uniform temperature T_0. The Kelvin-Voigt model of linear viscoelasticity which describes the viscoelastic nature of the material has been employed to study the problem. So, the initial conditions for all field variables are homogeneous. This half-space is irradiated uniformly the bounding plane $(x = 0)$ by a laser pulse with the non-Gaussian temporal profile. The system is initially quiescent where all the state functions are depending only on the variable x and the time t.

The displacement components for a one-dimensional medium have the forms $u_x = u(x,t)$ and $u_y = u_z = 0$. The relation between the strain and displacement can be expressed as $e = e_{xx} = \partial u/\partial x$. The constitutive equation will be

$$\sigma_{xx} = \sigma = (\lambda' + 2\mu')e - \beta'\theta \, . \tag{12}$$

The equation of motion takes the form

$$(\lambda' + 2\mu')\frac{\partial^2 u}{\partial x^2} - \beta'\frac{\partial \theta}{\partial x} = \rho \ddot{u}_i \tag{13}$$

where the double dot refers to second derivative with respect to time or may be written in the form

$$\frac{\partial^2 \sigma}{\partial x^2} = \rho\frac{\partial^2 e}{\partial t^2} \, . \tag{14}$$

The relation between the heat conduction and the thermodynamic heat takes the form

$$\varphi - \theta = b\frac{\partial^2 \varphi}{\partial x^2} \, . \tag{15}$$

The heat conduction equation (10) is given by

$$K\Big(1 + \tau_\theta\frac{\partial}{\partial t}\Big)\frac{\partial^2\varphi}{\partial x^2} = \Big(1 + \tau_q\frac{\partial}{\partial t}\Big)\Big[\rho C_E\frac{\partial}{\partial t}\Big(\varphi - b\frac{\partial^2\varphi}{\partial x^2}\Big) + \beta' T_0\frac{\partial e}{\partial t} - Q\Big] \, . \tag{16}$$

Let's introduce the following nondimensional parameters:

$$(x',u') = c_1\eta\,(x,u)\,, \ \ \Big(\,t',\tau'_q,\tau'_\theta,\beta'_1,\alpha'{}_2,\alpha'_1\Big) = c_1^2\eta\,\Big(\,t',\tau'_q,\tau'_\theta,\beta'_1,\alpha'{}_2,\alpha'_1\Big) \ ,$$

$$\theta' = \frac{\beta_e\theta}{\rho c_1^2}\,, \quad \varphi' = \frac{\beta_e\varphi}{\rho c_1^2}\,, \quad \sigma' = \frac{\sigma}{\rho c_1^2}\,, \quad Q' = \frac{Q}{K c_1^2\eta^2 T_0}\,, \tag{17}$$

where $c_1 = \sqrt{(\lambda_e + 2\mu_e)/\rho}$ is the longitudinal wave speed and $\eta = \rho C_E/K$ is the thermal viscosity. Then, Eqs. (12) and (14)–(16) can be transformed into the dimensionless forms

$$\sigma = \Big(1 + \delta_1\frac{\partial}{\partial t}\Big)e - \Big(1 + \beta\frac{\partial}{\partial t}\Big)\theta\,, \tag{18}$$

$$\frac{\partial^2\sigma}{\partial x^2} = \frac{\partial^2 e}{\partial t^2}\,, \tag{19}$$

$$\varphi - \theta = \omega \frac{\partial^2 \varphi}{\partial x^2}\,, \tag{20}$$

$$\left(1+\tau_\theta \frac{\partial}{\partial t}\right)\frac{\partial^2 \varphi}{\partial x^2} = \left(1+\tau_q \frac{\partial}{\partial t}\right)\left[\frac{\partial \theta}{\partial t} + \varepsilon\left(1+\beta\frac{\partial}{\partial t}\right)\frac{\partial e}{\partial t} - Q\right], \tag{21}$$

where $\varepsilon = \beta_e^2 T_0/\rho^2 C_E c_1^2$, $\omega = b c_1^2 \eta^2, \delta = \frac{c_2^2}{c_1^2}$, $\quad c_2^2 = \frac{\lambda_e \alpha_1 + 2\mu_e \alpha_2}{\rho}$.

Now, let us consider the medium is uniformly heated by a laser pulse with the non-Gaussian form temporal profile [25] as

$$I(t) = \frac{L_0 t}{t_p^2} e^{-t/t_p}\,, \tag{22}$$

where t_p is a characteristic time (measured by picoseconds) of the laser-pulse (the time duration of a laser pulse), L_0 is the laser intensity which is defined as the total energy carried by a laser pulse per unit area of the laser beam. The conduction heat transfer in the medium can be modeled as a one dimensional problem with the energy source, $Q(x,t)$, near the surface:

$$Q(x,t) = \frac{R_a}{\delta_1} e^{(x-h/2)/\delta_1} I(t) = \frac{R_a L_0}{\delta_1 t_p^2} t e^{(x-h/2)/\delta_1 - t/t_p}\,, \tag{23}$$

where δ_1 is the absorption depth of heating energy and R_a is the surface reflectivity [25]. Note that the laser pulse may lie on the surface of the medium ($x = 0$). In this case, the energy source takes the form

$$Q(t) = \frac{R_a L_0}{\delta_1 t_p^2} t e^{-h/(2\delta_1) - t/t_p}\,. \tag{24}$$

4 Initial and boundary conditions

The problem is solved under proper initial and boundary conditions:

$$\theta(x,t) = \varphi(x,t) = u(x,t) = 0 \quad \text{at} \quad t = 0\,,$$

$$\frac{\partial \theta(x,t)}{\partial t} = \frac{\partial \varphi(x,t)}{\partial t} = \frac{\partial u(x,t)}{\partial t} = 0 \quad \text{at} \quad t = 0\,. \tag{25}$$

The thermal and mechanical boundary conditions on the bounding plane, $x = 0$, of the assumed half-space are given as follows:

- Thermal boundary condition:
  The boundary plane $x = 0$ is subjected to a thermal shock as follows:

  $$\theta(0,t) = \theta_0 H(t) \ , \tag{26}$$

  where $H(t)$ is called the Heaviside unit step function and θ_0 is a constant.
- Mechanical boundary condition:
  The boundary plane $x = 0$ is considered to be friction free,

  $$\sigma(0,t) = 0 \ . \tag{27}$$

5 Solution of the problem in the Laplace transform domain

Applying Laplace transform with respect to variable t for Eqs. (18)–(21), one can get the system of differential equations in the transformed domain as follows:

$$\bar\sigma = (1+\delta_1 s)\,\bar e - (1+\beta s)\,\bar\theta \ , \tag{28}$$

$$\frac{\mathrm{d}^2\bar\sigma}{\mathrm{d}x^2} = s^2\bar e \ , \tag{29}$$

$$\bar\theta = \bar\varphi - \omega\frac{d^2\bar\varphi}{dx^2} \ , \tag{30}$$

$$\frac{d^2\bar\varphi}{dx^2} = \alpha_0\left[\bar\theta + \varepsilon\,(1+\beta s)\;\bar e\right] - \bar G(s) \ , \tag{31}$$

where

$$\bar G(s) = \frac{R_a L_0 e^{-h/2\delta_1}}{t_p^2 c_1 \delta_1 (1+\tau_\theta s)}\left[\frac{t_p\tau_q}{1+st_p} + \frac{t_p^2 - t_p\tau_q}{(1+st_p)^2}\right], \qquad \alpha_0 = \frac{s(1+\tau_q s)}{1+\tau_\theta s} \ . \tag{32}$$

Eliminating $\bar\theta$ and $\bar e$ from Eqs. (28)–(31), one obtains

$$\left[\frac{d^4}{dx^4} - A\frac{d^2}{dx^2} + B\right]\bar\varphi = q_2\bar G(s) \ , \tag{33}$$

where

$$A = \frac{\alpha_0\omega + q_1\alpha_0 + q_2 q_3}{\alpha_0\varepsilon\omega(1+\beta s) + q_1 q_3} \ , \qquad B = \frac{q_2\alpha_0}{\alpha_0\varepsilon\omega(1+\beta s) + q_1 q_3} \ ,$$

$$q_1 = \frac{1+\delta_1 s}{(1+\beta s)}, \quad q_2 = \frac{s^2}{(1+\beta s)}, \quad q_3 = 1+\alpha_1\omega \,. \tag{34}$$

The solution of Eq. (33) takes the following form:

$$\bar{\varphi} = A_1 e^{-m_1 x} + A_2 e^{-m_2 x} + \bar{F}_1(s) \,, \tag{35}$$

where A_1 and A_2 are parameters of s.

The solution of $\bar{\varphi}$ is used in Eq. (30) to get the solution of $\bar{\theta}$

$$\bar{\theta} = (1-\beta\, m_1^2)A_1 e^{-m_1 x} + (1-\beta\, m_2^2)A_2 e^{-m_2 x} + \bar{F}_1(s) \,. \tag{36}$$

The above two solutions are used in Eq. (31) to get the solution of $\bar{e}$ as

$$\begin{aligned} \bar{e} &= \frac{\bar{G}(s)}{\varepsilon\alpha_0(1+\beta s)} + \Big[\frac{q_3}{\varepsilon\alpha_0(1+\beta s)}D^2 - \frac{\alpha_1}{\varepsilon\alpha_0(1+\beta s)}\Big]\bar{\varphi} \\ &= \bar{F}_2(s) + \Omega_1 A_1 e^{-m_1 x} + \Omega_2 A_2 e^{-m_2 x} \,, \end{aligned} \tag{37}$$

where

$$\bar{F}_1(s) = q_2\bar{G}(s)/B, \;\; \bar{F}_2(s) = \left[\frac{B-\alpha_0 q_2}{B\varepsilon\alpha_0(1+\beta s)}\right]\bar{G}(s)\,, \; \Omega_i = \frac{q_3 m_i^2 - \alpha_0}{\varepsilon\alpha_0(1+\beta s)} \,, \tag{38}$$

$i = 1,\, 2$.

and substituting Eqs. (36) and (37) into Eq. (28), one obtains

$$\bar{\sigma} = \bar{F}(s) + \Gamma_1 A_1 e^{-m_1 x} + \Gamma_2 A_2 e^{-m_2 x} \,, \tag{39}$$

where: $\bar{F}(s) = \bar{F}_2(s)\,(1+\delta_1 s) - (1+\beta s)\,\bar{F}_1(s)$,
$\Gamma_i = \Omega_1\,(1+\delta_1 s) - (1+\beta s)\,(1-\beta\, m_i^2), \;\; i = 1,2$.

From Eq. (14) and by using the non-dimensional variables and place-Laplace transforms, one obtains the displacement in the following form:

$$\bar{u} = \frac{1}{s^2}\frac{\partial\bar{\sigma}}{\partial x} = -m_1\Gamma_1 A_1 e^{-m_1 x} - m_2\Gamma_2 A_2 e^{-m_2 x} \,. \tag{40}$$

In addition, the thermal and mechanical boundary conditions in the Laplace domain $\bar{\theta}(0,s) = \theta_0/s$ and $\bar{\sigma}(0,s) = 0$ with the aid of Eqs. (36) and (39), gives

$$\begin{aligned} A_1 &= \frac{s\,\bar{F}(s)\,(\beta m_2^2 - 1) + \bar{F}(s)\Big(s\,\bar{F}_1(s) - \theta_0\Big)}{s[\Gamma_1 - \Gamma_2 + \beta(\Gamma_2 m_1^2 - \Gamma_1 m_2^2)]} \,, \\ A_2 &= -\frac{s\,\bar{F}(s)\,(\beta m_1^2 - 1) + \bar{F}(s)\Big(s\,\bar{F}_1(s) - \theta_0\Big)}{s[\Gamma_1 - \Gamma_2 + \beta(\Gamma_2 m_1^2 - \Gamma_1 m_2^2)]} \,. \end{aligned} \tag{41}$$

This completes the solution in the Laplace transform domain.

6 Special cases

6.1 Generalized thermoelastic theory with two-temperature (2TTE)

Neglecting viscous effect by taking $\alpha_1 = \alpha_2 = 0$, we obtain the expressions for the displacement components, stresses and temperature field in the generalized magneto-thermoelastic heat conduction equation with diffusion.

6.2 Generalized thermoelastic theory with one-temperature (1TTE)

Neglecting viscous effect by taking $\alpha_1 = \alpha_2 = 0$ and $\omega \to 0$, we obtain the expressions for the displacement components, stresses and temperature field in the generalized thermoelastic with theory one-temperature.

6.3 Generalized thermoviscoelastic theory with one-temperature (1TTVE)

The generalized thermoviscoelastic theory with one-temperature can be deduced by setting the two-temperature parameter $\omega \to 0$.

7 Numerical inversion of the Laplace transform

In order to determine the conductive and thermal temperature, displacement and stress distributions in the time domain, we adopt a numerical inversion method based on a Fourier series expansion [26]. In this method, the inverse $f(t)$ of the Laplace transform $\bar{f}(s)$ is approximated by the relation

$$f(t) = \frac{e^{\zeta t}}{t_1}\left\{\tfrac{1}{2}\bar{f}(\zeta) + Re\left[\sum_{k=0}^{N} \bar{f}\left(\zeta + \frac{ik\pi}{t_1}\right) e^{ik\pi t/t_1}\right]\right\}, \quad 0 \le t \le t_1\ , \tag{42}$$

where Re is the real part and i is imaginary number unit, and N is a sufficiently large integer representing the number of terms in the truncated infinite Fourier series. It must be chosen such that

$$e^{\zeta t} e^{iN\pi t/t_1} Re\left[\bar{f}\left(\zeta + \frac{iN\pi}{t_1}\right)\right] \le \varepsilon_1\ , \tag{43}$$

where ε_1 is a persecuted small positive number that corresponds to the degree of accuracy to be achieved. The parameter ζ is a positive free parameter that must be greater than the real parts of all singularities of $\bar{f}(s)$. The optimal choice of ζ was obtained according to the criteria described in [26].

8 Numerical results and discussion

With the aim to illustrate the theoretical results obtained in the preceding sections, we now present some numerical results. Material chosen for this purpose is copper, featuring the following the physical data:

$$K = 368 \text{ N/Ks}, \quad \alpha_t = 1.78 \times 10^{-5}\,\text{K}^{-1}, \quad C_E = 383.1 \text{ m}^2/\text{K},$$

$$\rho = 8954 \text{ kg/m}^3 , \quad \lambda_e = 7.76 \times 10^{10}\,\text{N/m}^2,$$

$$\mu_e = 3.86 \times 10^{10}\,\text{N/m}^2, \ T_0 = 293 \text{ K}, \ \alpha_1 = 0.06\,\text{s}, \ \alpha_2 = 0.09\,\text{s} .$$

The computations were carried out for a wide range of x $(0 \leq x \leq 1)$ at small value of time $t = 0.15$. The physical quantities are plotted in Figs. 1–15. For all numerical calculations one takes $\delta_1 = 0.01$, $\tau_0 = 0.02$, $R_a = 0.5$, and $h = 0.1$. The field quantities such as the conductive temperature, dynamical temperature, stress, strain, and displacement distributions depend not only on the time t and space coordinate x, but also depend on the two-temperature parameter ω and the laser intensity L_0. The laser intensity L_0 is assumed to be of the form $L_0 = \xi \times 10^{11}$ J/m^2 where ξ is the laser intensity parameter. Using these values, nondimensional field variables have been evaluated and results are presented in the form of graphs. In order to analyze the effects of different parameters, such as, heat source, viscosity, two-temperature on displacement, temperatures and stress, we have considered their graphical representations into three categories.

In the first case, Figs. 1–4 plot the displacement u, thermodynamic temperature θ, conductive temperature φ and the stress σ distributions with different values of the two-temperature parameter ω to stand for the effect of this parameter on all the studied fields. The value of $\omega = 0$ indicates the old situation (one temperature thermoviscoelasticity theory 1TTVE) while $\omega = 0.02$ or 0.04 indicates the two-temperature thermoviscoelasticity theory (2TTVE). In this case one takes $\tau_q = 0.2$, $\tau_\theta = 0.1$, $\xi = 1$, and $t_p = 2$. The wave-amplitude of the displacement u decreases as ω increases. For $x > 0.1$, the thermodynamic temperature θ increases as ω

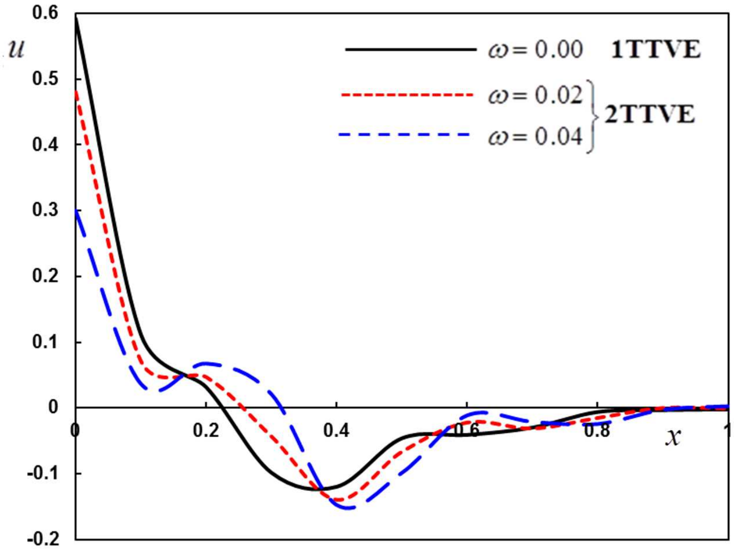

Figure 1: Dependence of displacement u on the two temperature parameter ω along distance x.

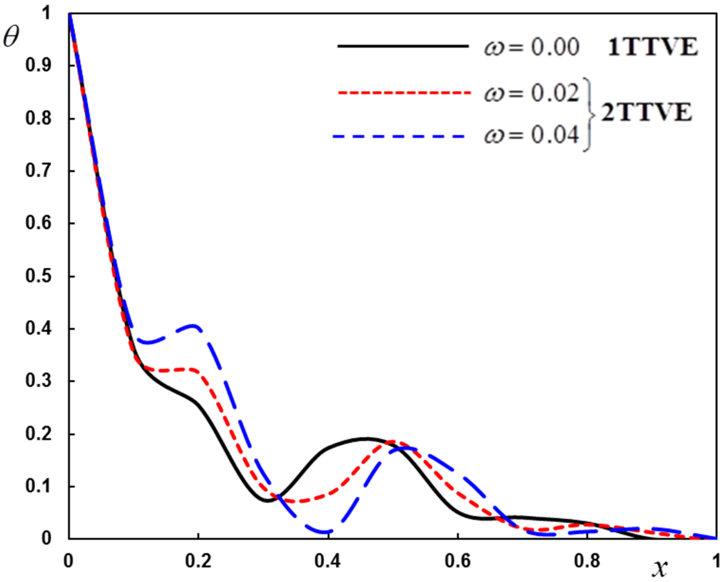

Figure 2: Dependence of thermodynamical temperature θ on the two temperature parameter ω along distance x.

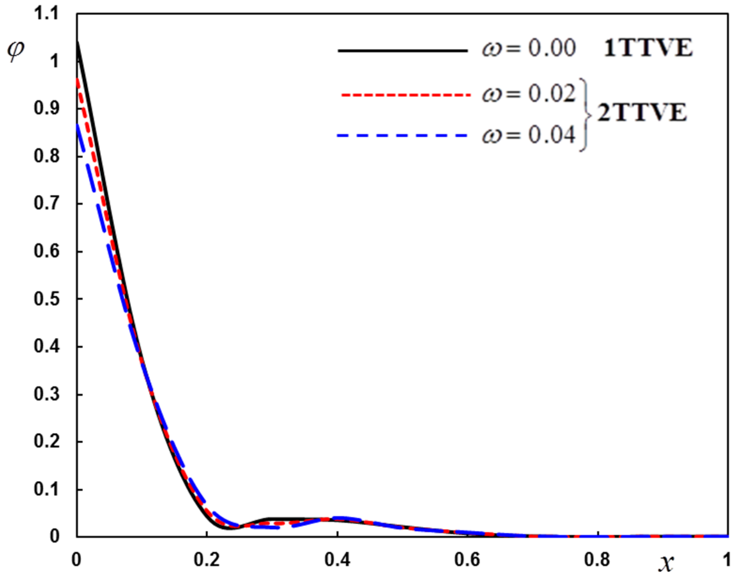

Figure 3: Dependence of conductive temperature φ on the two temperature parameter ω along distance x.

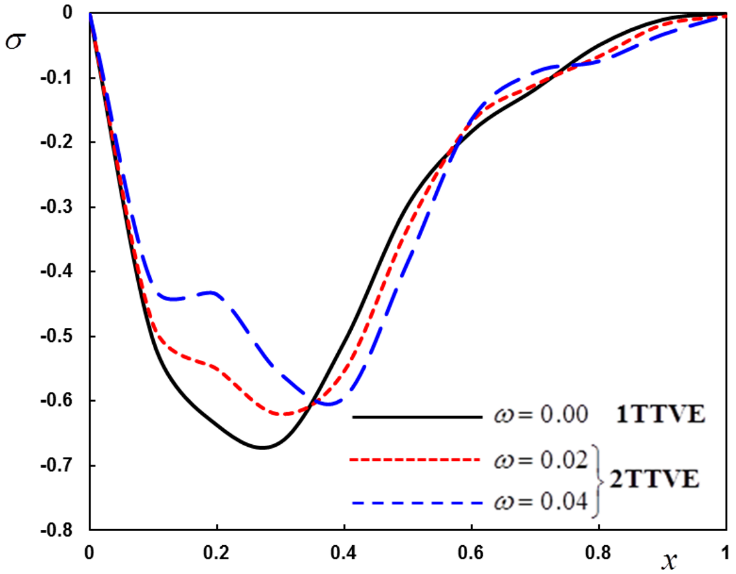

Figure 4: Dependence of the thermal stress σ on the two temperature parameter ω along distance x.

increases. Also, as ω increases the conductive temperature φ decreases in the interval $0 < x < 0.1$. In most positions, the stress σ increases as ω increases in the intervals $0 < x < 0.37$ and $0.6 < x < 0.1$ while it decreases in the interval $0.37 < x < 0.6$ and decreases in the interval $0.28 < x < 1$.

This shows the difference between the one temperature viscothermoelasticity model with phase lags 1TTVE (when $\omega = 0$) and the two-temperature generalized viscothermoelasticity 2TTVE (when $\omega = 0.02$ or 0.04). The figures show that this parameter has a significant effect on all the fields. The waves reach the steady state depending on the value of temperature discrepancy ω. Also these figures indicate that, the two-temperature generalized theory of thermoelasticity describes the behavior of the particles of an elastic body more realistically than the one-temperature theory of generalized thermoelasticity. From Fig. 4, the stress at $x = 0$ is zero as shown, which agrees with the boundary condition prescribed. This coincided with the mechanical boundary condition that the medium surface is friction free. In general, the amplitude of the wave of the displacement u is decreasing along the distance x. The thermodynamically θ and the conductive φ temperatures are directly decreasing along the distance x.

In the second case, Figs. 5–8 plot field quantities for different values of the laser intensity parameter ξ to stand for the effect of this parameter. It is found that this parameter has significant effects with fixed values of $\omega = 0.02$ and $t_p = 2$. It is observed that the nature of variations of all field variables for laser intensity parameter ξ is significantly different. All fields increase when the value of ξ increases.

In the last case, different values of the dual phase lag (DPL) of the heat flux and the temperature gradient τ_q and τ_θ, respectively, are considered. The graphs in Figs. 9-12 represent the curves predicted by three different theories of thermoelasticity obtained as special cases of the present DPL model. The computations were performed for various values of the parameters τ_q and τ_θ to obtain the coupled theory (CTE) ($\tau_q = \tau_\theta = 0$), the Lord-Shulman (LS) theory ($\tau_\theta = 0$, $\tau_q = 0.2$), and the generalized theory of thermoelasticity proposed by Tzou (DPL) ($\tau_q = 0.2$, $\tau_\theta = 0.1$).

It can be observed that the PLs parameters have a great effect on the distribution of field quantities. The mechanical distributions indicate that the wave propagates as a wave with finite velocity in medium. The values in classical theory of thermoelasticity (CTE model) are different compared to those of other theories. The fact that in generalized thermoelasticity theories (DPL and LS), the waves propagate with finite speeds is evident

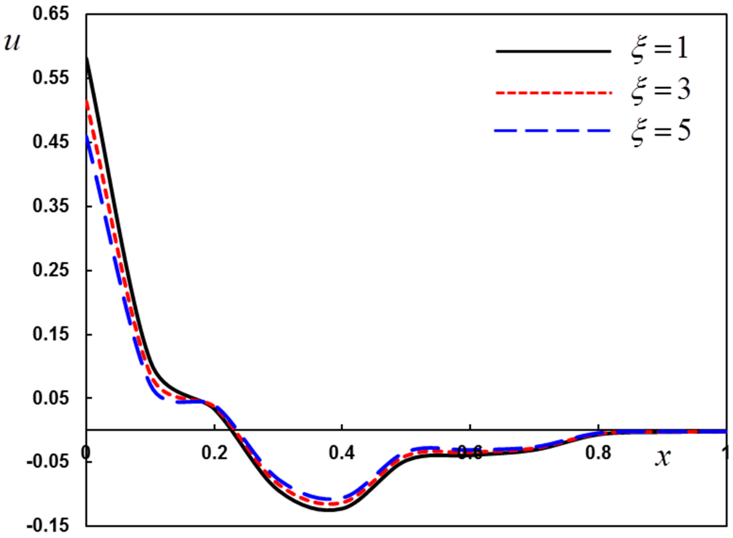

Figure 5: Dependence of displacement u on the laser intensity ξ along distance x.

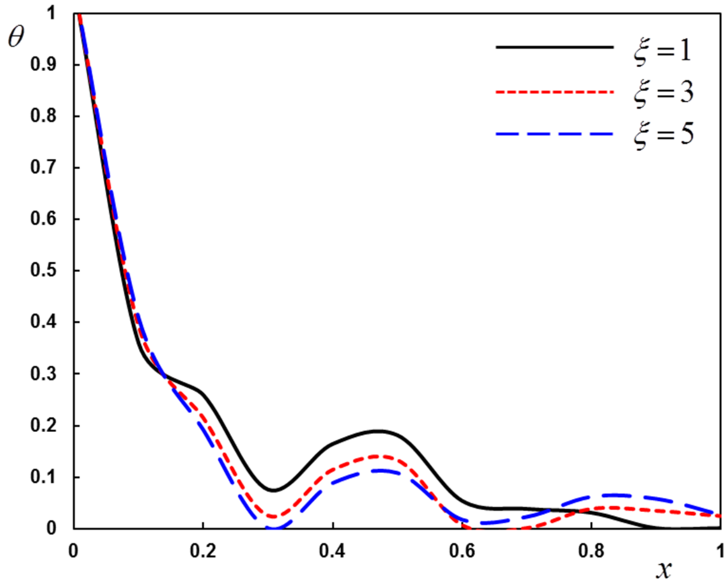

Figure 6: Dependence of thermodynamical temperature θ on the laser intensity ξ along distance x.

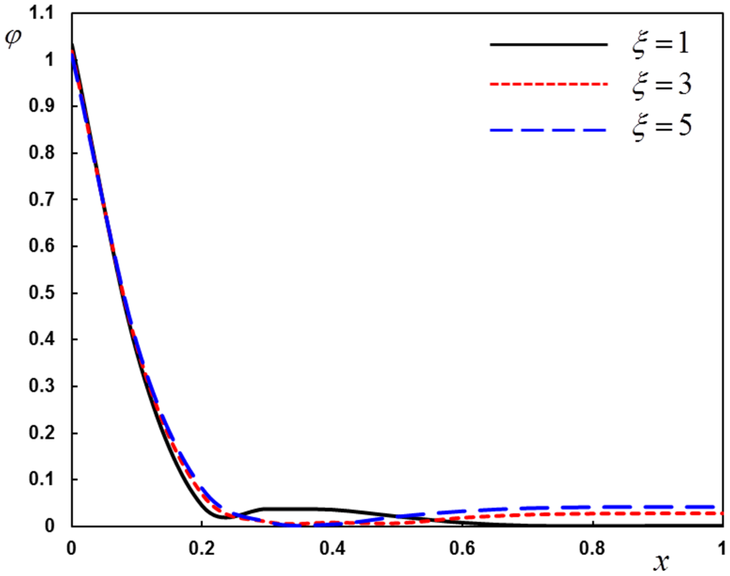

Figure 7: Dependence of conductive temperature φ on the time of the laser intensity ξ along distance x.

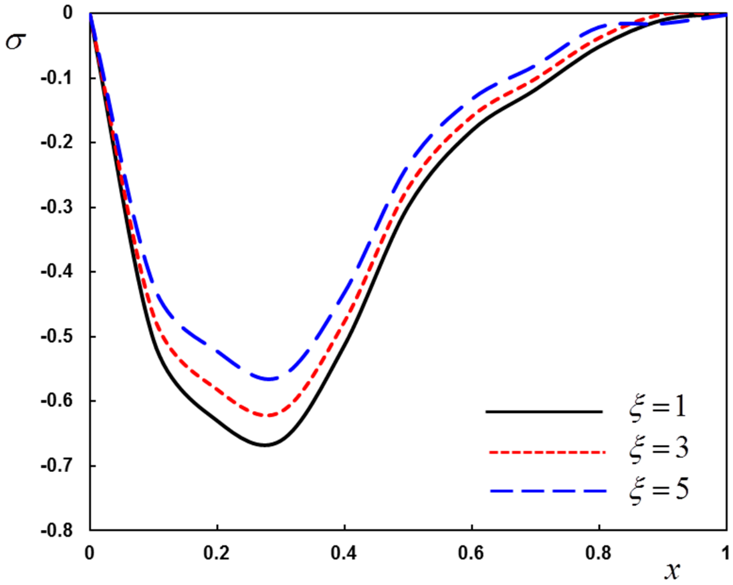

Figure 8: Dependence of the thermal stress σ on the laser intensity ξ along distance x.

in all these figures. The behavior of the three theories is generally quite similar.

9 Concluding remarks

In this paper, the theory of two-temperature thermoviscoelasticity with phase lags was constructed and applied to a specific problem of a semi-infinite solid. The effect of the laser intensity and phase lags of the heat flux and phase lage of gradient of temperatureand τ_q as well as the two-temperature parameter on the field variables has been investigated.

The results concluded from the above analysis can be summarized as follows:

1. The presence of phase lags parameters play a significant role in all physical quantities.
2. It is seen that the values of all field variables are significantly dependent on the two-temperature parameter.
3. According to the theory of thermoviscoelasticity with two-temperatures, we have to construct a new classification for materials where this parameter becomes a new indicator of its ability to conduct heat under the effect of thermoelastic properties.
4. It is also observed that the theories of coupled thermoelasticity and generalized thermoelasticity with one relaxation time can be obtained as limited cases.
5. From our results, we can consider the theory of two-temperature generalized thermoviscoelasticity as an improvement on studying elastic materials.
6. The properties of a body depend largely on the laser intensity of applied source. Therefore, the presence of the non-Gaussian laser pulse in the current model is of significance.

Received 15 April 2017

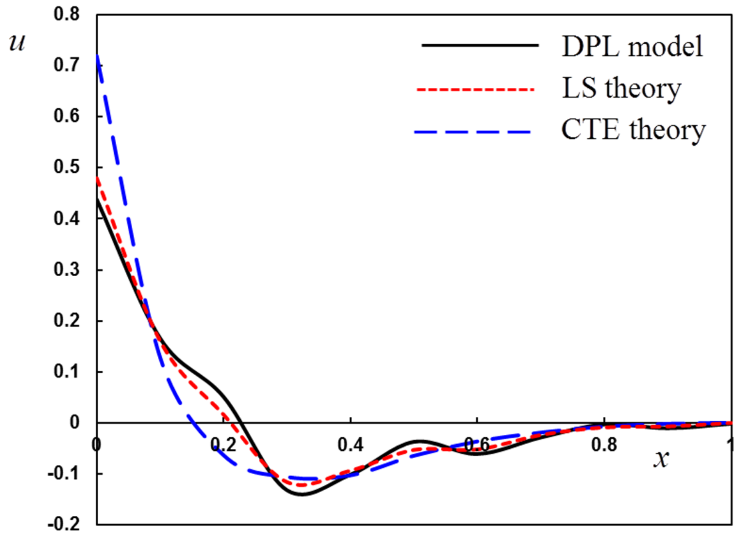

Figure 9: The displacement distribution u with distance x for different theories of thermoelasticity.

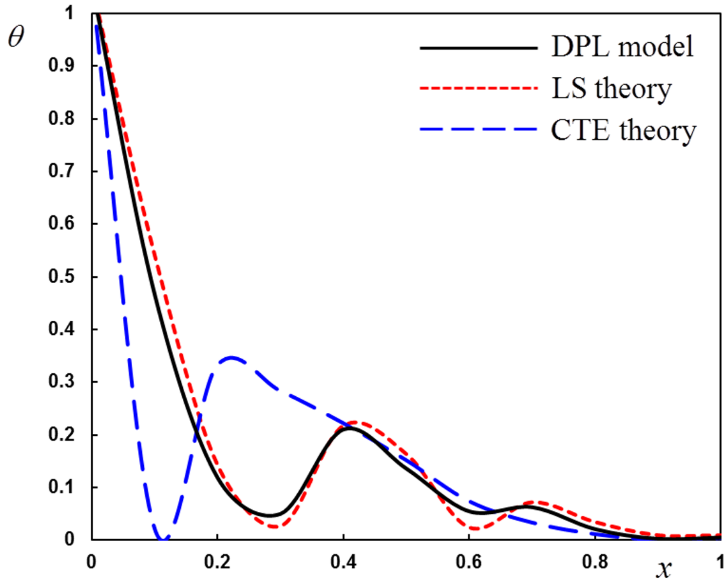

Figure 10: The thermodynamical temperature θ with distance x for different theories of thermoelasticity.

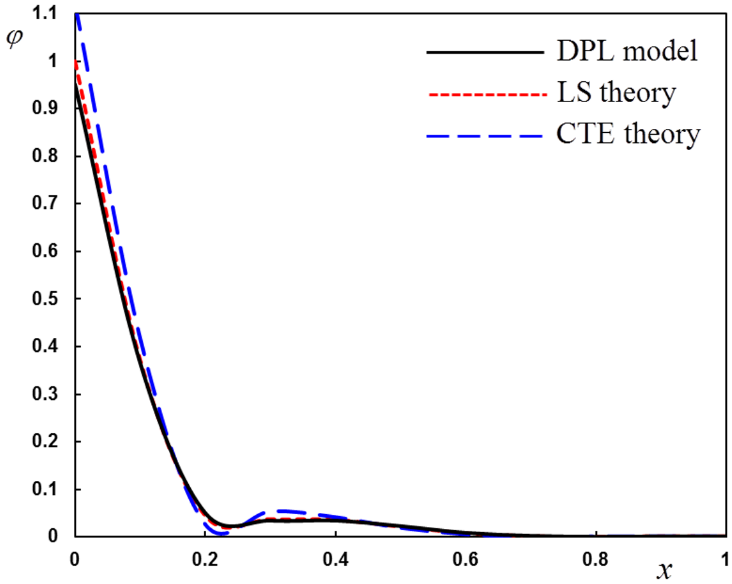

Figure 11: The conductive temperature φ with distance x for different theories of thermoelasticity.

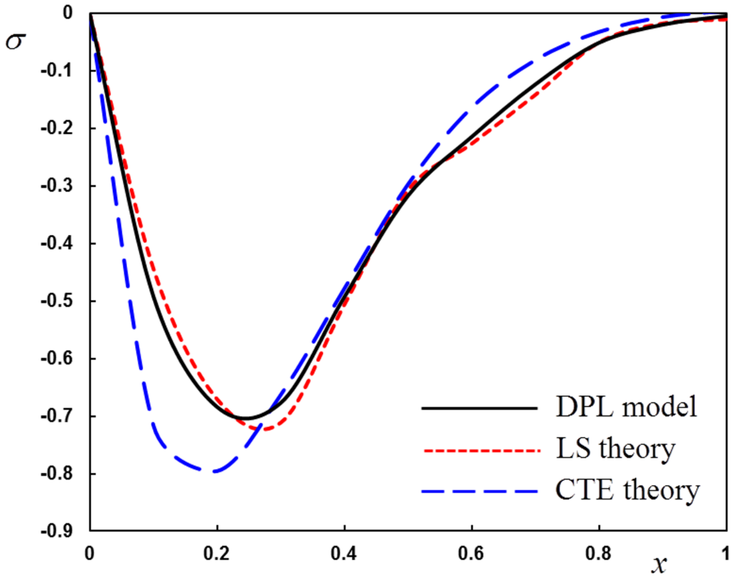

Figure 12: The thermal stress σ with distance x for different theories of thermoelasticity.

References

[1] Biot M.A.: *Thermoelasticity and irreversible thermodynamics.* J. Appl. Phys. **27**(1956), 3, 240–253.

[2] Lord H.W., Sulman Y.: *A generalized dynamical theory of thermoelasticity.* J. Mech. Phys. Solids **15**(1967), 5, 299–307.

[3] Green A.E., Lindasy K.A.: *Thermoelasticity.* J. Elast. **2**(1972), 1, 1–7.

[4] Tzou D.Y.: *A unified field theory for heat conduction from macro- to micro- scale.* ASME J. Heat Trans. **117**(1995), 1, 8–16.

[5] Chen P.J., Gurtin M.E.: *On a theory of heat conduction involving two temperatures.* Z. Angew. Math. Phys. **19**(1968), 4, 614–627.

[6] Chen P.J., Gurtin M.E., Williams W.O.: *On the thermodynamics of non-simple elastic materials with two temperatures.* Z. Angew. Math. Phys. **20**(1969), 1, 107–112.

[7] Chen P.J., Gurtin M.E., Williams W.O.: *A note on non simple heat conduction.* Z. Angew. Math. Phys. **19**(1968), 6, 960–970.

[8] Boley B.A., Tolins I.S.: *Transient coupled thermoelastic boundary value problems in the half space.* ASME J. Appl. Mech. **29**(1962), 4, 637–646.

[9] Warren W.E., Chen P.J.: *Wave propagation in the two temperature theory of thermoelasticity.* Acta Mech. **16**(1973), 1-2, 21–33.

[10] Youseff H.M.: *The dependence of the modulus of elasticity and the thermal conductivity on the reference temperature in generalized thermoelasticity for an infinite material with a spherical cavity.* J. Appl. Math. Mech. **26**(2005), 4, 470–475.

[11] Wood R.F., White C.W., Young R.T.: *Pulsed laser processing of semi- conductors.* In: Semiconductors and Semimetals, Vol. 23, Chapt. 5, Academic Press, London 1984.

[12] Trajkowski D., Cukic R.: *A coupled problem of thermoelastic vibrations of a circular plate with exact boundary conditions.* Mech. Res. Commun. **26**(1999), 2, 217–224.

[13] Wang X., Xu X.: *Thermoelastic wave induced by pulsed laser heating.* Appl. Phys. A, **73**(2001), 1, 107–114.

[14] McDonald F.A.: *On the precursor in laser-generated ultrasound waveforms in metals.* Appl. Phys. Lett. **56**(1990), 3, 230–232.

[15] Allam M.N.M., Aboulregal A.E.: *The thermoelastic waves induced by pulsed laser and varying heat of non-homogeneous microscale beam resonators.* J. Therm. Stresses **37**(2014), 4, 455–470.

[16] Othman M.I.A., Tantawi R.S., Eraki E.E.M.: *Effect of rotation on a semiconducting medium with two-temperature under L-S theory.* Arch. Thermodyn. **38**(2017), 2, 101–122.

[17] Abd-Alla A.N., Abo-Dahab S.M.: *On the reflection of the generalized magnetothermo-viscoelastic plane waves.* Chaos Soliton Fract. **16**(2003), 2, 211–231.

[18] Abd-Alla A.N., Abo-Dahab S.M.: *The influence of the viscosity and the magnetic field on reflection and transmission of waves at interface between magneto-viscoelastic materials.* Meccanica **43**(2008), 5, 437–448.

[19] Mukhopadhyay S.: *Effects of thermal relaxations on thermoviscoelasticity interactions in an unbounded body with a spherical cavity subjected to a periodic loading on the boundary.* J. Therm. Stresses **23**(2000), 7, 675-684.

[20] Mukhopadhyay B., Bera R.K.: *Effect of distributed instantaneous and continuous heat sources in an infinite conducting magneto-thermo-viscoelastic solid with thermal relaxation.* Comput. Math. Appl. **18**(1989), 8, 723–728.

[21] Ezat M.A., Othman M.I.A., El-Karamany A.S.: *State-space approach to two dimensional generalized thermoviscoelasticity with two relaxation times.* Int. J. Eng. Sci. **40**(2002), 11, 1251–1274.

[22] Othman M.I.A., Song Y.Q.: *Effect of rotation on plane waves of the generalized electromagneto-thermo-viscoelasticity with two relaxation times.* Appl. Math. Model. **32**(2008), 5, 811–825.

[23] Othman M.I.A., Fekry M.: *Effect of magnetic field on generalized thermo-viscoelastic diffusion medium with voids.* Int. J. Str. Stab. Dyn. **16**(2016), 7 1550033-1–1550033-21.

[24] Tzou D.Y.: *Macro- to microscale heat transfer: the lagging behavior.* Series in chemical and mechanical engineering, Taylor & Francis, Washington 1997.

[25] Sun Y., Fang D., Saka M., Soh A.K.: *Laser-induced vibrations of micro-beams under different boundary conditions.* Int. J. Solids Struct. **45**(2008), 7-8, 1993–2013.

[26] Honig G., Hirdes U.: *A method for the numerical inversion of the Laplace transform.* J. Comput. Appl. Math. **10**(1984), 1, 113–132.

archives
of thermodynamics
Vol. **38**(2017), No. 3, 101–118
DOI: 10.1515/aoter-2017-0018

Investigations on mixture preparation for two phase adiabatic pressure drop of R134a flowing in 5 mm diameter channel

TOMASZ MUSZYŃSKI[a*]
RAFAŁ ANDRZEJCZYK[a]
CARLOS A. DORAO[b]

[a] Gdańsk University of Technology, Narutowicza 11/12, 80-233 Gdańsk, Poland

[b] Norwegian University of Science and Technology, Department of Energy and Proces Engineering, N-7491 Trondheim, Norway

Abstract The article presents detailed two-phase adiabatic pressure drops data for refrigerant R134a. Study cases have been set for a mass flux varying from 200 to 400 kg/m^{2}s, at the saturation temperature of 19.4 °C. Obtained experimental data was compared with the available correlations from the literature for the frictional pressure drop during adiabatic flow. Influence of mixture preparation on pressure drop was investigated, for varying inlet subcooling temperature in the heated section. The flow patterns have also been obtained by means of a high-speed camera placed in the visualization section and compared with literature observations.

Keywords: Adiabatic flow; Frictional pressure drop; Two-phase flow; Flow pattern map; R134a

Nomenclature

A – surface area, m^2
a – heat transfer coefficient, W/m^{2}K
c_p – specific heat, J/kgK
D – diameter, m

---

[*] Corresponding Author. Email tommuszy@pg.gda.pl

f – friction factor
G – mass flux, kg/m^{2}s
g – gravitational acceleration, m/s^2
h – specific enthalpy, kJ/kg
L – channel length, m
I – current, A
MAD – mean absolute deviation, %
$\dot{m}$ – mass flow of refrigerant, kg/s
ΔP – pressure drop, Pa
$\dot{q}$ – heat flux, kW/m^2
$\dot{Q}$ – rate of heat, kW
T – temperature, °C
x – vapour quality

Greek symbols

α – heat transfer coefficient
ρ – density, kg/m^3

Superscripts

el – electric
i – inner
in – inlet
l – liquid
out – outlet
sat – saturation
sub – subcooling
v – vapour
W – wall

1 Introduction

Developers of many modern devices are faced with two conflicting trends: the need to dissipate increasing amounts of heat, and the quest for more compact and lightweight designs. These trends have spurred unprecedented increases in heat dissipation per volume and per surface area, forcing the research in heat removal enhancement in air cooling [1] and single-phase liquid cooling solutions [2]. Cooling demands in these and many other applications have resulted in a paradigm shift from single-phase to two-phase cooling strategies to capitalize upon the coolant's sensible and latent heat rather than sensible heat alone. Phase change cooling solutions come in a variety of configurations that could meet the system requirements of the application in question. These include pool boiling [3], channel flow boiling [4], mini/microchannels [5], jet [6,7], boiling on enhanced surfaces [8–10], and hybrid cooling techniques [11].

The flow of vapors and liquids in pipes, channels, equipment, etc. is frequently encountered in industry and has been studied intensively for many years. The reliable prediction of flow parameters in two-phase flows is thereby an important aim; yet, heat transfer coefficients and pressure gradients predicted using leading methods often differ by more than 50% according to various reports [12–14].

Instability of two-phase flow in a channel with evaporating fluid is closely related to the existence of pulsations of pressure and flow rate. Significant pressure pulsations may be dangerous. They can lead to channel wall deformations and, in consequence, emergency shutdown. Changes of mass flow rate accompanying pressure fluctuations may, on the other hand, lead to boiling crisis, which in effect lead to the reduction of heat transfer effectiveness in heat exchangers [15]. Therefore the issue of local stability (flow in the channel with evaporating fluids), as well as general evaporator stability, is important to the thermal design engineers [16].

Dorao *et. al* [17] studied the effect of the heating profile of the characteristics of pressure drop oscillations (PDO). The experiments were performed in a 2 m long horizontal test section with 5 mm internal diameter, with R134a as working fluid. The PDOs were characterized by superimposing high- and low-frequency oscillations for varying range of heat flux. It was observed that at low and high heat fluxes with a uniform heating profile the high-frequency oscillations vanish. In addition, a decreasing power distribution can increase their occurrence.

Two-phase flow maldistribution in systems of heated parallel channels with a subcooled inlet state was investigated by Oevelen *et.al* [18]. Such maldistribution can result from the nonmonotonic behavior of channel pressure drop as a function of flow rate. A pressure drop model applied to every individual channel was integrated together with a pump curve into a system model. Multiple different flow distributions can occur for a given operating condition; the stability of each flow distribution is assessed by solving a generalized eigenvalue problem. Parametric effects of inlet subcooling, heat flux, and flow rate on the stability of the uniform distribution and on the severity of maldistribution were also investigated. Authors observed that there is a minimum inlet subcooling below which the uniform distribution is always stable and maldistribution cannot occur, regardless of the boiling number.

Lee *et al.* [19] investigated the minimum mass flux conditions in which a stable flow is sustainable. Flow parameters were identified *via* 47 flow instability data points and were compared with relevant correlations. The results implied flow excursion points that were close to the onset of a significant void. The visualization of the flow excursion using a high-speed camera was achieved, clearly demonstrating that the flow excursion is triggered by the coalescence of facing bubbles or wavy vapors on opposing heated surfaces. Presented data showed deviation from predictions, therefore new empirical correlation that reflect the gap size effect was suggested.

As indicated in the literature experimental data tend to deviate greatly from predictions. Therefore, the main objective of this paper was to investigate the frictional pressure drop during adiabatic flow in the 5 mm diameter channel with varying heat flux at a two-phase mixture preparation section. The objective of the present study is to run the two-phase flow in-tube cases under different experimental conditions in order to characterize the frictional pressure drop for the refrigerant R134a, for vapor qualities ranging from 0 to 1.

2 Experimental setup

2.1 Experimental test facility

The experimental facility is the R134a loop consisting of a main reservoir or refrigerant, pump, preheater (conditioner), heated test section, sight glass, and an adiabatic section and condenser. The loop is schematically represented in Fig. 1.

The fluid pressure is set by controlling the temperature in the main tank where the refrigerant is at saturation conditions. The fluid is driven by a magnetically coupled gear pump which prevents any leakage of working fluid. The conditioner is a shell and tube heat exchanger with glycol in the shell side which is used for adjusting the R134a inlet temperature. Before entering the heated section the refrigerant flows through a Coriolis type mass flow meter. A mass flow rate accuracy of 0.2% of the reading was given by the supplier. The heated section is made from two meters long stainless steel tube. The section is electrically heated by Joule effect with the use of a low voltage AC power supply. The section is thermally insulated with a thick layer of mineral wool, thus thermal losses are neglected. The tube dimensions are 5 mm and 8 mm internal and external diameter respectively. Nine galvanically separated thermocouples are distributed along the wall surface, additional two are inside the tube in order to measure the local fluid temperature. The thermocouple accuracy after in house calibration

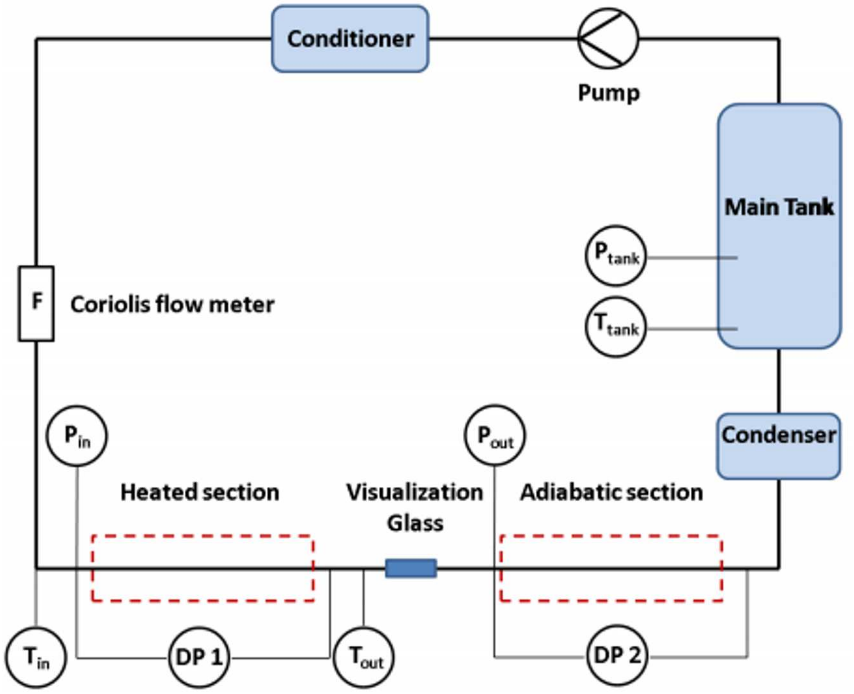

Figure 1: Schematic diagram of test facility: P_{tank} – pressure in the tank, P_{out} – pressure at the outlet of heated section, T_{out} – temperature at the outlet of the heated section, T_{in} – temperature at the inlet of the heated section, T_{tank} – temperature in the tank, DP1 – pressure drop at the heated section, DP2 – pressure drop at the adiabatic section.

was found to be 0.05 K.

The adiabatic test section is a 1 m long stainless steel pipe with an inner diameter of 5 mm and 8 mm outer diameter. It is thermally insulated with polyurethane foam insulation. The adiabatic and heated section are arranged horizontally in line, with a 300 mm distance between them.

2.2 Experimental procedure and data acquisition

The measurements have been performed with the aid of computer connected to a National Instruments Compact RIO data acquisition system. The signal from measuring devices was processed with the aid of the LabVIEW application. The temperatures, absolute pressures, pressure differences and mass flow rates were acquired at a frequency of 2 Hz.

For every experimental point ∼100 data points were acquired, thus every point was obtained by averaged values from ˜50 s measurements. Additionally, every experimental point was recorded twice, with 5 min interval, in order to exclude heat capacity effect of tube and insulation.

Two-phase total pressure drop was directly measured with a differential pressure transducer, same type differential pressure transducer was used to measure the adiabatic pressure drop. A differential pressure accuracy of 0.075% full-scale was given by the supplier. An absolute pressure accuracy of 0.04% full-scale was given by the supplier. This accuracy was checked by in house calibration. The heat flux and two-phase heat transfer coefficient were determined according to relations

$$\dot{q} = \frac{\dot{Q}_{el}}{A_W} \,, \tag{1}$$

$$\alpha = \frac{\dot{q}}{(T_W - T_{sat})} \,. \tag{2}$$

The absolute pressure at the inlet and outlet of the heated section was also recorded and was used for checking the saturation temperature T_{sat} of the fluid based on the equilibrium thermodynamic properties. The refrigerant quality at the inlet of the adiabatic section was determined from mass and energy conservation equations using NIST REFPROP fluid database [20]:

$$x_{out} = \frac{\dot{q}\pi D_i L - \dot{m} c_p \Delta T_{sub}}{\dot{m} h_{lv}} \,. \tag{3}$$

The general expression for describing the total two-phase pressure drop $\Delta \mathrm{p}_{total}$ is

$$\Delta p_{total} = \Delta p_{mom} + \Delta p_{frict} + \Delta p_{static} \,, \tag{4}$$

where Δp_{static} is the elevation head pressure drop and is neglected in a horizontal tube, Δp_{mom} is the momentum pressure drop created by the acceleration of the flow in a heating/cooling process, and Δp_{frict} is the two-phase frictional pressure drop.

The adiabatic two-phase pressure drops were obtained at the vapor quality leaving the horizontal boiling test section. No additional heat flux allows steady two-phase flow inside tube without bubble growth, thus the momentum pressure drop in the adiabatic section is zero. Therefore, we can determine the two-phase frictional pressure drops in the adiabatic test section directly from the measured values:

$$\Delta p_{total} = \Delta p_{frict} \,. \tag{5}$$

Using electric current to supply heat in the diabatic test section to evaporate the refrigerant, the wall temperature undergoes a slight temperature change while the phase changing refrigerant stays at nearly the same saturation temperature. The local heat flux is calculated as a function of generated Joule heat and is assumed to be constant during the evaporation process along the length of the tube.

In order to determine the reliability of the experimental results, an uncertainty analysis was conducted on all measured quantities as well as the quantities calculated from the measurement results. For the heat flux, the error coming from the propagation is the error associated with the voltage and current measurements. Nevertheless, the thermal heat flowing to the fluid under stationary conditions was calibrated against the electrical value for different temperatures and conditions for single phase liquid considering the heat exchange with the surroundings arriving to a final accuracy of 3%. Uncertainties were estimated according to the standard procedures described by National Institute of Standards and Technology (NIST) [20]. Overall, the uncertainty in the calculated vapor quality is lower than 10%.

3 Experimental data analysis

A summary of the experimental conditions of adiabatic two-phase pressure drop of R134a are presented in Tab. 1.

Table 1: Experimental conditions of pressure drop experiments.

Parameter	Unit	Operating range
D	m	0.005
L_h	m	2
L_{ad}	m	1
T_{sat}	°C	19.4
G	$\mathrm{kg/m^2s}$	200–400
q''	$\mathrm{W/m^2}$	100–69000

In order to verify the assumed accuracy of the measurement and the correctness of the experimental procedure the preliminary studies were accomplished involving the determination of the pressure drop for the single-phase adiabatic flow of the test fluid R134a. The obtained experimental data, in the form of a pressure drop at the length of the 2 m long channel were compared with the Darcy-Weisbach correlation, assuming the friction coefficient according to the Haaland [21] equation, with pipe roughness height given by supplier to be below 0.03 mm. The pressure drop can be obtained by the following expression:

$$\Delta p = f\frac{G^2}{2\rho}\frac{L}{D}\,, \tag{6}$$

where f is the frction factor It turns out that the majority of the experimental data fits in the range of ±10% of the consistency with predictions. The maximal absolute deviation of 30% was present in the lower range of Reynolds numbers, as can be seen in Fig. 2. This can be attributed to larger error of pressure transducers. Most of the experimental points presented in this article are higher than 2 kPa.

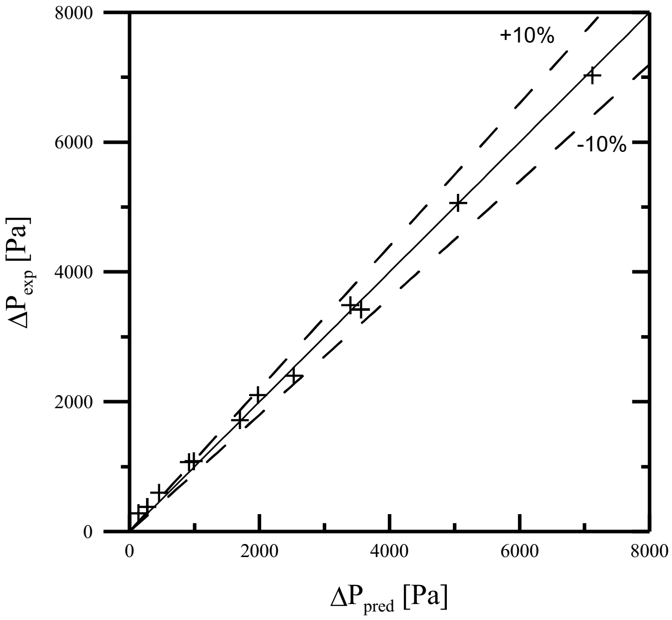

Figure 2: Comparison of single-phase pressure drop experimental data for the R134a with the predicted Darcy-Weisbach correlation.

In authors opinion that result can be deemed as satisfactory, particularly in the light of the fact that the recorded pressure drop rarely drops below a value of 1 kPa, with a maximum of 50 kPa in the accomplished experiment. The deviation between predicted and obtained results are close to the measurement accuracy achieved by the applied pressure transducers.

Adiabatic pressure drop

Adiabatic pressure drops as indicated in the introduction can be measured after preparation of vapour-liquid mixture in heated section. Varying the inlet subcooling temperature of working fluid will influence the amount of heat necessary to obtain same vapor quality. Figure 3 shows the experimental two-phase pressure drop of the 5 mm tube as a function of mass flux and heat flux of R134a at different subcooling temperatures, at a saturation temperature of 19.4 °C.

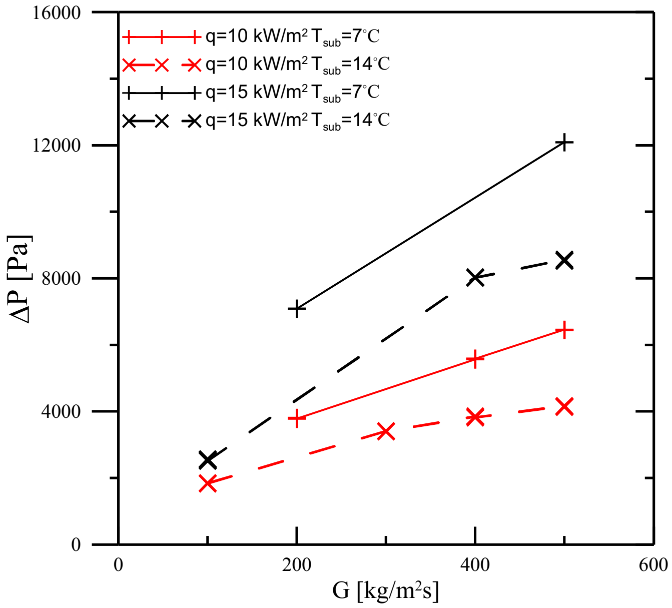

Figure 3: Experimental two-phase pressure drop in the 5 mm tube as a function of mass flux and heat flux of R134a at different subcooling temperatures.

The experimentally obtained adiabatic pressure drop values are compared with well-known correlations from the literature. Because inlet vapor quality is obtained from energy balance equation on heated section all data regarding adiabatic flow with the same mass flux and various subcooling are plotted on a single figure. The pressure drop gradients are calculated by dividing measured pressure difference by the test section length, thus each experiment test condition allows to gather a single point. Since the flow is adiabatic the experimental data presents a frictional pressure drop. Figures 4 to 6 show the experimental adiabatic frictional pressure drops, plotted versus values predicted with selected correlations. Pressure drop models used in this comparison are presented in detail in the previous section.

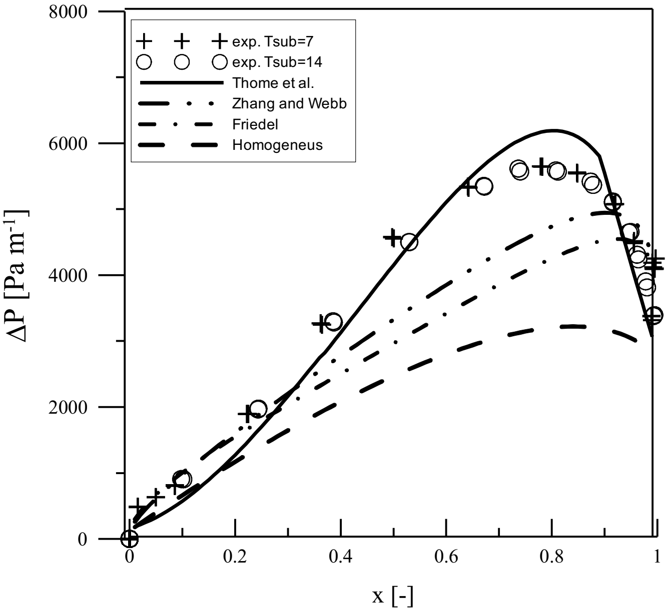

Figure 4: Experimental adiabatic pressure drop of R134a as a function of vapor quality in comparison with literature models for $G = 200$ kg/m^{2}s.

The adiabatic pressure drop along channel increases exponentially with mass flux. It can also be seen that the two-phase pressure drop is increasing for higher exit vapor quality with a maximum about vapor qualities around x = 0.7-0.9, as reported in the literature. The local maxima of pressure drop are observed to be more shifted towards higher vapor qualities at a higher mass fluxes. It can be seen that pressure drop values of each mass flux corresponds to single phase pressure drop values. It can also be seen from that the difference between the two phase pressure drops is higher for higher mass flux. That corresponds to the trends reported in literature, e.g., by Ould Didi *et al.* [22] for refrigerants flow in macrotubes of 10.92–12 mm and by Tran *et al.* [23], for small channels.

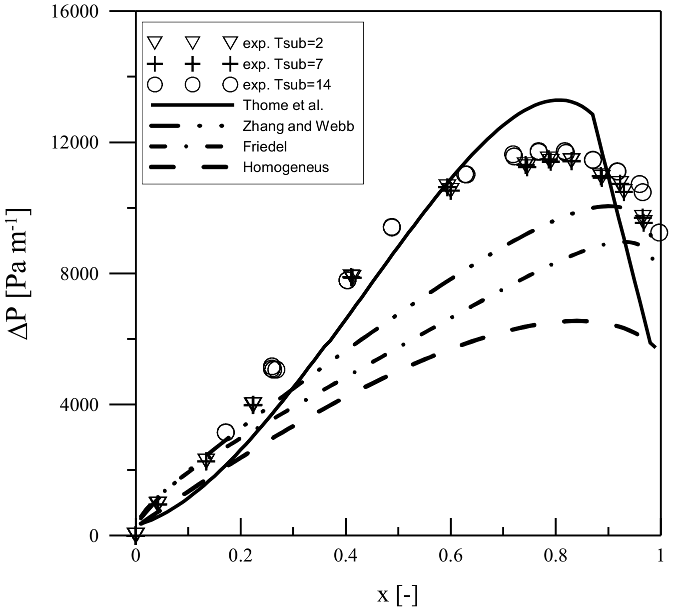

Figure 5: Experimental adiabatic pressure drop of R134a as a function of vapor quality in comparison with literature models for $G = 300$ kg/m^{2}s.

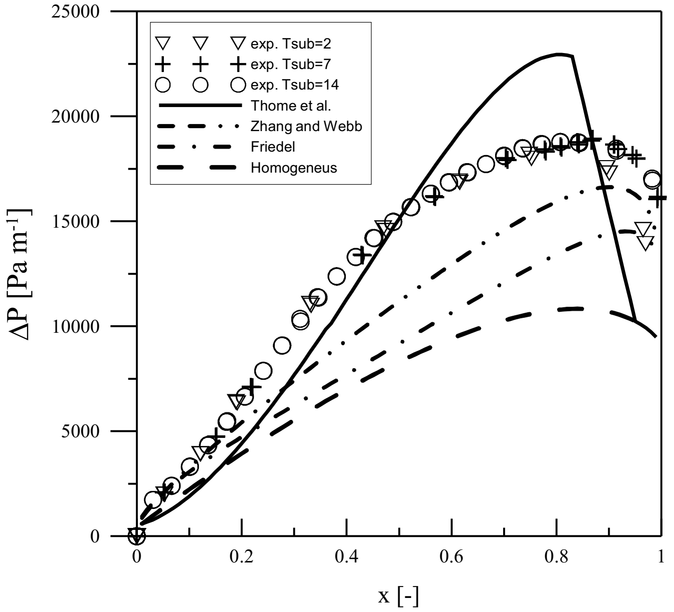

Figure 6: Experimental adiabatic pressure drop of R134a as a function of vapor quality in comparison with literature models for $G = 400$ kg/m^{2}s.

From an overall comparison of figures, 4 to 6 good agreement with experimental data for correlations of Zhang and Webb [24] and Thome *et al.* [25] clearly stands out as best in describing pressure drop variations with varying vapor quality. Most importantly one can observe the difference between the experimental data series for varying inlet subcooling. For higher values of inlet subcooling series experimental pressure drop is shifted towards higher values, what is visible for 0.8–1 vapor qualities.

Table 2: Literature correlations predictions confidence levels.

	Zhang and Webb	Thome *et al.*	Friedel	Homogeneous
Mean abolute deviation	0.17	0.18	0.24	0.36
Confidence level > 30%	0.93	0.80	0.58	0.27
> 20%	0.60	0.63	0.36	0.09
> 10%	0.30	0.32	0.22	0.04

The Zhang and Webb [24] correlation is a modified form of the Friedel [26] correlation. This correlation predicts most of the data within ±30%. However, only 30% of the data is predicted within 10% error band.

The correlation of Thome et al. [25] for predicting the frictional pressure drop is flow pattern based. Thus this method includes the effect of interfacial flow structure via the flow pattern map, and better follows the variation in pressure gradient with vapor quality. Also, it captures the peak in the pressure gradient at high vapor qualities. It is based on the actual mean velocities of the phases via the void fraction equation rather than superficial velocities. It has to be pointed that pressure drop experimental values during the experiments were also visually investigated in order to validate flow pattern map developed by Wojtan *et al.* [27].

Predictions given by the homogeneous model assume equal velocities of vapor and liquid, also the fluid is considered as one single phase with averaged properties. This model under predicts the data with a mean aqbsolute deviation (MAD) of 36%. It should be noted that the prediction trend in the results is good and that the deviation is decreasing with increased mass flux, indicating that with a change in the leading constant this correlation would give better predictions. In low flow ranges, prediction error seems to be more pronounced in vapor qualities in a range of $x = 0.4$–0.8.

In order to find an answer for a shift in pressure drop values, flow visualization was performed. Figure 7 shows the flow pattern map for a representative set of experimental conditions for the mass flux $G = 400$ kg/m^{2}s. Selected points confirming structure shown on the flow pattern map are depicted in Figs. 8 to 12. This map is based on a recent version of the Kattan *et al.* [28] flow map, proposed by Wojtan *et al.* [27], and also includes an improved method for the effect of heat flux on the transition to mist flow. D represents the transition zone between annular and mist flow.

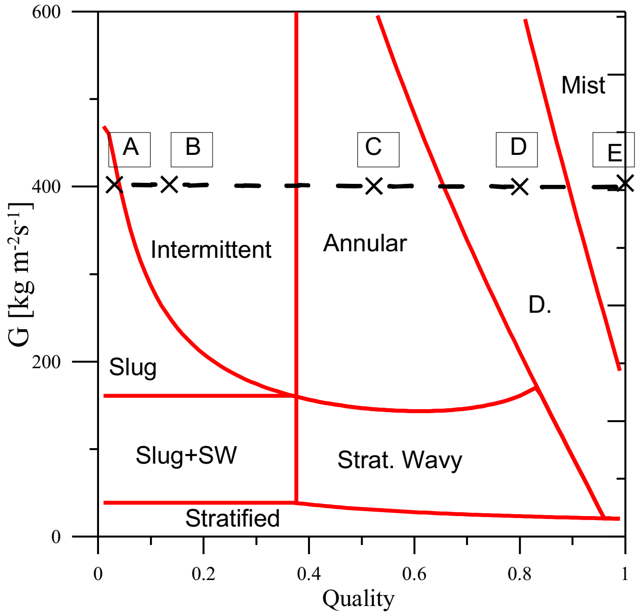

Figure 7: Flow pattern map evaluated for R134a at $T_{sat} = 19.4$ °C in a 5 mm internal diameter tube for $\dot{q} = 35$ kW/m^2 using $G = 400$ kg/m^{2}s to calculate the void fractions.

All of the obtained visualizations were similar in terms of flow structure without a visible difference in the flow pattern. As mentioned in the previous section, the refrigerant was heated in horizontal channel of approx. 2 m length. Vapor quality at the inlet of the adiabatic test section was calculated from energy balance equation. Entrained droplets can be observed in Fig. 12, while the calculated vapor quality is equal to 1 (Fig. 7). In authors' opinion the difference between presented test runs may be explained by the

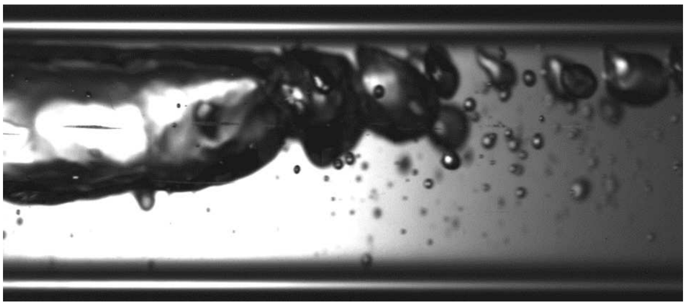

Figure 8: Experimentally obtained slug adiabatic flow of R134a for $G = 400$ kg/m^{2}s with $\dot{q} = 4.7$ kW/m^2, point A on flow pattern map.

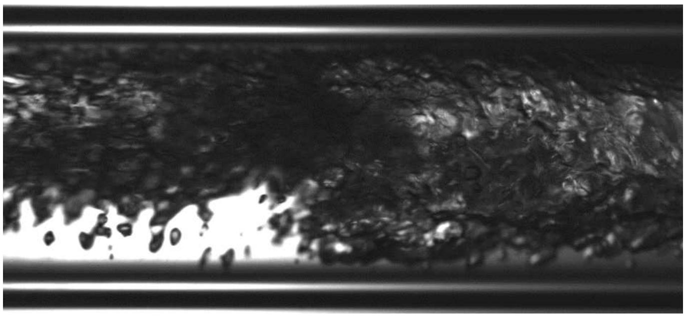

Figure 9: Experimentally obtained intermittent adiabatic flow of R134a for $G = 400$ kg/m^{2}s with $\dot{q} = 9.5$ kW/m^2, point B on flow pattern map.

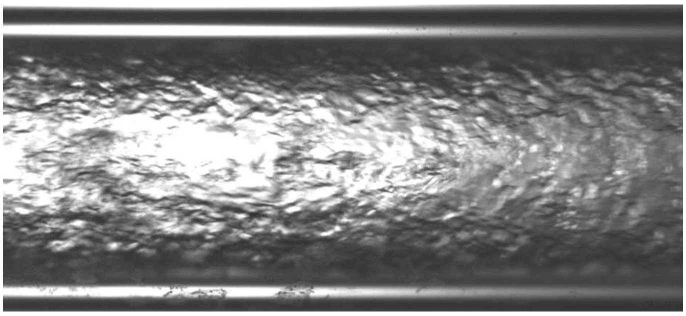

Figure 10: Experimentally obtained annular adiabatic flow of R134a for $G = 400$ kg/m^{2}s with $\dot{q} = 28.6$ kW/m^2, point C on flow pattern map.

entrainment effect, which is influenced by the supplied heat flux. Unfortunately, in most prediction tools the parameters at which the two-phase mixture is prepared are not taken into account. It is also possible that the

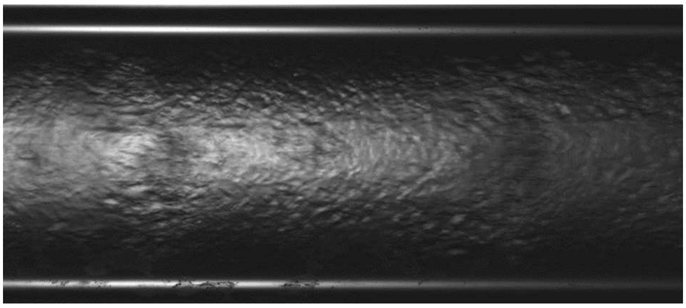

Figure 11: Experimentally obtained dryout adiabatic flow of R134a for $G = 400$ kg/m^{2}s with $\dot{q} = 39$ kW/m^2, point D on flow pattern map.

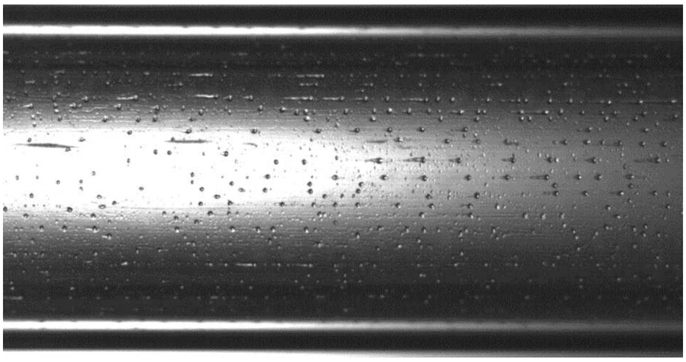

Figure 12: Experimentally obtained mist adiabatic flow of R134a for $G = 400$ kg/m^{2}s with $\dot{q} = 47$ kW/m^2, point E on flow pattern map.

pressure drop is affected by an average void fraction which may be different than in a single snapshot.

4 Conclusions

As the first step of this work, a comprehensive experimental study was undertaken in order to obtain accurate two-phase pressure drop values during the adiabatic flow of refrigerants R134a in a horizontal tube. The flow conditions were chosen to obtain experimental values over a wide range of test parameters so that the effect of each parameter could be easily identified. The range of experimental conditions covered were three mass velocities and vapor quality covering the entire range from 1 to 0, and three inlet subcooling temperatures. The existing experimental facility allowed to run tests under adiabatic conditions to obtain two-phase pressure drop values for nearly every flow regime, and to validate the data reduction procedure used to obtain the pressure drop, and to validate existing flow pattern maps. The experimental campaign acquired over 500 experimental two-phase pressure drop values covering all flow regimes except bubbly because of operating limitations.

Obtained data is used as a validation of the literature models, a set of graphs showed comparisons, for a representative set of experimental conditions, of the two-phase frictional pressure gradients for the adiabatic test section. Agreement including reliability of the measurements as well as the correctness of the data reduction protocol and choice of void fraction model was shown to be quite good. A slight shift from predictions given by Thome *et al.* [25] model was attributed to entrained droplets in vapor flow with fluid enthalpy calculated from energy balance higher than saturated vapor.

Verification of the pressure drop for single-phase adiabatic flow showed that for Zhang and Webb correlation 93% of experimental data fits in the range of +/-30%. The model proposed by Thome *et al.* in other hand predicts almost 33% of data within 10% error, but only 80% of the data is predicted within 30% error.

Acknowledgements The authors would like to appreciate funding received from the Research Council of Norway under the FRINATEK Project 231529.

Received 21 January 2017

References

[1] Muszynski T., Koziel S.M.: *Parametric study of fluid flow and heat transfer over louvered fins of air heat pump evaporator.* Arch. Thermodyn. **37**(2016), 3, 45–62. DOI:10.1515/aoter-2016-0019.

[2] Bohdal T., Charun H., Sikora M.: *Empirical study of heterogeneous refrigerant condensation in pipe minichannels.* Int. J. Refrig. **59**(2015), 210–223. DOI:10.1016/j.ijrefrig.2015.07.002.

[3] Mudawar I., Howard A.H., Gersey C.O.: *An analytical model for near-saturated pool boiling critical heat flux on vertical surfaces.* Int. J. Heat Mass Transf. **40**(1997), 2327–2339.

[4] Mikielewicz D., Andrzejczyk R., Jakubowska B., Mikielewicz J.: *Analytical model with nonadiabatic effects for pressure drop and heat transfer during boiling and*

condensation flows in conventional channels and minichannels. Heat Transf. Eng. **37**(2016), 1158–1171.

[5] Tran T.N., Wambsganss M.W., France D.M.: *Small circular-and rectangular-channel boiling with two refrigerants.* Int. J. Multiph. Flow. **22**(1996), 485–498.

[6] Muszynski T., Mikielewicz D.: *Comparison of heat transfer characteristics in surface cooling with boiling microjets of water, ethanol and HFE7100.* Appl. Therm. Eng. **93**(2016), 1403–1409. DOI:10.1016/j.applthermaleng.2015.08.107.

[7] Muszynski T., Andrzejczyk R.: *Applicability of arrays of microjet heat transfer correlations to design compact heat exchangers.* Appl. Therm. Eng. **100**(2016), 105–113, DOI:10.1016/j.applthermaleng.2016.01.120.

[8] Nakayama W., Nakajima T., Hirasawa S.: *Heat sink studs having enhanced boiling surfaces for cooling of microelectronic components.* ASME Pap. 84-WA/HT-89(1984).

[9] Marto P.J., Lepere V.J.: *Pool boiling heat transfer from enhanced surfaces to dielectric fluids.* J. Heat Transfer. **104**(1982), 292–299.

[10] Andrzejczyk R., Muszynski T.: *Performance analyses of helical coil heat exchangers. The effect of external coil surface modification on heat exchanger effectiveness.* Arch. Thermodyn. **37**(2016), 4, 137–159. DOI:AOT-00010-2016-04.

[11] Muszynski T., Andrzejczyk R.: *Heat transfer characteristics of hybrid microjet – microchannel cooling module.* Appl. Therm. Eng. **93**(2016), 1360–1366. DOI:10.1016/j.applthermaleng.2015.08.085.

[12] Andrzejczyk R., Muszynski T., Alberto Dorao C.: *Experimental investigations on adiabatic frictional pressure drops of R134a during flow in 5mm diameter channel.* Exp. Therm. Fluid Sci. **83**(2017), 78–87. DOI:10.1016/j.expthermflusci.2016.12.016.

[13] Mikielewicz D., Jakubowska B.: *Prediction of flow boiling heat transfer coefficient for carbon dioxide in minichannels and conventional channels.* Arch. Thermodyn. **37**(2016), 2, 89–106. DOI:10.1515/aoter-2016-0014.

[14] Mikielewicz D., Andrzejczyk R.: *Comparative study of flow condensation in conventional and small diameter tubes.* Arch. Thermodyn. bf 33(2012), 2, 67–83. DOI:10.2478/v10173-012-0011-2.

[15] Mikielewicz J., Mikielewicz D.: *Thermal-hydraulic issues of flow boiling and condensation in organic Rankine cycle heat exchangers.* Arch. Thermodyn. **33**(2012), 1, 41–66. DOI:10.2478/v10173-012-0002-3.

[16] Muszynski T.: *Design and experimental investigations of a cylindrical microjet heat exchanger for waste heat recovery systems.* Appl. Therm. Eng. **115**(2017),782–792. DOI:10.1016/j.applthermaleng.2017.01.021.

[17] Dorao C.A., Langeland T., Fernandino M.: *Effect of heating profile on the characteristics of pressure drop oscillations.* Chem. Eng. Sci. **158**(2017), 453–461. DOI:10.1016/j.ces.2016.10.009.

[18] Van Oevelen T., Weibel J.A., Garimella S.V.: *Predicting two-phase flow distribution and stability in systems with many parallel heated channels.* Int. J. Heat Mass Tran. **107**(2017), 557–571. DOI:10.1016/j.ijheatmasstransfer.2016.11.050.

[19] Lee J., Chae H., Chang S.H.: *Flow instability during subcooled boiling for a downward flow at low pressure in a vertical narrow rectangular channel.* Int. J. Heat Mass Tran. **67**(2013), 1170–1180. DOI:10.1016/j.ijheatmasstransfer.2013.08.049.

[20] *N. REFPROP, standard reference database 23. NIST Thermodyn. Prop. Refrig. Mix. Database (REFPROP).* Version. 9 (2002).

[21] Haaland S.E.: *Simple and explicit formulas for the friction factor in turbulent pipe flow.* J. Fluids Eng. **105**(1983), 1, 89–90.

[22] Ould Didi M.B., Kattan N., Thome J.R.: *Prediction of two-phase pressure gradients of refrigerants in horizontal tubes.* Int. J. Refrig. **25**(2002), 935–947. DOI:10.1016/S0140-7007(01)00099-8.

[23] Tran T.N., Chyu M.-C., Wambsganss M.W., France D.M.: *Two-phase pressure drop of refrigerants during flow boiling in small channels: An experimental investigation and correlation development.* Int. J. Multiph. Flow. **26**(2000), 11, 1739–1754.

[24] Zhang M., Webb R.L.: *Correlation of two-phase friction for refrigerants in small-diameter tubes.* Exp. Therm. Fluid Sci. **25**(2001), 3–4, 131–139. DOI:10.1016/S0894-1777(01)00066-8.

[25] Thome J.R.: *Engineering Databook III.* Wolverine Tube Inc. 2010 (2004).

[26] Friedel L.: *Improved friction pressure drop correlations for horizontal and vertical two-phase pipe flow.* In: Eur. Two-Phase Flow Gr. Meet. Pap. E, 1979.

[27] Wojtan L., Ursenbacher T., Thome J.R.: *Investigation of flow boiling in horizontal tubes: Part II—Development of a new heat transfer model for stratified-wavy, dryout and mist flow regimes.* Int. J. Heat Mass Tran. **48**(2005), 2970–2985.

[28] Kattan N., Thome J.R., Favrat D.: *Flow boiling in horizontal tubes: Part 1 – Development of a diabatic two-phase flow pattern map.* J. Heat Transfer. **120**(1998), 1, 140–147.

archives
of thermodynamics
Vol. **38**(2017), No. 3, 119–134
DOI: 10.1515/aoter-2017-0019

Analysis of heat flow in a tube bank of a condenser considering the influence of air

MAGDA JOACHIMIAK*
DAMIAN JOACHIMIAK
PIOTR KRZYŚLAK

Poznan University of Technology, Chair of Thermal Engineering, Piotrowo 3, 60-965 Poznań, Poland

Abstract The pressure of wet water vapor inside a condenser has a great impact on the efficiency of thermal cycle. The value of this pressure depends on the mass share of inert gases (air). The knowledge of the spots where the air accumulates allows its effective extraction from the condenser, thus improving the conditions of condensation. The condensation of water vapor with the share of inert gas in a model tube bank of a condenser has been analyzed in this paper. The models include a static pressure loss of the water vapor/air mixture and the resultant changes in the water vapor parameters. The mass share of air in water vapor was calculated using the Dalton's law. The model includes changes of flow and thermodynamic parameters based on the partial pressure of water vapor utilizing programmed water vapor tables. In the description of the conditions of condensation the Nusselts theory was applied. The model allows for a deterioration of the heat flow conditions resulting from the presence of air. The paper contains calculations of the water vapor flow with the initial mass share of air in the range 0.2 to 1%. The results of calculations clearly show a great impact of the share of air on the flow conditions and the deterioration of the conditions of condensation. The data obtained through the model for a given air/water vapor mixture velocity upstream of the tube bank allow for identification of the spots where the air accumulates.

Keywords: Condensation; Inert gas; Mass share of gas noncondensing in water vapor; Dalton's law; Water vapor and air partial pressure

---

*Corresponding Author. Email: magda.joachimiak@put.poznan.pl

Nomenclature

A – surface area, m^2
c – velocity, m/s
D – tube external diameter, m
g – gravitational acceleration, m/s^2
h – enthalpy, J/kg
k – air mass share, %
l – pipe length, m
M – mole mass, kg/kmol
$\dot{m}$ – mass flow rate, kg/s
Nu – Nusselt number
n – number of tube rows
p – pressure, Pa
Q – heat flow, W
r – heat of evaporation, J/kg
R – individual gas constant, J/KgK
Re – Reynolds number
S – width of the tube bank, m
T – temperature, K
W_i – Chebyshev polynomial of the first kind of the ith degree
X – vetical and horizontal distance between the centers of the tubes, m

Greek symbols

α – heat transfer coefficient, W/m^{2}K
Δ – difference
ε – function describing the relation of heat transfer coefficients for condensation of water vapor with air and with pure water vapor
λ – heat conductance coefficient, W/mK
μ – dynamic viscosity, kg/m s
ν – kinematic viscosity, m^2/s
ρ – density, kg/m^3
ξ – total coefficient of pressure loss

Superscripts

0 – upstream of the first row of tubes
a – air
c – condensed
f – flow
l – condensate
m – mixture of gases
s – saturation
p – tubes in one bank row
sum – total for all rows of tubes
v – water vapor
w – wall

1 Introduction

The efficiency of thermal cycle depends, among others things, on the vacuum level inside the condenser. Due to the leakage of the condenser, air (inert gas) penetrates into the system. One of the factors influencing pressure and the resulting temperature of water vapor saturation is the mass share of inert gases [4,6,8]. The presence of air results in a decrease of the partial pressure of water vapor near the condensate film, which causes a local drop of saturation temperature, decreases the difference of temperatures between the water vapor and the wall and deteriorates the conditions of heat flow [5,6,8,10] (Fig. 1).

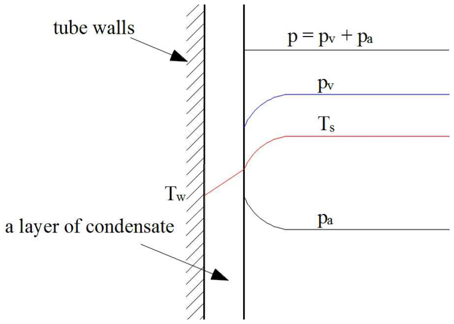

Figure 1: Distribution of pressure and temperature during condensation of water vapor in a solution with air [10].

The accumulating air causes additional thermal resistance and necessitates a greater number of tube rows for the water vapor mass flow to condense. In [3] heat flow and the phenomenon of subcooling was analyzed for condensation inside the horizontal tube. The influence of the share of air, gas velocity and pressure on the heat transfer coefficient was investigated. The influence of the mass flow of gas, mass share of inert gas and pressure during condensation inside the horizontal tube on the heat flow was described in [1]. Experimental research indicates that an increase in the mass share of air to 4% results in a drop of the heat transfer coefficient, α, of up to 20% referred to the same coefficient for pure water vapor [2]. Problems related to the mathematical modeling of condensers have been described in [8]. In this work a mathematical model was analyzed that leads to a solution in the form of fields of velocity, pressure and inert gases for two types of condensers. The analysis of the changes of thermodynamic parameters during water vapor condensation with the participation of air is an important issue in terms of water vapor cycle efficiency. In this paper the authors analyze the influence of the mass share of air in water vapor on the thermal and flow parameters in the model tube bank of a condenser.

2 Calculation model

The model tube bank is composed of tubes set in a rectangular order with identical vertical and horizontal distance (Fig. 2). The calculations were made for $l = 1$ m of the tube length and the width of the tube bank S. Hence, the flow surface area upstream of the bank is

$$A_0 = Sl \; . \tag{1}$$

The flow surface area of the gas among the tubes can be described with the formula

$$A_f = \frac{S\,(X - D)\,l}{X} \; . \tag{2}$$

The lateral area of the tubes in one row is

$$A_p = \frac{S}{X}\pi Dl \; . \tag{3}$$

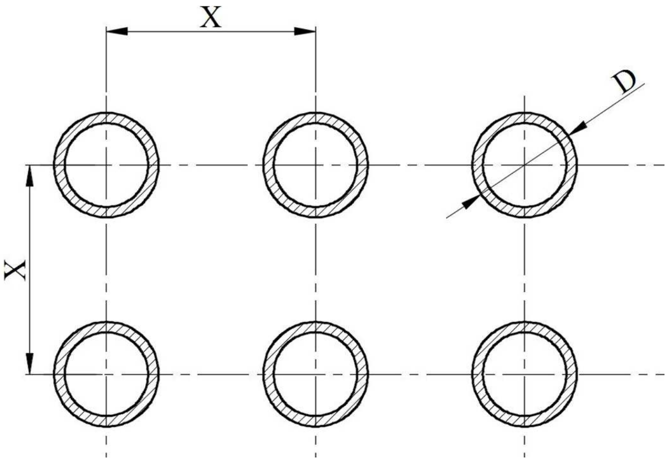

Figure 2: Distribution of the tubes in the tube bank.

The following values have been assumed upstream of the first row of tubes: gas mixture pressure, velocity of gases and mass share of air and temperature of the tube walls. In the calculations, water vapor tables have been used based on [9,11]. Based on the partial pressure of water vapor in an ith row of tubes, for the saturation parameters, saturation temperature, T_{vi}, specific enthalpy, h_{1i}, specific volume, v_{vi}, heat of evaporation, r_i, and kinematic viscosity, ν_{vi}, were calculated. For the given partial pressure of water vapor from the saturation line $x = 0$ specific volume v_{li} and kinematic viscosity, μ_{li}, of the condensate were obtained. In the model, the authors assumed that the temperature of the mixture equals that of the water vapor saturation

$$T_{mi} = T_{vi} \ . \tag{4}$$

If the calculated value of the temperature of water vapor saturation in an ith row of tubes is lower or equal to the temperature of the tube walls it will result in stopping of the calculations. The mass flow of the gases in an ith row of tubes was determined as a difference of the mass flow of gases in the previous row less the condensed mass flow of water vapor

$$\dot{m}_i = \dot{m}_{i-1} - \Delta\dot{m}_{i-1} \ . \tag{5}$$

For the first row of tubes the mass flow rate was determined with the formula

$$\dot{m}_1 = \rho_{m1} c_1 A \tag{6}$$

and for the last row

$$\dot{m}_m = k_{a1}\dot{m}_1 \ . \tag{7}$$

The share of air in the ith row of tubes is

$$k_{ai} = \frac{k_{a1}\dot{m}_1}{\dot{m}_i} \ . \tag{8}$$

For the first row of tubes the share of air k_{a1} is a preset value while for the last row $k_{am} = 1$ (for rows in which the entire mass flow rate of steam is condensed). Hence, the mass airflow in the ith row of tubes is

$$\dot{m}_{ai} = k_{ai}\dot{m}_i \ . \tag{9}$$

The gas constant of the mixture of gases depends on gas constants of air and water vapor as well as the mass share of air in the water vapor

$$R_{mi} = R_a k_{ai} + R_v \left(1 - k_{ai}\right) \ , \tag{10}$$

where $R_a = 278.05 \ \frac{\text{J}}{\text{kgK}}$ while $R_v = 461.91 \ \frac{\text{J}}{\text{kgK}}$. The pressure of the mixture of gases in the ith row of tubes was determined based on the difference between the pressure of gases upstream of the ith row of tubes and the drop of pressure in this row

$$p_{mi} = p_{m,i-1} - \Delta p_{m,i-1} \; . \tag{11}$$

For the first row of tubes the mixture pressure, p_{m1}, is a preset value. The partial pressure of air was determined based on the Clapeyron equation

$$p_{ai} = \frac{k_{ai} p_{mi} R_a}{R_v + k_{ai}\left(R_a - R_v\right)} = \frac{k_{ai} p_{mi} R_a}{R_{mi}} \; . \tag{12}$$

Based on the Dalton's law, the partial pressure of water vapor was calculated

$$p_{vi} = p_{mi} - p_{ai} \; . \tag{13}$$

The density of air is

$$\rho_{ai} = \frac{p_{ai}}{R_a T_{mi}} \; . \tag{14}$$

From the Dalton's law and the Clapeyron equation, the density of mixture of gases was determined

$$\rho_{mi} = \frac{R_a \rho_{ai} + R_v \rho_{vi}}{R_{mi}} \; . \tag{15}$$

The dynamic viscosity was determined based on the steam tables, and the air viscosity was based on the air density (14) as well as the relation describing kinematic viscosity of air. The air viscosity is described by the function depending on temperature of the gas mixture

$$\nu_{ai} = 0.0016583 e^{-0.053\left[T_m(i-1) - 273.15\right]} \; . \tag{16}$$

The dynamic viscosity has been described with the Wilkie method [10]

$$\mu_{mi} = \frac{z_{vi}\mu_{vi}}{z_{vi}\Phi_{vvi} + z_{ai}\Phi_{vai}} + \frac{z_{ai}\mu_{ai}}{z_{vi}\Phi_{avi} + z_{ai}\Phi_{aai}} \; , \tag{17}$$

where

$$\Phi_{vvi} = \Phi_{aai} = 1 \; , \tag{18}$$

$$\Phi_{vai} = \frac{1}{\sqrt{8}}\left(1 + \frac{M_v}{M_a}\right)^{-0.5}\left[1 + \left(\frac{\mu_{vi}}{\mu_{ai}}\right)^{0.5}\left(\frac{M_a}{M_v}\right)^{0.25}\right]^2 \; , \tag{19}$$

$$\Phi_{avi} = \frac{1}{\sqrt{8}}\left(1 + \frac{M_a}{M_v}\right)^{-0.5}\left[1 + \left(\frac{\mu_{ai}}{\mu_{vi}}\right)^{0.5}\left(\frac{M_v}{M_a}\right)^{0.25}\right]^2 \; , \tag{20}$$

$$z_{vi}=\frac{p_{vi}}{p_{mi}},\quad z_{ai}=\frac{p_{ai}}{p_{mi}}\ . \tag{21}$$

Viscosity of the mixture is determined by the relation [10]

$$\nu_{mi}=\frac{\mu_{mi}}{\rho_{mi}}\ . \tag{22}$$

Based on the flow continuity equation, the velocities of gases among the tubes can be expressed as

$$c_i=\frac{\dot{m}_i}{\rho_{mi}A_f}\ . \tag{23}$$

The total coefficient of pressure loss in the ith row of tubes was described with the relation [2]

$$\xi_{sum,i}=(6+9i)\left(\frac{X}{D}\right)^{-0.13}\mathrm{Re}_i^{-0.26}\ , \tag{24}$$

where $\mathrm{Re}_i=\frac{Dc_i}{\nu_{mi}}$. The loss of pressure is

$$\Delta p_{mi}=(\xi_i-\xi_{i-1})\,\frac{\rho_{mi}c_i^2}{2}\ , \tag{25}$$

where $\xi_0=0$. The Nusselt number was described with the aid of formula [10]

$$\mathrm{Nu}_i=0.728\left(\frac{\rho_l g r_i D^3}{\mu_l\lambda_l\,(T_{mi}-T_w)}\right)^{0.25}\ . \tag{26}$$

The ratio of coefficients of heat transfer for the condensation of water vapor with air and pure water vapor has been shown in Fig. 3 and described with the formula [2]

$$\varepsilon=\frac{\alpha_{va}}{\alpha_v}\ . \tag{27}$$

The dependence of ε on the share of air for $k_a\in[0,0.07]$ was described with the 10th degree polynomial based on experimental data described in [2]

$$\varepsilon=\sum_{j=0}^{10}a_jW_j\left(\varsigma_i\right)\ , \tag{28}$$

where W_j is a Chebyshev polynomial j [7], and the interval $k_a\in[0,0.07]$ was transformed to interval $\varsigma\in[-1,1]$. The values of the coefficients of

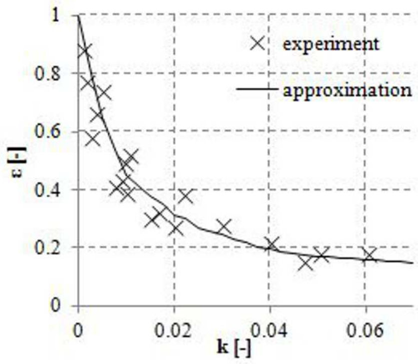

Figure 3: The dependence of ε on the share of air [2].

Table 1: Polynomial coefficients.

a_0	0.354370	a_4	0.04383900	a_8	-0.0019692
a_1	-0.319400	a_5	-0.02284100	a_9	0.0025022
a_2	0.172280	a_6	0.00787620	a_{10}	-0.0016688
a_3	-0.085118	a_7	-0.00029291		

the polynomial have been listed in Tab. 1. For the share of air above 0.07, a linear function was determined crossing the points (0.07,0.15) and (1,0). Based on the definition of Nusselt number and the value ε, the coefficient α was calculated allowing for determination of the share of air during condensation [2]

$$\alpha_{vai} = \varepsilon_i \frac{Nu_i \lambda_l}{D} \ . \tag{29}$$

The heat flow from the water vapor condensing to water inside is described by the formula

$$Q_i = A_p \alpha_{vai} \left(T_{mi} - T_w \right) \ . \tag{30}$$

For the last row of tubes the heat flow was calculated based on the relation

$$Q_m = r_{m-1} \left(\dot{m}_{m-1} - \dot{m}_m \right) \ . \tag{31}$$

The flow of the condensed mass of water vapor is

$$\Delta \dot{m}_i = \frac{Q_i}{r_i} \ . \tag{32}$$

3 Results of calculations

The calculations were made with the assumption that the tube bank receives a mixture of water vapor and air of the pressure of 7000 Pa with the velocity of 17 m/s. Taking the change of the flow area in the tube bank into account, the velocity between the tubes in the first row was 34 m/s. Besides, it was assumed that there is air in the water vapor of the mass shares of: 0.002, 0.004, 0.006, 0.008, and 0.01. The tube bank is composed of tubes set in a rectangular fashion of identical horizontal and vertical distances. The dimensions have been given in Tab. 2. The length of the tube bank results from the number of rows of tubes where the water vapor condenses.

Table 2: Geometry of the tube bank and input data for the calculations.

D, m	0.028
X, m	0.056
S, m	1.008
p_{m0}, Pa	7000
c_0, m/s	17
T_w, K	283
k, –	0.002, 0.004, 0.006, 0.008, 0.01

The model allowed calculating the static pressure in the subsequent rows of tubes. For the increasing initial mass share of air from 0.002 to 0.01 the number of rows of tubes, on which total condensation of water vapor occurs, grows from 12 to 25 (Fig. 4a). The increase in the number of rows of tubes results in a greater loss of pressure during the flow of gas through the bank. The consequence of that is a drop of temperature (which depends on pressure) of water vapor saturation (Fig. 4b). This deteriorates the conditions of condensation.

When the mixture of gases flows through the tube bank, its velocity (Fig. 5a) and the Reynolds number (Fig. 5b) drops. This drop is the fastest for the lowest mass share of air upstream of the first row of tubes. In the last rows of the tube bank the water vapor fades. This results in a drop of the flow velocity of the mixture of gases and the Reynolds number to values close to zero.

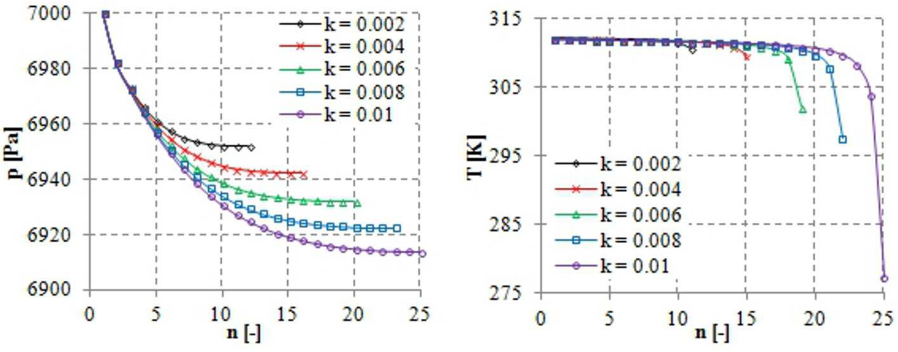

a) b)

Figure 4: Values of the pressure of the mixture of gases (a), and temperature of water vapor saturation in the subsequent rows of tubes (b) for the mass share of air upstream of the first row of tubes of $k = 0.002$, 0.004, 0.006, 0.008, and 0.01.

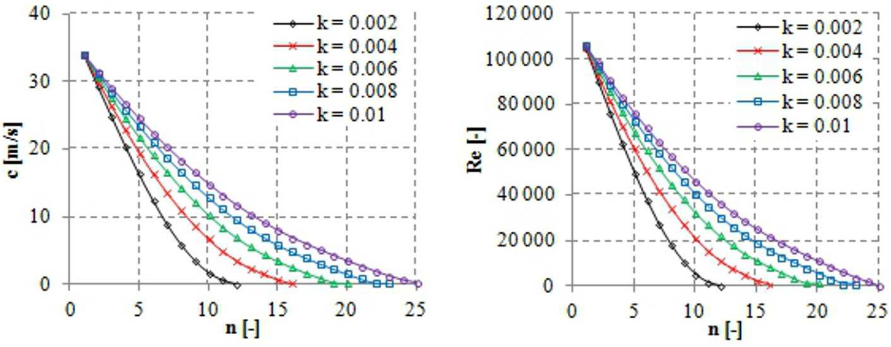

a) b)

Figure 5: Values of the velocities of gases (a), and Reynolds number in the subsequent rows of tubes (b) for the mass share of air upstream of the first row of tubes of $k = 0.002$, 0.004, 0.006, 0.008, and 0.01.

The total loss coefficient, depending on the geometry of the tube bank and the Reynolds number, grows in subsequent rows of tubes to the value of approx. 30 (Fig. 6a). This growth is the fastest for the lowest initial share of air. A relatively high value of the total coefficient of pressure loss in the last rows of tubes results in a small loss of pressure due to low flow velocities of the mixture in these rows (Figs. 5a and 6). The drop of pressure is the greatest in the first row of tubes and it decreases in the subsequent rows of the tube bank (Fig. 6b). The total drop of pressure increases linearly along with the initial mass share of air (Fig. 7). For k increasing from 0.002 to 0.01 the total static pressure loss grows from 48 to 85 Pa.

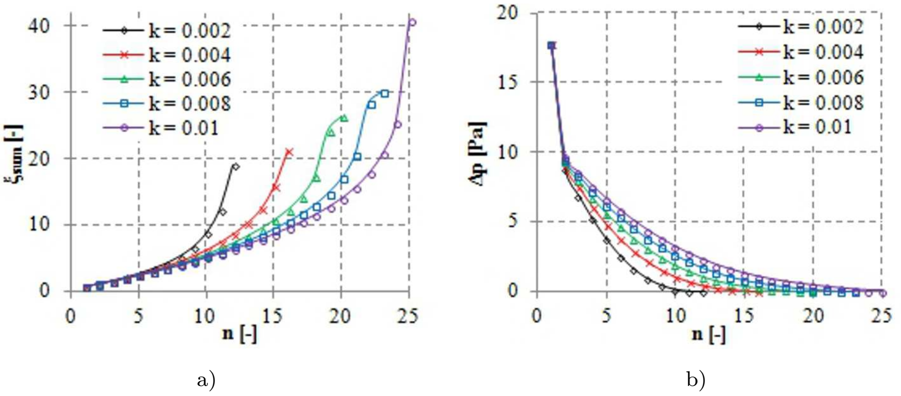

Figure 6: Values of the total loss coefficient (a) and pressure loss in the subsequent rows of tubes (b) for the mass share of air upstream of the first row of tubes of $k = 0.002$, 0.004, 0.006, 0.008, and 0.01.

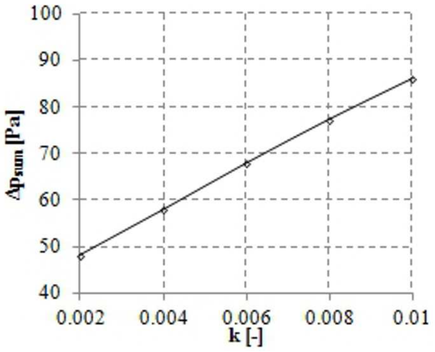

Figure 7: Values of the total drop of pressure of the mixture depending on the share of air upstream of the first row of tubes.

The partial pressure of water vapor, except the last rows, decreases smoothly in the model tube bank (Fig. 8a). The increment of partial pressure of air in this part of the tube bank has a similar character (Fig. 8b). In the last rows of tubes the partial pressure of water vapor drops abruptly and the partial pressure of air increases. This results from the small residual mass flow of water vapor and accumulation of air.

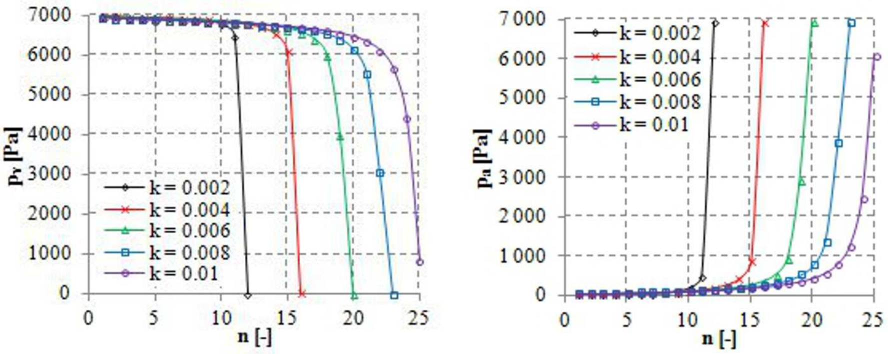

a) b)

Figure 8: Values of the partial pressure of water vapor (a) and partial pressure of air in the subsequent rows of tubes (b) for the mass share of air upstream of the first row of tubes of $k = 0.002$, 0.004, 0.006, 0.008, and 0.01.

The heat of evaporation depends on the partial pressure of water vapor and the saturation temperature. For majority of rows, the heat of evaporation is approx. 2410 kJ/kg (Fig. 9a). Due to a drop in the saturation, the value of the heat of evaporation in subsequent rows of tubes increases gradually. The Nusselt number for most of the rows assumes values of approx. 335 (Fig. 9b). In the last rows, an increase of the Nusselt number takes place, which results from a small difference between the temperature of the tube wall and the temperature of water vapor saturation. This increase also depends on the obtained course of heat of evaporation. The heat transfer coefficient α allowing for the presence of air in the condenser depends on the Nusselt number and the course of the function ε. The mass share of air upstream of the first row of tubes significantly influences the value of the heat transfer coefficient (Fig. 9c) and the heat flow (Fig. 9d) already at the front of the tube bank. For the first row of tubes, the heat transfer coefficient assumes the values from 3000 to 6000 W/m^{2}K and the heat flow from 150 to 280 kW. In the last rows of tubes the mass share of air k grows rapidly as a result of the fading water vapor. This results in a decrease of heat transfer coefficient, α.

The mass flow of gases flowing through the tube bank drops from approx. 0.8 kg/s to values close to zero (Fig. 10a), which results from the condensation of water vapor. The amount of mass flow of condensed water vapor in the rows of the tube bank mainly depends on the heat transfer coefficient and the difference between the temperature of the wall and the

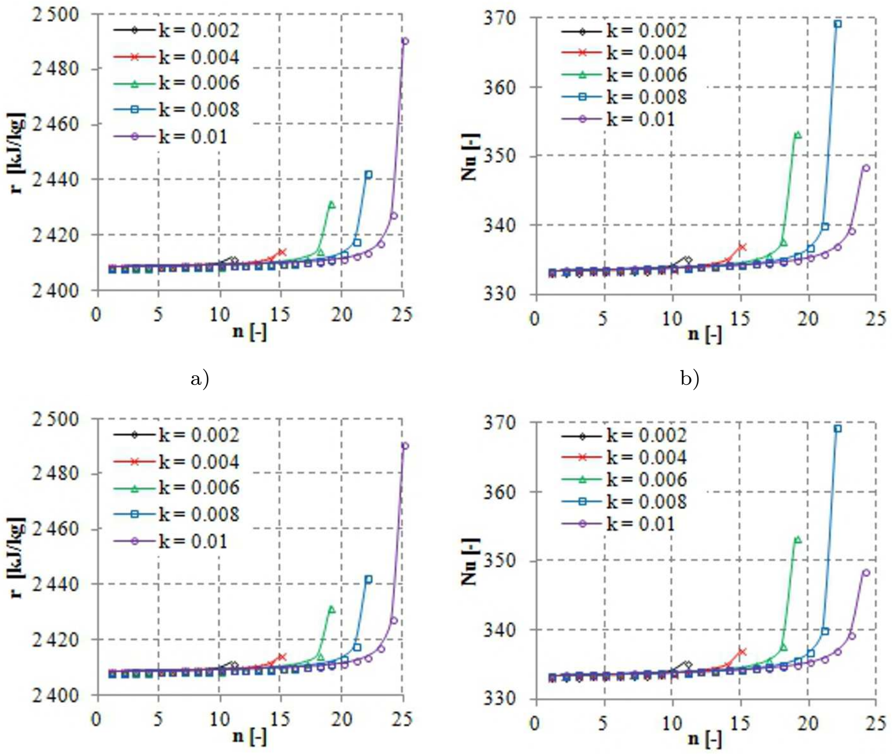

a) b)

c) d)

Figure 9: Values of the heat of evaporation (a), Nusselt number (b), heat transfer coefficient (c), heat flow in the subsequent rows of tubes (d) for the mass share of air upstream of the first row of tubes of k = 0.002, 0.004, 0.006, 0.008, and 0.01.

temperature of the mixture of gases. Hence, the courses of the characteristics of heat transfer coefficient, α, and Nusselt number, Nu (Figs. 9c and 9d), and condensed water vapor mass flow rate, $\Delta\dot{m}$, (Fig. 10b) are similar. The mass flow rate of condensed water vapor decreases as the gases flow through the condenser (Fig. 10b). A deterioration of the conditions of condensation results from the increase of the heat resistance of the air accumulating in the subsequent rows of tubes (Fig. 11) and the drop of the partial pressure of water vapor, which results in a drop of the water vapor saturation temperature. In the last rows of tubes one can see an abrupt increase in the mass share of air, k, (Fig. 11).

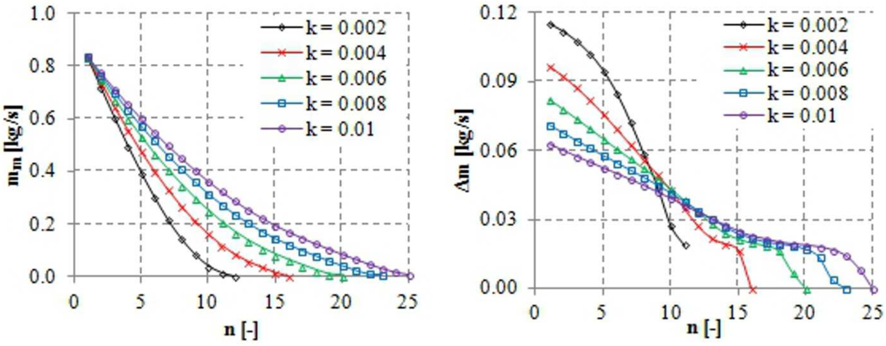

a) b)

Figure 10: Values of the mass flow rate of the mixture of gases (a), condensed water vapor mass flow in the subsequent rows of tubes (b) for the mass share of air upstream of the first row of tubes of $k = 0.002$, 0.004, 0.006, 0.008, and 0.01.

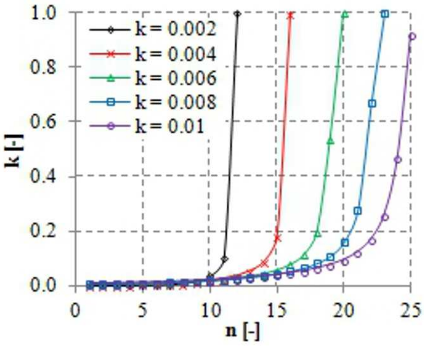

Figure 11: Values of the mass share of air in the subsequent rows of tubes for the mass share of air upstream of the first row of tubes of $k = 0.002$, 0.004, 0.006, 0.008, 0.01.

4 Conclusions

The presented calculation model allows determining of the average values of thermodynamic and flow parameters occurring in individual rows of tubes of a condenser. Based on the results included in the paper, it can be observed that a relatively small increase in the mass share of air in the water vapor entering the condenser results in a change of the flow parameters and a significant deterioration of the heat flow conditions. Additional heat resistance triggered by the accumulation of air results in a need to increase the number of rows of tubes for a successful condensation of water vapor to take place. The proposed calculation model allows determining of the length of the tube bank in which the water vapor condensation occurs.

The resultant length of the tube bank depends on the initial velocity, pressure of the mixture of gases and the mass share of air. The model also allows determining the row, in which the temperature of water vapor saturation is close to the temperature of the tube wall, in which case a significant deterioration or even pausing of the condensation process occurs. This and the knowledge of the mass share of air in each of the rows allow determining the spots where air accumulates in the tube bank of the condenser and its successful extraction.

The presented model assumes a constant value of the pressure and velocity in the intake plane to the model tube bank of the condenser. In the next stage of research, analysis is planned allowing for determination of the thermal and flow parameters in a tube bank of a condenser of a fixed number of rows and variable initial parameters of the air/water vapor mixture.

Received 8 August 2016

References

[1] Bin Ren, Li Zhang, Hong Xu, Jun Cao, Zhenyu Tao: *Experimental study on condensation of steam/air mixture in a horizontal tube.* Exp. Therm. Fluid Sci. **58**(2014), 145–155.

[2] Hobler T.: *Heat Transfer and Heat Exchangers.* Warszawa, WNT 1986 (in Polish).

[3] Huiqiang Xu, Zhongning Sun, Haifeng Gu, Hao Li: *Experimental study on the effect of wall-subcooling on condensation heat transfer in the presence of non-condensable gases in a horizontal tube.* Ann. Nucl. Energy **90**(2016), 9–21.

[4] Joachimiak M., Krzyślak P.: *The analysis of the changes in the partial pressure of gases and the share of air during a flow through a tube bank inside a condenser.* JMTE **65**(2013), 4, 13–21.

[5] Madejski J.: *Heat Transfer Theory.* PWN, Warszawa 1963 (in Polish).

[6] Marto P.J.: *Heat Transfer and two-phase flow during shell-side condensation.* Heat Transfer Eng. **5**(1984), 1-2, 31–61.

[7] Paszkowski S.: *Numerical Application of Multinomials and Chebyshev Series.* PWN, Warszawa 1975 (in Polish).

[8] Rusowicz A.: *Problems of Mathematical Modeling of Power Condensers.* Oficyna Wydawnicza Politechniki Warszawskiej, Warszawa 2013 (in Polish).

[9] Wagner W., Kretzschmar H.J.: *International Steam Tables, Properties of Water and Steam Based on the Industrial Formulation IAPWS-IF97.* Springer-Verlag, 1998.

[10] Wiśniewski S., Wiśniewski T.S.: *Heat Transfer*. WNT, Warszawa 2012 (in Polish).

[11] *Release on the IAPWS Formulation 2008 for the Viscosity of Ordinary Water Substance*. IAPWS, Berlin 2008.

archives
of thermodynamics
Vol. **38**(2017), No. 3, 135–148
DOI: 10.1515/aoter-2017-0020

Selected studies of flow maldistribution in a minichannel plate heat exchanger

PAWEŁ DĄBROWSKI[*]
MICHAŁ KLUGMANN
DARIUSZ MIKIELEWICZ

Gdańsk University of Technology, Faculty of Mechanical Engineering, Department of Energy and Industrial Apparatus, Narutowicza 11/12, 80-233 Gdańsk, Poland

Abstract Analysis of the state of-the-art in research of minichannel heat exchangers, especially on the topic of flow maldistribution in multiple channels, has been accomplished. Studies on minichannel plate heat exchanger with 51 parallel minichannels with four hydraulic diameters, i.e., 461 μm, 574 μm, 667 μm, and 750 μm have been presented. Flow at the instance of filling the microchannel with water at low flow rates has been visualized. The pressure drop characteristics for single minichannel plate have been presented along with the channels blockage, which occurred in several cases. The impact of the mass flow rate and channels' cross-section dimensions on the flow maldistribution were illustrated.

Keywords: Pressure drop; Minichannel; Plate; Heat exchanger; Flow maldistribution; Channel blockage

Nomenclature

A – surface area, m^2
D – intake conduit diamater, m
D_h – hydraulic diamater, m
f – average friction coefficient for intake conduit flow
h – convective heat transfer coefficient, W/m^{2}K

---

[*] Corresponding Author. Email pawel.dabrowski@pg.edu.pl

k_f – fluid thermal conductivity, W/m K
$\dot{m}$ – mass flow rate, kg/s
Nu_∞ – Nusselt number for fully-developed temperature profile
P – pressure in the inlet conduit, Pa
P_w – wetted perimeter, m
W – velocity in the inlet conduit, m/s
Z – axial coordinate, m

Greek symbols

β – average velocity ratio in the intake conduit
ΔP – pressure drop, Pa
ρ – fluid density, kg/m^3

1 Introduction

All technology sectors are endeavoring to miniaturization with simultaneous improvement of the performance of considered appliances. That causes the increase of heat flux which is necessary to be dissipated from the surface, so the cooling systems have also to be improved. Hence, heat exchangers that are inherently an integral part of cooling systems are undergoing modifications. Well-known conventional or even compact heat exchangers are insufficient in many cases. Poor thermal management is a main drawback on the way of further miniaturization. Hence, there is a need to focus on modern designs of heat exchangers and to intensify the heat transfer.

Tuckerman and Pease [1] clearly demonstrated, about four decades ago, that convective heat transfer coefficient directly depends on the hydraulic diameter of the channel, which in minichannels is featuring the laminar character. Hence, for the constant value of the Nusselt number, Nu_∞, the product of heat transfer coefficient and hydraulic diameter is constant [2]

$$h = \frac{k_f \mathrm{Nu}_\infty}{D_h} \; . \tag{1}$$

As can be seen from Eq. (1) the smaller the hydraulic diameter, the higher is the convective heat transfer coefficient. That is also accompanied by a significant elevation of pressure losses in the exchanger. The latter conclusion introduced new generation of heat exchangers, i.e., minichannel heat exchangers, where the realized flow is predominantly laminar. Micro- and minichannels are different from the conventional channels in terms of channel hydraulic diameters. Ranges of hydraulic diameters proposed in [3]

$$D_h = \frac{4A}{P_w} \; , \tag{2}$$

are as follows: $D_h > 6$ mm for macrochannels, 1 mm $< D_h < 6$ mm for minichannels, 0.1 mm $< D_h < 1$ mm for mesochannels and 1 μm $< D_h < 100$ mm for microchannels. Different classification was postulated in [4], i.e., channels can be defined as: conventional when $D_h > 3$ mm, mini when 0.2 mm $< D_h < 3$ mm and micro when 10 μm $< D_h < 200$ μm.

Mini- or microchannel heat exchangers are widely used in many industries, i.e., power industry (water cooled turbine blades, rocket nozzle cooling, fusion reactor blanket cooling, domestic micro-combined heat and power) [5-9], information technology industry (computer data centers) [10,11], avionics industry (avionics cooling) [12], space industry (cooling of satellite electronics) [13], solar industry (solar photovoltaic panels) [14], automotive industry (cooling of hybrid vehicle power electronics) [15], chemical and biological industry [16,17], refrigeration industry (microfin tubes in residential cooling) [4] or cryogenic industry (heat exchangers for hydrogen storage systems) [18]. Kandlikar [19] reported that microchannels may provide a heat flux dissipation ratio up to 10^3 W/cm^2.

Small diameter of channels causes a low mass flux of fluid that is able to flow through it and a moderate heat flux that can be dissipated from the cooled surface as a result. That is a reason for application of many parallel minichannels with common inlet and outlet manifold in minichannel heat exchangers. But this kind of construction causes a flow maldistribution. According to Mueller and Chiou [20], prefix ‘mal’ means defective or bad, so if a comparison is made to a uniform distribution, then ‘maldistribution’ means unequal amount of fluid or unequal flow velocity in each channel. In fact, there are two kinds of maldistribution connected with fabrication conditions: gross maldistribution and passage-to-passage maldistribution [21]. The first one is associated with mechanical design, mainly improper header configuration and the second one is caused by various manufacturing tolerances. But flow maldistribution can also appear due to heat transfer process, two-phase flows and fouling or corrosion [20].

Very significant aspect in heat exchangers designing is to choose proper inlet and outlet manifold configuration. Two main structures of manifolds can be distinguished, namely consecutive and bifurcation [22]. They are shown in Fig. 1 [23]. In consecutive manifolds the main fluid stream is divided continuously into channels as it reaches them. This structure is very common due to their simplicity and lower pressure drop comparing to bifurcation type. However, consecutive manifold is susceptible to flow maldistribution. Bifurcation structure is inspired by the nature and can be

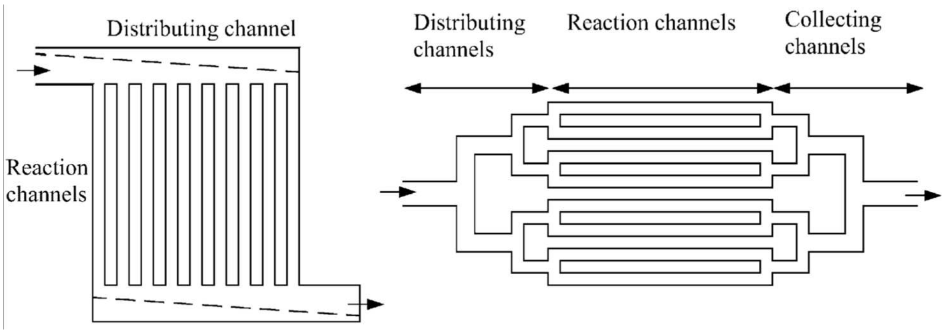

Figure 1: Schematic for consecutive (left) and bifurcation (right) manifold of minichannel heat exchanger [23].

seen in trees, cracks in the dry ground, blood circulation system and lungs [24]. Here, main fluid stream is divided into two streams. Each stream is then further subdivided into two more till the number of divisions matches the number of channels. In the end they are merging till main fluid stream creation. In [25] comparison of several manifolds was made and it is found out that the bifurcation structure gives much better distribution, which resulted in very uniform temperature field over the heating surface.

There are several papers [26–30] that introduce analytical models which describe the flow distribution in manifolds. One that could be used to predict the velocity distribution, flow distribution, and pressure drop was shown in [26]:

$$\frac{1}{\rho}\frac{dP}{dZ} + \frac{f}{2D}W^2 + (2-\beta)\,W\frac{dW}{dZ} = 0\,. \tag{3}$$

This model contain the mass balance, momentum balance and utilized Bernoulli's equation and was prepared for macrochannel plate heat exchangers, however it is also applicable for micro- or mini- scale. The aim of many authors' projects is to elaborate a method that will allow to predict a single or two-phase flow distribution, pressure drops and heat transfer in a minichannel heat exchangers very precisely. Hence, many papers are focused on a numerical simulations as a predictive tool for flow distribution in parallel micro- or minichannels. Tuo and Hrnjak [31] modeled a microchannel evaporator with a consideration that every single microchannel is a unique flow path and that various pressure drops along each flow path must add up to the same overall pressure drop. Comparison of predicted and measured evaporator cooling capacity shows that nearly 88% of the data points are predicted within ±5% deviation from the experimental results. Comparison of predicted and measured pressure drop shows that nearly 92% of the data points are predicted within ±20% deviation from the experimental results. New microchannel heat exchanger cosimulation approach was proposed by [32]. It combines a detailed header simulation based on commercial computational fluid dynamics (CFD) code (Fluent) and a robust effectiveness-based finite volume tube-side heat transfer and refrigerant flow modeling tool. Also in [33] simulation has been done to predict the flow distribution in the inlet header of plate-fin heat exchangers. Authors found out that flow maldistribution is strongly pronounced at greater Reynolds number and two modified headers with a two-stage-distributing structure were recommended to improve the distribution. Nielsen *et al.* [34] proposed a numerical method to quantify the heat transfer degradation associated with the non-uniform flow channel thickness in microchannel heat exchanger. Lalot *et al.* [35] suggested analytical expression that allows to approximate fluid velocity field in microchannel heat exchanger. Authors compared a computed results with experiments and obtained a good estimation.

Many authors conducted experiments that have allowed to indicate parameters that affect flow distribution. Minqiang *et al.* [36] carried out CFD-based studies of maldistribution in 20 parallel channels. The variable parameters were manifold's dimensions (length, magnitude and position of inlet/outlet) and microchannel's dimensions (length, width, and depth). All this parameters have influence on maldistribution. Kumaraguruparan *et al.* [37] conducted in numerical and experimental research of flow maldistribution in parallel microchannels in U-type configuration. These studies have shown the presence of flow separation, backflows and vortex at the inlet. These phenomena cause maldistribution but the increase of viscosity of the fluid reduces these effects. Another research on the influence of flow maldistribution on temperature and hot spot formation in 10 parallel channels with various hydraulic diameter was carried out in [38]. Authors investigated and compared maldistribution on three channel flow configurations (U-, Z-, and I-type) and various heat flux generated. They found out that the smaller the diameter of channels, the smaller the maldistribution. Thus the temperature difference over the surface was also smaller. Other researchers [39] found out that the best distribution is obtained when the fluid enters the inlet header perpendicular to the length of the header. Moreover rectangular header shape gives lower maldistribution at high flow rate while trapezoidal and triangular header shape gives lower maldistribution at low flow rate. It is found that irrespectively of header shape or flow inlet configuration the flow becomes more uniform at higher flow rate.

Hydraulic characteristics of minichannel heat exchangers are the prerequisites for using them in any thermal applications. Knowledge of pressure drop at different flow rates is essential to be able to predict the pumping power. Current studies are scheduled to check the potential of minichannel heat exchanger as an evaporator in a perspective design of the solar thermosiphon installation. For that reason authors measured pressure drop in single phase flow at low volume flow rates, typical which occurs in thermosiphon installations and visualized the flow distribution in minichannel heat exchanger.

2 Experimental setup

Authors used four model plate heat exchangers with a set of parallel minichannels made of brass. The measuring section contained 51 channels (connected by common inlet and outlet trapezoidal manifold) of 40 mm length with rectangular cross-section of different dimensions, i.e., width x depth were respectively: 1 mm×0.3 mm/0.4 mm/0.5 mm/0.6 mm (corresponding to hydraulic diameter of 461 μm, 574 μm, 667 μm, and 750 μm, respectively). The model geometry was shown in Fig. 2.

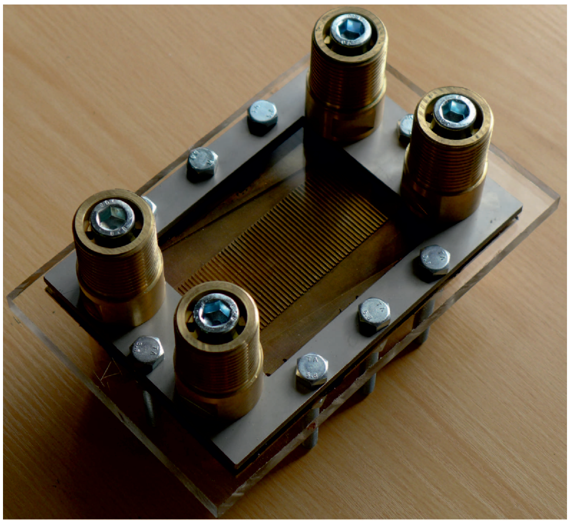

Figure 2: Model minichannel plate heat exchanger.

In order to observe the working fluid, the section was covered with 10 mm acrylic glass sheet. Authors were filling empty heat exchanger with water at various mass flow rates (0.83–8.33 g/s), and recorded the entire section with Panasonic Lumix LX7 camera. This camera allows to record sequences of records at 1920×1080 resolution. Other parameters of the camera were: shutter speed 50–500 μs, frame rate 50 fps, focal length (small pic. eqiv.) = 70 mm. The traditional 1000 W halogen lamp was used for illumination of the measuring section. At the same time, the pressure drop at the heat exchanger was measured using an ATM.1ST electronic pressure transmitter with a measuring range of 0–5 kPa. It worked with the National Instruments SCXI-1600 measuring interface and LabView environment. In addition, the test rig has been equipped with a valve and installation for removing water from the test section before, every measuring series were accomplished, using compressed air. This allowed to prepare the characteristics of pressure drop and to observe the flowing fluid and possible flow maldistribution in the individual channels.

Selection of the minichannel heat exchangers geometry results from authors' long-standing experience [40–42] of investigations in minichannels with various aspects, ranging from single phase to two-phase flows.

3 Results and discussion

Authors obtained a repeatability of results and stated that air content in the flowing medium has no influence on the flow profile. That is clearly seen in Fig. 3. The shape of flow profile is caused by the geometry of test section, i.e., shape and dimensions of inlet and outlet manifold and cross-section of minichannels itself. Fig. 3 shows also a phenomenon of flow maldistribution. The heads of flow in every single channel are not collinear and have different velocity, i.e., they have filled channels at different time. It was observed that the flow maldistribution depends on mass flow rate (higher flow rate, more uniform distribution) and hydraulic diameter of channels (lower hydraulic diameter, more uniform distribution). It corresponds with other authors' observations, that is to reduce the flow maldistribution, the effect of inertia should be reduced and the effect of viscosity should be increased. Hence, larger pressure drop should be in the channels and lower in inlet and outlet manifold [31,36,37,39].

Most of studies are made in the steady state, e.g., at constant flow rate, at constant temperature or constant heat flux. However, every installation

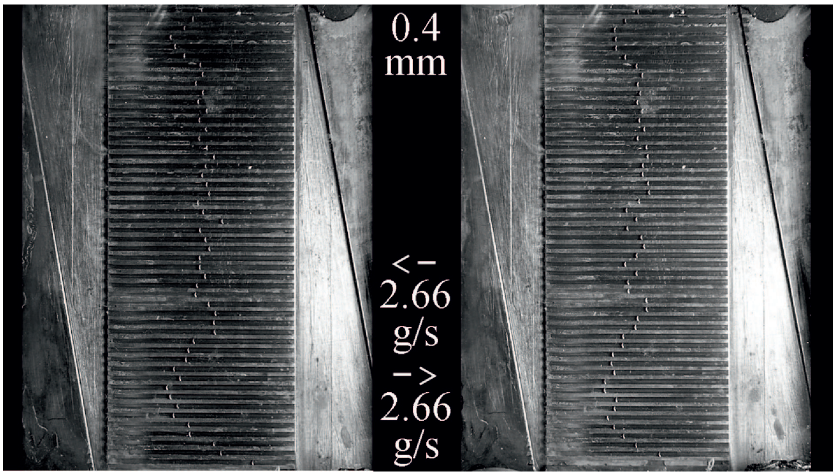

Figure 3: Comparison of flow profiles for two different measurement series concerning the same minichannel depth (0.4 mm) at equal flow rates of 2.66 g/s. Aerated water (left), degassed water (right).

has to be started up at least once but in many cases the moment when the working fluid is starting to flow occurs periodically. Current studies show the moment when fluid is starting to flow and enters the model minichannel heat exchanger. This situation is common in solar thermosiphon installation, where fluid enters the evaporator due to density differences of hot and cold medium as the solar energy is transferred. This approach allowed to observe the phenomena of channel blockage, which will be analysed in the paper.

In Fig. 4 the test section (geometry with the hydraulic diameter of 750 μm) when the head of flow reached the outlet at different flow rates was presented. The white lines represent blocked channels which were not filled with water entirely. Black lines represent blocked channels filled with water but blocked with the air bubble in outlet manifold. The working fluid does not flow in the channels that are not filled with water entirely, so the heat exchanger works unevenly. Uneven temperature distribution over the surface and lower heat exchanger's efficiency can be observed due to this situation. It was seen that more minichannels are inactive at low flow rates. The amount of inactive channels at the lowest flow rate (1 g/s) is 16 and for 3.5 g/s, 6.16 g/s, and 8.16 g/s is getting smaller (7, 3, and 0, respectively). It is clearly shown that it low flow rates should be avoided.

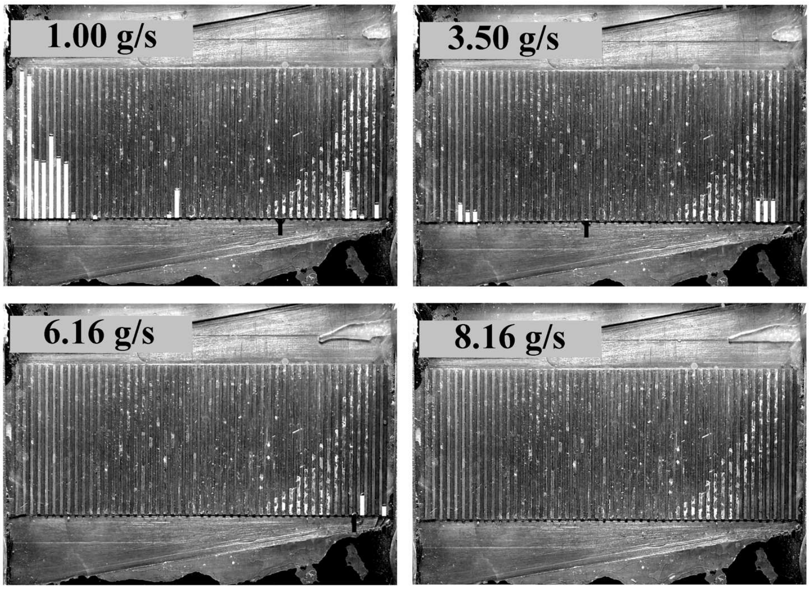

Figure 4: View of test section with blocked channels at different flow rates in the same geometry (minichannel depth of 0.6 mm).

In Fig. 5 was presented the test section in similar situation as before but this time, the depth of the channel is a varying parameter and the flow rate in every case is the same and equals 1.83 g/s. It is seen that bigger hydraulic diameter of channels causes a bigger amount of the inactive channels. This amount rises from 4 inactive channels for the depth of minichannels' equal to 0.3 mm to 16 inactive channels for 0.6 mm minichannels' depth. For 0.4 mm and 0.5 mm depth amount of inactive channels are 7 and 10, respectively. It can be deduced that channels are blocked with recurrent mechanism that is strictly connected with flow maldistribution. For every geometry, the critical value of flow rate below which the maldistribution and channel blockage are severe, can be also distinguished. These issues will be the subject of wider research and separate publication.

Total pressure drop, which contains of pressure drop in inlet manifold, 51 parallel minichannels and outlet manifold was also measured. It is shown in Fig. 6. Values in Fig. 6 correspond to pressure drops in single minichannel plate itself, without hydraulic resistance in valves at the inlet and outlet. Pressure drop as a function of flow rate, as expected, increase as the flow rate increases, and increase as the hydraulic diameter of channels decreases.

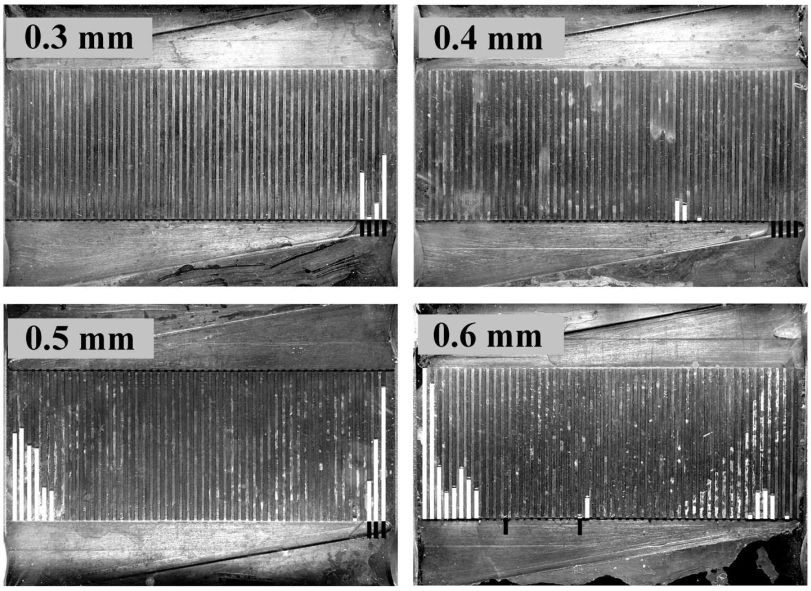

Figure 5: View of test section with blocked channels in different geometries (minichannel depths of 0.3 mm – 0.6 mm) at the same flow rate of 1.83 g/s.

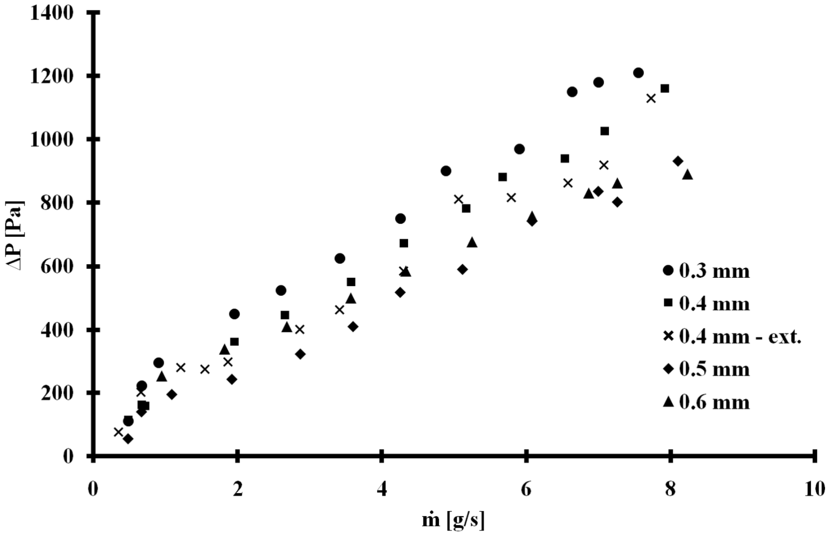

Figure 6: Pressure drop as a function of mass flow rate for various minichannels depth.

In current studies value of pressure drop does not exceed 1250 Pa, but worth remembering is the fact that this is a model of the heat exchanger with single plate and the real heat exchanger with minichannel plates should contain a number of them.

Authors made also pressure drop profiles as a function of the filling time of the section. These curves are reproducible and characteristic, which are related to the broader characteristics of the flow phenomena in the section. These issues will be the subject of wider research and separate publication.

4 Conclusions

Hydrodynamic studies in minichannel plate heat exchanger were made. Authors measured pressure drops in plate heat exchanger which contains of 51 parallel minichannels with rectangular cross-section of various hydraulic diameter (461 μm, 574 μm, 667 μm, and 750 μm) connected by trapezoidal inlet and outlet manifold. Current studies were preliminary researches to check the potential of minichannel heat exchanger as an evaporator in solar thermosiphon installation. The single phase flow visualization at the moment of filling the model heat exchanger allowed to observe the flow maldistribution and the channels blockage phenomenon. Authors noticed the dependency of mass flow rate and channels' cross-section dimensions on maldistribution and blockage mechanism.

Due to the critical flow rate below which the deterioration of the work occurs and the parabolic nature of the pressure drop curve, there is a narrow range of flow at which model geometries can work optimally. It is a range in the order of 5 g/s to 8.33 g/s. In this range the pressure drops are in range of 600–1250 Pa, depending on the hydraulic diameter of channels. These values seem to be appropriate for the intended uses of the assumed geometry in a solar thermosiphon installation.

Acknowledgements The work presented in the paper was funded from the National Science Centre research project No. 2015/19/D/ST8/03201 in years 2016-2019.

Received 21 January 2017

References

[1] Tuckerman D.B.: Pease RFW *High-performance heat sinking for VLSI.* IEEE Electr. Device Lett **2**(1981), 5, 126–129. DOI: 10.1109/EDL.1981.253672.

[2] Teng J.: *Fluid Dynamics in Microchannels.* Intechopen 2012, 403–436. DOI: 10.1002/97835276314453.

[3] Mehendale S.S., Jacobi A.M., Shah R.K.: *Fluid flow and heat transfer at micro- and meso-scales with application to heat exchanger design.* Appl. Mech. Rev. **53**(2000), 7, 175–193.

[4] Kandlikar S.G., Grande W.J.: *Evolution of microchannel flow passages-thermohydraulic performance and fabrication technology.* Heat Tran. Eng. **24**(2003), 1, 3–17. DOI: 10.1080/014576303040405.

[5] Ornatskii A.P., Vinyarskii L.S.: *Heat transfer crisis in a forced flow of under-heated water in small-bore tubes.* Teplofiz. Vysok. Temp. **3**(1965), 441–451.

[6] Mudawar I.A., El-Masri M.A. Wu C.S., Ausman-Mudawwar J.R.: *Boiling heat transfer and critical heat flux in high-speed rotating liquid films.* Int. J. Heat Mass Tran. **28**(1985), 4, 795–806. DOI: 10.1016/0017-9310(85)90230-3

[7] Sturgis J.C., Mudawar I.: *Assessment of CHF enhancement mechanisms in a curved, rectangular channel subjected to concave heating.* J. Heat Transfer **121**(1999), 2, 394–404.

[8] Hall D.D., Mudawar I.: *Ultra-high critical heat flux (CHF) for subcooled water flow boiling? II: high-CHF database and design equations.* Int. J. Heat Mass Transf. **42**(1999), 8, 1429–1456. DOI: 10.1016/S0017-9310(98)00242-7

[9] Mikielewicz D., Mikielewicz J.: *A thermodynamic criterion for selection of working fluid for subcritical and supercritical domestic micro CHP.* Appl. Therm. Eng. **30**(2010), 16, 2357–2362. DOI: 10.1016/j.applthermaleng.2010.05.035.

[10] Mudawar I: *Assessment of high-heat-flux thermal management schemes.* IEEE Trans. Comp. Pack. Technol. **24**(2001), 2, 122–141. DOI: 10.1109/6144.926375.

[11] Mudawar I. *Two-phase microchannel heat sinks: theory, applications, and limitations.* J. Electron Packag. **133**(2011), 4, 41002–41031.

[12] Jimenez P.E., Mudawar I.: *A multi-kilowatt immersion-cooled standard electronic clamshell module for future aircraft avionics.* J Electron Packag. **116**(1994), 3, 220–229.

[13] LaClair T.J., Mudawar I.: *Thermal transients in a capillary evaporator prior to the initiation of boiling.* Int. J. Heat Mass Tran. **43**(2000), 21, 3937–3952. DOI: 10.1016/S0017-9310(00)00042-9

[14] Reddy S.R., Ebadian M.A., Lin C-X.: *A review of PVT systems: thermal management and efficiency with single phase cooling.* Int. J. Heat Mass Tran. **91**(2015), 861–871. DOI: 10.1016/j.ijheatmasstransfer.2015.07.134.

[15] Mudawar I., Bharathan D., Kelly K., Narumanchi S.: *Two-phase spray cooling of hybrid vehicle electronics.* IEEE Trans. Components Packag. Technol. **32**(2009), 2, 501–512. DOI: 10.1109/TCAPT.2008.2006907.

[16] JY R., LY L., XS D. *et al.*: *Numerical investigations on characteristics of methane catalytic combustion in micro-channels with a concave or convex wall cavity.* Energy Convers Manag **97**(2015), 188–195. DOI: 10.1016/j.enconman.2015.03.058.

[17] Berthier J., Brakke K.A., Furlani E.P. *et al*: *Whole blood spontaneous capillary flow in narrow V-groove microchannels.* Sensors Actuators, B Chem **206**(2015), 258–267. DOI: 10.1016/j.snb.2014.09.040.

[18] Kim S.M., Mudawar I.: *Review of databases and predictive methods for heat transfer in condensing and boiling mini/micro-channel flows.* Int. J. Heat Mass Tran. **77**(2014), 627–652. DOI: 10.1016/j.ijheatmasstransfer.2014.05.036.

[19] Kandlikar S.G.: *High flux heat removal with microchannels – A roadmap of challenges and opportunities.* Heat Transfer Eng. **26**(2005), 8, 5–14. DOI: 10.1080/01457630591003655.

[20] Mueller A.C., Chiou J.P.: *Review of various types of flow maldistribution in heat exchangers.* Heat Tranfer Eng. **9**(1988),36–50. DOI: 10.1080/01457638808939664.

[21] Wen J., Li Y.: *Study of flow distribution and its improvement on the header of plate-fin heat exchanger.* Cryogenics (Guildf) **44**(2004), 11, 823–831. DOI: 10.1016/j.cryogenics.2004.04.009.

[22] Wang J.: *Theory of flow distribution in manifolds.* Chem. Eng. J. **168**(2011), 3, 1331–1345. DOI: 10.1016/j.cej.2011.02.050.

[23] Amador C., Gavriilidis A., Angeli P.: *Flow distribution in different microreactor scale-out geometries and the effect of manufacturing tolerances and channel blockage.* Chem. Eng. J. **101**(2004), 1-3, 379–390. DOI: 10.1016/j.cej.2003.11.031.

[24] Bejan A., Errera M.R.: *Deterministic tree networks for fluid flow: geometry for minimal flow resistance between a volume and one point.* Fractals **5**(1997), 4, 685–695. DOI: 10.1142/S0218348X97000553.

[25] Ramos-Alvarado B., Li P., Liu H., Hernandez-Guerrero A.: *CFD study of liquid-cooled heat sinks with microchannel flow field configurations for electronics, fuel cells, and concentrated solar cells.* Appl. Therm. Eng. **31**(2011), 14-15, 2494–2507. DOI: 10.1016/j.applthermaleng.2011.04.015.

[26] Bassiouny M.K., Martin H.: *Flow distribution and pressure drop in plate heat exchangers-I U-type arrangement.* Chem. Eng. Sci. **39**(1984), 4, 693–700. DOI: 10.1016/0009-2509(84)80176-1.

[27] Bassiouny M.K., Martin H.: *Flow distribution and pressure drop in plate heat exchangers-II Z-type arrangement.* Chem. Eng. Sci. **39**(1984), 4, 701–704. DOI: 10.1016/0009-2509(84)80177-3.

[28] Bajura R.A.: *A model for flow distribution in manifolds.* J. Eng. Power **93**(1971), 1, 7–12.

[29] Acrivos A., Babcock B.D., Pigford R.L.: *Flow distributions in manifolds.* Chem. Eng. Sci. **10**(1959), 1-2, 112–124. DOI: 10.1016/0009-2509(59)80030-0.

[30] Wang J., Gao Z., Gan G., Wu D.: *Analytical solution of flow coefficients for a uniformly distributed porous channel.* Chem. Eng. J. **84**(2001), 1, 1–6. DOI: 10.1016/S1385-8947(00)00263-1.

[31] Tuo H., Hrnjak P.: *Effect of the header pressure drop induced flow maldistribution on the microchannel evaporator performance.* Int. J. Refrig. **36**(2013), 8, 2176–2186. DOI: 10.1016/j.ijrefrig.2013.06.002.

[32] Huang L., Lee M.S., Saleh K. *et al.*: *A computational fluid dynamics and effectiveness-NTU based co-simulation approach for flow mal-distribution analysis in microchannel heat exchanger headers.* Appl. Therm. Eng. **65**(2014), 1-2, 447–457. DOI: 10.1016/j.applthermaleng.2014.01.046.

[33] Zhang Z., Li Y.: *CFD simulation on inlet configuration of plate-fin heat exchangers.* Cryogenics (Guildf) **43**(2003), 12, 673–678. DOI: 10.1016/S0011-2275(03)00179-6.

[34] Nielsen K.K., Engelbrecht K., Christensen D.V. *et al.*: *Degradation of the performance of microchannel heat exchangers due to flow maldistribution.* Appl. Therm. Eng. **40**(2012), 236–247. DOI: 10.1016/j.applthermaleng.2012.02.019.

[35] Lalot S., Florent P., Lang S.K., Bergles A.E.: *Flow maldistribution in heat exchangers.* Appl. Therm. Eng. **19**(1999), 8, 847–863. DOI: 10.1016/S1359-4311(98)00090-8.

[36] Minqiang P., Dehuai Z., Yong T., Dongqing C.: *CFD-based study of velocity distribution among multiple parallel microchannels.* J. Comput. **4**(2009), 11, 1133–1138. DOI: 10.4304/jcp.4.11.1133-1138.

[37] Kumaraguruparan G., Kumaran R.M., Sornakumar T., Sundararajan T.: *A numerical and experimental investigation of flow maldistribution in a micro-channel heat sink.* Int. Commun. Heat Mass Tran. **38**(2011), 10, 1349–1353. DOI: 10.1016/j.icheatmasstransfer.2011.08.020.

[38] Manoj Siva V., Pattamatta A., Das S.K.: *Effect of flow maldistribution on the thermal performance of parallel microchannel cooling systems.* Int. J. Heat Mass Tran. **73**(2014), 424–428. DOI: 10.1016/j.ijheatmasstransfer.2014.02.017.

[39] Anbumeenakshi C., Thansekhar M.R.: *Experimental investigation of header shape and inlet configuration on flow maldistribution in microchannel.* Exp. Therm. Fluid Sci. **75**(2016), 156–161. DOI: 10.1016/j.expthermflusci.2016.02.004.

[40] Mikielewicz D., Klugmann M.: *A study of flow boiling heat transfer in minichannels.* Arch Thermodyn. **29**(2008), 2, 73–84.

[41] Mikielewicz D., Klugmann M., Wajs J.: *Flow boiling intensification in minichannels by means of mechanical flow turbulising inserts.* Int. J. Therm. Sci. **65**(2013), 79–91. DOI: 10.1016/j.ijthermalsci.2012.10.002.

[42] Mikielewicz D., Wajs J., Andrzejczyk R., Klugmann M.: *Pressure drop of HFE7000 and HFE7100 during flow condensation in minichannels.* Int J. Refrig. **68**(2016), 226–241. DOI: 10.1016/j.ijrefrig.2016.03.005.

Notes for Contributors

ARCHIVES OF THERMODYNAMICS publishes original papers which have not previously appeared in other journals. The journal does not have article processing charges (APCs) nor article submission charges. The language of the papers is English. The paper should not exceed the length of 25 pages. All pages should be numbered. The plan and form of the papers should be as follows:

1. The heading should specify the title (as short as possible), author, his/her complete affiliation, town, zip code, country and e-mail. Please indicate the corresponding author. The heading should be followed by *Abstract* of maximum 15 typewritten lines and *Keywords*.
2. More important symbols used in the paper can be listed in *Nomenclature*, placed below *Abstract* and arranged in a column, e.g.:
   u – velocity, m/s
   v – specific volume, m/kg
   etc.
   The list should begin with Latin symbols in alphabetical order followed by Greek symbols also in alphabetical order and with a separate heading. Subscripts and superscripts should follow Greek symbols and should be identified with separate headings. Physical quantities should be expressed in SI units (*Système International d'Unités*).
3. All abbreviations should be spelled out first time they are introduced in the text.
4. The equations should be each in a separate line. Standard mathematical notation should be used. All symbols used in equations must be clearly defined. The numbers of equations should run consecutively, irrespective of the division of the paper into sections. The numbers should be given in round brackets on the right-hand side of the page.
5. Particular attention should be paid to the differentiation between capital and small letters. If there is a risk of confusion, the symbols should be explained (for example *small c*) in the margins. Indices of more than one level (such as B_{f_a}) should be avoided wherever possible.
6. Computer-generated figures should be produced using **bold lines and characters**. No remarks should be written directly on the figures, except numerals or letter symbols only. Figures should be as small as possible while displaying clearly all the information requires, and with all lettering readable. The relevant explanations can be given in the caption.
7. The figures, including photographs, diagrams, etc., should be numbered with Arabic numerals in the same order in which they appear in the text. Each figure should have its own caption explaining the content without reference to the text.
8. Computer files on an enclosed disc or sent by e-mail to the Editorial Office are welcome. The manuscript should be written as a MS Word file – $*$.*doc*, $*$.*docx* or LaTeX file – $*$.*tex*. For revised manuscripts after peer review process, figures should be submitted as separate graphic files in either vector formats (PostScript (PS),

Encapsulated PostScript (EPS), preferable, CorelDraw (CDR), etc.) or bitmap formats (Tagged Image File Format (TIFF), Joint Photographic Experts Group (JPEG), etc.), with the resolution not lower than 300 dpi, preferably 600 dpi. These resolutions refer to images sized at dimensions comparable to those of figures in the print journal. Therefore, electronic figures should be sized to fit on single printed page and can have maximum 120 mm x 170 mm. Figures created in MS World, Exel, or PowerPoint will not be accepted. The quality of images downloaded from websites and the Internet are also not acceptable, because of their low resolution (usually only 72 dpi), inadequate for print reproduction.

9. The references for the paper should be numbered in the order in which they are called in the text. Calling the references is by giving the appropriate numbers in square brackets. The references should be listed with the following information provided: the author's surname and the initials of his/her names, the complete title of the work (in English translation) and, in addition:

   (a) for books: the publishing house and the place and year of publication, for example:
   [1] `Holman J.P.:` *`Heat Transfer`*`. McGraw-Hill, New York 1968.`

   (b) for journals: the name of the journal, volume (Arabic numerals in bold), year of publication (in round brackets), number and, if appropriate, numbers of relevant pages, for example:
   `[2] Rizzo F.I., Shippy D.I.:` *`A method of solution for certain problems of transient heat conduction`*`. AIAA J.` **`8`**`(1970), No. 11, 2004–2009.`

   For works originally published in a language other than English, the language should be indicated in parentheses at the end of the reference.

   Authors are responsible for ensuring that the information in each reference is complete and accurate.

10. As the papers are published in English, the authors who are not native speakers of English are obliged to have the paper thoroughly reviewed language-wise before submitting for publication.

Manuscript submission Manuscripts to be considered for publication should be electronically submitted to the Editorial Office via the online submission and reviewing system, the Editorial System, at http://www.editorialsystem.com/aot. Submission to the journal proceeds totally on line and you will be guided stepwise throughout the process of the creation and uploading of your files. The body of the text, tables and figures, along with captions for figures and tables should be submitted separately. The system automatically converts source files to a single PDF file article, for subsequent approval by the corresponding Author, which is then used in the peer-review process. All correspondence, including notification confirming the submission of the manuscripts to the Editorial Office, notification of the Editorsñs decision and requests for revision, takes place by e-mails. Authors should designate the corresponding author, whose responsibility is to represent the Authors in contacts with the Editorial Office. Authors are requested not to submit the manuscripts by post or e-mail.

The illustrations may be submitted in color, however they will be printed in black and white in the journal, so the grayscale contributions are preferable. Therefore, the figure caption and the entire text of the paper should not make any reference to color in the illustration. Moreover the illustration should effectively convey author's intended meaning when it is printed as a halftone. The illustrations will be reproduced in color in the online publication.

Further information All manuscripts will undergo some editorial modification. The paper proofs (as PDF file) will be sent by e-mail to the corresponding author for acceptance, and should be returned within two weeks of receipt. Within the proofs corrections of minor and typographical errors in: author names, affiliations, articles titles, abstracts and keywords, formulas, symbols, grammatical error, details in figures, etc., are only allowed, as well as necessary small additions. The changes within the text will be accepted in case of serious errors, for example with regard to scientific accuracy, or if authors reputation and that of the journal would be affected. Submitted material will not be returned to the author, unless specifically requested.
A PDF file of published paper will be supplied free of charge to the Corresponding Author.

Submission of the manuscript expresses at the same time the authors consent to its publishing in both printed and electronic versions.

Transfer of Copyright Agreement Submission of the manuscript means that the authors automatically agree to assign the copyright to the Publisher. Once a paper has been accepted for publication, as a condition of publication, the authors are asked to send by email a scanned copy of the signed original of the Transfer of Copyright Agreement, signed by the Corresponding Author on behalf of all authors to the Managing Editor of the Journal. The copyright form can be downloaded from the journal's website at http://www.imp.gda.pl/archives-of-thermodynamics/ under Notes for Contributors.

The Editorial Committee